VILNIUS UNIVERSITY
CENTER FOR PHYSICAL SCIENCES AND TECHNOLOGY

Artyom Plyushch

Dielectric properties of composites with carbon nanoparticles.

Doctoral dissertation
Physical sciences, physics – 02P

Vilnius, 2018

The dissertation work was carried out at Vilnius University from 2014 to 2018.

Scientific supervisor:

Dr. Jan Macutkevič (Vilnius University, physical sciences, physics – 02P)

VILNIAUS UNIVERSITETAS
FIZINIŲ IR TECHNOLOGIJOS MOKSLŲ CENTRAS

Artyom Plyushch

Kompozitų su anglies nanodalelėmis dielektrinės savybės

Daktaro disertacija
Fiziniai mokslai, fizika – 02P

Vilnius, 2018

Disertacija rengta 2014 - 2018 metais Vilniaus universitete.

Mokslinis vadovas:

Dr. Jan Macutkevič (Vilniaus universitetas, fiziniai mokslai, fizika – 02P)

Acknowledgements

It is not a fair task to acknowledge all the people who made this Ph.D. thesis possible with a few words. However, I will try to do my best to extend my great appreciation to everyone who helped me scientifically and emotionally through out this study.

This project would never have been possible without the support and guidance of various people at the Vilnius university and the Institute for Nuclear Problems, BSU, Minsk.

I would like to thank doctor Jan Macutkevič for giving me the wonderful opportunity to complete my Ph.D. thesis under his supervision. Thank you for all the advice, ideas, moral support and patience in guiding me through this project.

I am sincerely gratefull to professor Jūras Banys for carefull help, support and vise advices he giving me for the years of study.

Special thanks should be given to doctor Polina Kuzhir. Thank you for introducing me to the study the electromagnetism of non homogeneous media ten years ago, for your continuous support and guidance in the years that followed and for keeping me motivated throughout the writing and editing of the articles bound in this thesis.

A very special thanks to doctor Vytautas Samulionis for his help with ultrasonic measurements.

To my friends and colleagues for many years: Alesia Paddubskaya, Dzmitry Buchanok, Nadzezhda Volynets for the stimulating discussions, for the hardworking together, and for all the fun we have had in the last four years.

To my friends and colleagues in Vilnius University (without particlular order): Maksim Ivanov, Šarunas Svirskas, Sergejus Balčiūnas, Ieva Kranauskaitė, Dziugas Jablonskas, Robertas Grigalaitis, Mantas Šimėnas for friendly atmosphere in the lab, support and help.

Doctor Patrizia Lamberti and doctor Giovanni Spinelli for the advices with modelling and valuable discussions.

Professor Alain Celzard and doctor Vanessa Fierro for the help with sample synthesis.

I am deeply thankful to my parents and my famly, wife Natalya and daughter Sonia for their love and support.

Artyom Plyushch

Vilnius, 2018

Table of Contents

Notations

GNP – graphite nanoplatellete
TGS – triglycine sulfate
CNT – carbon nanotubes
MC – Monte Carlo method
UC – unit cell
PU – polyurethane
FMG – flat micronic graphite

Chapter 1

Introduction

1.1 Recent progress in material science: polymer nanocomposites

The ability of polymers to act as electrical insulators is the basis for their widespread use in the electromagnetic field, the resistivity of which is generally around $10^{15}\ \Omega m$. However, material designers have sought to impart conduction to polymers by blending insulating polymers with conductive ingredients such as carbon blacks, carbon fibers, metal particles or conducting polymers such as polyaniline [1]. As a consequence, a range of so-called conductive polymer composite has come to existence since the 1950*s* with the resistivity between the metallic conductor ($10^{-7}\ \Omega m$) and insulating materials ($10^{15}\ \Omega m$) [2]. Such polymers can find their applications in many fields such as floor heating elements, electronic equipment [3], important strategic materials such as electromagnetic interference (EMI) shielding [4], apart from the conventional application of semiconducting materials for dissipation of static electricity [5]. More recently conductive composites have been used for sensing components [6, 7]. Compared with the metallic conductor, conductive polymer composites have the advantages of ease of shaping, low density, and the wide range of electrical conductivities as well as corrosion resistance [5, 8].

Since the carbon nanotubes (CNT) were discovered by Iijima [9] it become the point of interest as the functional filler for the composites. CNT is the graphene list rolled particular order to form the tube. Composites filled with CNT are widely studied due to the possibility to improve mechanical [10], electrical [11],

shielding properties of the polymers. Due to the high aspect ratio of the CNT, it is possible to improve the composite using the very low content of the filler (usually lower then 3-4 $wt.$ %), so the advantages of the polymers like flexibility, wear resistance are also kept. However, the CNT has also several disadvantages. Mainly the ability of the nanotubes to agglomerate leads to the non-uniform distribution of filler in the composite. As the result, we should increase the necessary amount of filler that may cause the destruction of the polymer.

A two-dimensional graphitic nanostructured material, in particular, graphite nanoplatelets (GNP) is a great alternative to carbon nanotubes to be used as a filler. GNP opens new perspectives to the material science for several reasons: (i) it is cheaper then CNT, (ii) it has lower agglomeration ability, (iii) the synthesis of GNP is simple and does not require sophisticated equipment, (iv) it is safer for the health. Due to mentioned, the big amount of the researcher's activity was aimed to study the GNP / polymer composites.

Despite the significant success achieved in this field, there are still a lot of open questions.

Mainly the possible applications require the multifunctional materials, that can be used in different aggressive conditions. For instance, in avionics, it is important for the composite to be usable at higher or lower temperatures. However, the systematic study of the temperature behaviour of the dielectric properties was not performed.

Another attractive point is hybrid composites with two or more different fillers (carbonaceous or not). Many researchers report on the experimental observation of the synergetic effects of polymer composites filled with different combinations of carbon relative fillers, for instance: CNT + GNP [12, 13, 14], GNP + carbon black (CB) [15, 16, 17]. But only a few theoretical or numerical models contribute to describing the properties of the hybrid composites of this type [18].

Different type of hybrid composite is carbon-based composites with non - carbon phase, like ferroelectrics or ferromagnetics, were investigations are mainly aimed to combine the advantages of both fillers in the final composite. Such composites are promising for the wave absorption systems, energy storage properties [19] and electronic device applications [20]. Researchers are mostly focused on the CNT + ferroelectric hybrids, while GNP+ferroelectric systems receive less attention.

1.2 Aims and tasks of the work

The main aim of the current work is to investigate the dielectric properties of the composites with 2D carbon inclusions.

The tasks of the current work are:

1. Study the dielectric properties of polymer composited filled with 2D nanostructured graphitic inclusions in a wide frequency and temperature ranges.

2. Study the dielectric and piezoelectric properties of the hybrid systems based on the ferroelectric / polymer composites with addition of 2D nanostructured graphitic inclusions.

3. Develop the numerical model for the percolation phenomena description in composites filled with 2D inclusion and hybrid (different types of inclusions).

The main instruments of the experimental investigations are broadband dielectric spectroscopy and acoustic spectroscopy. The main method of numerical study is Tabu search method based on the Monte Carlo approach.

1.3 Novel contributions

1. The experimental study of dielectric properties of composite systems based on insulating polymer matrices (epoxy resin and PU) with GNP and FMG inclusions respectively, in wide frequency (20 Hz – 2 THz) and temperature (100 – 600 K) ranges were performed. The significant rise of the permittivity and conductivity was observed upon the first heating / cooling cycle. For the first time, the effect of the inclusion redistribution above the polymer glassy temperature was proved to be the most possible physical mechanism of the phenomenon. The redistribution effect was demonstrated for the cases of GNP / epoxy resin composite and FMG / polyurethane composite.

2. For the first time, the experimental study of dielectric and piezoelectric properties of the hybrid polymer composite with inclusions of GNP and triglycine sulfate crystallites was performed. The strong synergy between

GNP and ferroelectric particles was demonstrated. Two physical mechanisms underlying this synergy are the following: higher dispersion and therefore finer distribution of TGS particles in multiphase composites, and the creation of local electric fields by GNP inside the composite.

3. Monte Carlo Model based on Tabu search method for the modelling of the percolation processes in composites with randomly distributed inclusions was developed. The limiting case of 2D inclusions distributed in the matrix below and close to percolation threshold was confirmed *via* comparison with available experimental data. For the first time, the Monte Carlo based model was applied for the simulations of hybrid composites, comprising 2D+1D inclusions.

1.4 Author's contribution

The author performed all the dielectric studies described in the dissertation. He also produced hybrid composites of TGS / GNP epoxy resin during an internship at Epinal University, supervised by prof. Alain Celzard (Epinal University). Piezoelectric measurements were performed with the help of doc. V. Samulionis. The model was developed with Prof. Patrizia Lamberti. The calculations program has been written and all calculations have been done by himself. The author wrote the articles himself (on the basis of which he prepared a dissertation), in consultation with the authors.

1.5 Statements presented for defence

1. The redistribution effects appear in polymeric composites with two dimensional graphitic inclusions close to the percolation threshold after the first annealing above the glass transition temperature. After the first annealing above the glass transition temperature electromagnetic properties of epoxy resin and PU composites in a wide frequency range substantially improved due to the better distribution of the inclusion particles.

2. The dielectric and piezoelectric properties of polymeric composites with ferroelectric inclusions are strongly improved by the addition of GNP in wide temperature range due to the better distribution of particles and

creation of local electric field by GNP which enhances the piezoelectric response of ternary composition due to electromagnetic coupling.

3. The numeric model for the percolation threshold calculation in composites filled with randomly distributed nanosized inclusions was developed. The main advantage of the model is the possibility to be applied for the different dimensionality (0D, 1D, 2D), mean size distribution of the filler, and what is more important, different filling fractions for any of the additives combinations.

1.6 List of publications included into the thesis

1. A. Plyushch, J. Macutkevic, P. Kuzhir, J. Banys, D. Bychanok, P. Lambin, S. Bistarelli, A. Cataldo, F. Micciulla, S. Bellucci, Electromagnetic properties of graphene nanoplatelets/epoxy composites, Composites Science and Technology 128 (2016) 75–83.

2. A. Plyushch, J. Macutkevic, P. Kuzhir, J. Banys, V. Fierro, A. Celzard, Dielectric properties and electrical conductivity of flat micronic graphite/polyurethane composites, Journal of Nanophotonics 10(1) (2016) 012511–012511.

3. A. Plyushch, J. Macutkevič, J. Banys, P. Kuzhir, N. Kalanda, A. Petrov, C. Silvestre, M.A. Uimin, A.Ye. Yermakov, O. Shenderova, Carbon-Coated Nickel Nanoparticles: Effect on the Magnetic and Electric Properties of Composite Materials, Coatings 8(5), (2018), 165–175.

4. A. Plyushch, J. Macutkevic, V. Samulionis, J. Banys, Dz. Bychanok, P. Kuzhir, S. Mathieu, V. Fierro, A. Celzard, Synergetic effect of triglycine sulfate and graphite nanoplatelets on dielectric and piezoelectric properties of epoxy resin composites, *published online,* Polymer Composites, DOI: /10.1142/9789813224537_0046.

5. A. Plyushch, P. Lamberti, G. Spinelli, J. Macutkevic, P. Kuzhir, Numerical Simulation of the Percolation Threshold in Non-overlapping Ellipsoid Composites: Toward bottom-up approach for carbon based electromagnetic components realization, Applied Sciences 8(6), (2018) 882–891.

1.7 List of conference presentations

1. Redistribution effects in graphene nano platelets / epoxy resin composite A. Plyushch, J. Macutkevic, P. Kuzhir, J. Banys, Dz. Bychanok, S. Maksimenko, A. Cataldo, F. Miciulla and S. Bellucci, FMNT-2015 | October 5^{th} - 8^{th}, Vilnius, Lithuania

2. Electromagnetic properties of GNP/epoxy composites in a wide temperature range. A. Plyushch, J. Macutkevic, P. Kuzhir, J. Banys, Dz. Bychanok, S. Maksimenko, A. Cataldo, F. Miciulla and S. Bellucci, Nanomeeting 2015, May 26^{th} - 29^{th}, Minsk, Belarus

3. Graphene nano platelets / epoxy composites in a wide frequency and temperature range, A. Plyushch, J. Macutkevic, P. Kuzhir, J. Banys, Dz. Bychanok, S. Maksimenko, A. Cataldo, F. Miciulla and S. Bellucci, FANEM 2015, May 25^{th}-27^{th}, Minsk, Belarus

4. Kompozitų su grafeno intarpais dielektrinės savybės A. Plyushch, J. Macutkevič, P. Kuzhir, J. Banys, D. Bychanok, S. Maksimenko, A. Cataldo, F. Miciulla, S. Bistarrelli, S. Bellucci, June 17^{th} - 19^{th}, Vilnius, 2015

5. Dielectric and shielding properties of Ni@C/ polydimethylsiloxane composites, A. Plyushch, J. Macutkevič, J. Banys, P. Kuzhir, O. Shenderova, LUP-2016, September 5^{th} - 9^{th}, Palanga, Lithuania.

6. Kompozitų su triglicinsulfato ir grafeno nanodalelėmis dielektrinės savybės, A. Plyushch, J. Macutkevic, V. Samulionis, J. Banys, Dz. Bychanok, P. Kuzhir, V. Fierro, A. Celzard, October 4^{th}-6^{th}, Vilnius, 2017

7. Dielectric and piezoelectric properties of triglycine sulfate and graphite nanoplatelets epoxy resin composites, A. Plyushch, J. Macutkevic, V. Samulionis, J. Banys, Dz. Bychanok, P. Kuzhir, S. Mathieu, V. Fierro, A. Celzard, FANEM 2018, June 5^{th}-7^{th}, Minsk, Belarus

1.8 Other papers

1. P. Kuzhir, A. Paddubskaya, D. Bychanok, A. Nemilentsau, M. Shuba, A. Plusch, S. Maksimenko, S. Bellucci, L. Coderoni, F. Micciulla, I. Sacco, G.

Rinaldi, J. Macutkevic, D. Seliuta, G. Valusis, J. Banys, Microwave probing of nanocarbon based epoxy resin composite films: toward electromagnetic shielding, Thin Solid Films, 519(12), 4114–4118.

2. D. S. Bychanok, M. A. Kanygin, A. V. Okotrub, M. V. Shuba, A. G. Paddubskaya, A. O. Plyushch, P. P. Kuzhir, S. A. Maksimenko, Anisotropy of the Electromagnetic Properties of Polymer Composites Based on Multiwall Carbon Nanotubes in the Gigahertz Frequency Range, JETP Letters, 93 (10), 607–611 (2011)

3. A. Paddubskaya, D. Bychanok, A. Plyushch, P. Kuzhir, A. Nemilentsau, S. Maksimenko, S. Bellucci, L. Coderoni, F. Micciulla, I. Sacco, G. Rinaldi, Epoxy Resin/SWCNT Shielding Paint for Super-High-Frequency Range, J. Nanoelectronics and Optoelectronics, Vol. 7, 81–86, 2012

4. P. Kuzhir, V. Ksenevich, A. Paddubskaya, T. Veselova, D. Bychanok, A. Plusch, A. Nemilentsau, M. Shuba, S. Maksimenko, S. Bellucci, L. Coderoni, F. Micciulla, I. Sacco, G. Rinaldi, CNT based epoxy resin composites for conductive applications, Nanoscience and Nanotechnology Letters, 2011, Vol. 3, No. 6 (6pp)

5. M. V. Shuba, A. G. Paddubskaya, A. O. Plyushch, P. P. Kuzhir, G. Ya. Slepyan, S. A. Maksimenko, V. K. Ksenevich, P. Buka, D. Seliuta, I. Kasalynas, J. Macutkevic, G. Valusis, C. Thomsen, A. Lakhtakia, Experimental evidence of localized plasmon resonance in composite materials containing single-wall carbon nanotubes, PHYSICAL REVIEW B 85, 165435 (2012)

6. Pliushch A., Paddubskaya A., Kuzhir P., Maksimenko S., Coderoni L., MicciullaF., Sacco I., Bellucci S., NANOCARBON modified epoxy resin and microwaves, Nanocarbon Modified Epoxy Resin and Microwaves, Fullerenes, Nanotubes and Carbon Nanostructures, 20:4-7, 496-501, 2012

7. M.A. Kanygin O.V. Sedelnikova, I.P. Asanova, L.G. Bulusheva, A.V. Okotrub, P.P. Kuzhir, A.O. Plyushch, S.A. Maksimenko, K.N. Lapko, A.A. Sokol, O.A.Ivashkevich, Ph. Lambin, Journal of Applied Physics, 113, 144315 (2013) (8pp)

8. A. Plyushch, D. Bychanok, P. Kuzhir, S. Maksimenko, K. Lapko, A. Sokol, J. Macutkevic, J. Banys, F. Micciulla, A. Cataldo, S. Bellucci, Heat resistant

unfired phosphate ceramics with carbon nanotubes for electromagnetic application Physica Status Solidi A, I.f. 1.525, 211, No. 11, 2580–2585 (2014).

9. D. Bychanok , A. Plyushch , K. Piasotski , A. Paddubskaya , S. Varanovich, P. Kuzhir, S. Baturkin, A. Klochkov,E. Korovin, M. Letellier, S. Schaefer, A. Szczurek, V. Fierro and A. Celzard, Electromagnetic properties of polyurethane template-based carbon foams in Ka-band, Physica Scripta, Volume 90,Number 9 2015

10. Natalia Apanasevich; Aliaksei Sokal ; Konstantin Lapko; Alexander Kudlash; Vladimir Lomonosov; Artem Plyushch; Polina P. Kuzhir, PhD; Jan Macutkevic; Juras Banys; Alexander Okotrub Phosphate ceramics - carbon nanotubes composites: liquid aluminum phosphate vs solid magnesium phosphate binder, Ceramics International, Volume 41, Issue 9, Part B, November 2015, Pages 12147–12152,

11. Artyom Plyushch, Polina P. Kuzhir, Sergey A. Maksimenko, Jan Macutkevič, Jūras Banys, Aliaksei Sokal, Konstantin N. Lapko, Vladislav Arkhipov, Alexander Okotrub, Grain size effect in conductive phosphate / carbon nanotube ceramics, Ceramics International 43(6) 4965–4969, 2017

Chapter 2

Overview

2.1 Dielectric permittivity

The relative permittivity (ε) and the permeability (μ) are main material parameters in electrodynamics. For nonmagnetic material μ = 1. Generally, the dielectric permittivity defined as the ratio of the electrical field amplitude in material and in a vacuum. In case if the material has nonzero dielectric losses, then not only the amplitude changes but also the phase ϕ. Then the dielectric permittivity can be introduced as the complex number. In that case, the relative permittivity defined as follows. The equation for a planar wave which propagates along z direction states [21]:

$$E = E_0 e^{i\omega t - ikz}, \tag{2.1}$$

where i is an imaginary unit, k is a wave number, z is coordinate, $\omega = 2\pi\nu$ is an angular frequency, and t is the time. Being propagated inside the material with complex refraction index $n = n' + in$" the wave equation (2.1) will read:

$$D = \varepsilon\varepsilon_0 E_0 e^{i\omega t - ikz}, \tag{2.2}$$

here $\varepsilon_0 \approx 8.85410^{-12} F/m$ - is the dielectric constant (vacuum permittivity). The complex permittivity can be recalculated into polar coordinates as:

$$\varepsilon = \varepsilon' - i\varepsilon'' = |\varepsilon| e^{-i\delta}. \tag{2.3}$$

Where $|\varepsilon| = \sqrt{\varepsilon'^2 + \varepsilon''^2}$ and $\delta = arctg(\frac{\varepsilon''}{\varepsilon'})$ are modulus and the loss angle ε. The complex dielectric permittivity can be presented in polar coordinates as:

$$D = \varepsilon_0|\varepsilon|e^{-i\delta}E_0e^{i\omega t-ikz} = \varepsilon_0|\varepsilon|E_0e^{i\omega t-i\delta-ikz}, \tag{2.4}$$

In present work, we will keep the notation of $\varepsilon = \varepsilon' - i\varepsilon"$. In case of the anisotropic material, the dielectric permittivity presents a frequency dependent complex tensor $\varepsilon(\omega) = \varepsilon_{ij}(\omega)$. In present work we are focused on the investigation of non-anisotropic materials, so we denote the permittivity as frequency dependent complex scalar $\varepsilon(\omega) = \varepsilon'(\omega) - i\varepsilon"(\omega)$. Next, the most basic cases of frequency dependencies of permittivity will be discussed.

2.1.1 Debye relaxation

The Debye relaxation model was developed to describe the response of polar liquid to an externally applied electric field. More details presented in book [22]. The main idea is that the reorientation of the dipoles is not immediate, and some finite amount of time is necessary. Mathematically it reads as follows. Let at the initial moment $t = 0$, the electric field of E_0 applied to the material. Then the time dependence of the electric displacement vector reads:

$$D(t) = \varepsilon_0\varepsilon_\infty E + \varepsilon_0(\varepsilon_s - \varepsilon_\infty)f_0(t)E, \tag{2.5}$$

where ε_s and ε_∞ are the static and high-frequancy limits of ε. The first term corresponds to the immediate response of the system, and the second term corresponds to the slow dipole polarisation. Here$f_0(t)$ is the time-dependent function, which by definition is $f_0(0) = 0$, and $f_0(\infty) = 1$. The time dependence of the polarisation vector can be described as follows:

$$\frac{dP}{dt} = -\frac{P(\infty) - P(t)}{\tau}, \tag{2.6}$$

where τ is the relaxation time. Solving the equation (2.6) one can obtain:

$$P(t) = P(\infty)(1 - e^{-t/\tau}), \tag{2.7}$$

If we compare equations (2.5) and (2.7) we can obtain the function $f_0(t)$ in explicit form of:

$$f_0(t) = (1 - e^{-t/\tau}). \tag{2.8}$$

Lets calculate the derivative of the equation (2.5):

$$\frac{dD(t)}{dt} = \varepsilon_0\varepsilon_\infty \frac{dE(t)}{dt} + \varepsilon_0\varepsilon_s \frac{E(t)}{\tau} - \frac{D(t)}{\tau}. \tag{2.9}$$

In case if external field has the form of $E(t) = E_0 e^{-iwt}$ and the electric displacement vector is $D(t) = D_0 e^{-iw(t-\varphi)}$, the equation (2.9) can be transformed into linear, and the well-known Debye equation may be obtained:

$$\varepsilon = \frac{D(t)}{\varepsilon_0 E(t)} = \varepsilon_\infty + \frac{\varepsilon_s - \varepsilon_\infty}{1 - i\omega\tau}. \tag{2.10}$$

.

From the equation (2.10) the real and imaginary part of the permittivity may be derived as follows:

$$\begin{cases} \varepsilon' = \varepsilon_\infty + \dfrac{\varepsilon_s - \varepsilon_\infty}{1 + \omega^2\tau^2} \\ \varepsilon'' = \dfrac{(\varepsilon_s - \varepsilon_\infty)\omega\tau}{1 + \omega^2\tau^2} \end{cases} \tag{2.11}$$

It can be easily shown, that the equations (2.11) are the parametric equation for the semicircle. The presentation of (2.10) as $\varepsilon''(\varepsilon')$ is known as Cole-Cole plot. The equation (2.10) is widely used for the descriprion of the experimental data [23, 24].

However, for many complex heterogeneous systems the relaxation process cannot be well described with the equation (2.10), but for the most cases modified formulas may be successfully used:

$$\varepsilon = \varepsilon_\infty + \frac{\varepsilon_s - \varepsilon_\infty}{[1 + (-i\omega\tau)^\alpha]^\beta}. \tag{2.12}$$

In this equation the exponents α and β are in range (0,1). The equation (2.12) is known as Havriliak – Negami ($\alpha \neq 1$, $\beta \neq 1$) and reduces to Cole-Cole equation ($\beta = 1$) and Davidson-Cole ($\alpha = 1$) [25, 26].

2.1.2 Maxwell – Wagner effect

The Maxwell – Wagner effect (or Maxwell – Wagner – Sillars) is similar to the Debye relaxation, but in this case, the material does not consist of the dipoles. The polarisation process takes place on the interfacial boundary of heterogeneous material under the external field (see figure 2.1). The basics of the Maxwell – Wagner effect are described in works of Maxwell, Wagner and Sillars [27, 28]. This effect is typical for the heterogeneous materials, in particular, ceramics and polymer composites filled with conductive inclusions.

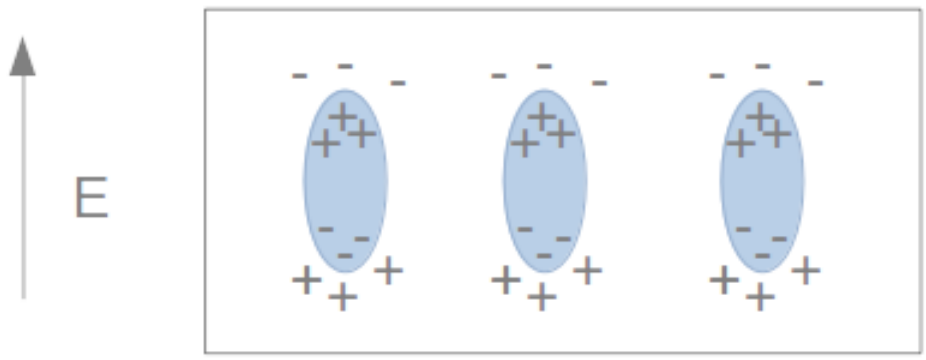

Figure 2.1: Nonhomogeneous sample polarised by external field

For this type of material, the dielectric permittivity ε may be as high as 1000 at low frequencies. In this case, the relaxational impact to the total permittivity spectrum may be very small and it is problematic to describe it. To overcome this difficulty in a study this effect the electric modulus, or the reciprocal complex permittivity was introduced as [29, 30]:

$$M = \frac{1}{\varepsilon' - i\varepsilon''} = \frac{\varepsilon' + i\varepsilon''}{\varepsilon'^2 + \varepsilon''^2} \tag{2.13}$$

It can be easily shown that the Cole-Cole plot presentation ($M''(M')$) will also have the semicircle shape, similarly to the equation (2.10).

Another possibility for Maxwell-Wagner relaxation description is the imped-

ance:

$$Z = \frac{1}{i\omega\varepsilon_0\varepsilon^*} = \frac{1}{i\omega\varepsilon_0(\varepsilon' - i\varepsilon'')} \tag{2.14}$$

The sample plased between the elecrodes it can be considered as a capacitor C, if the sample has substantial conductivity, then it can be considered as a capacitor C and resistor R connected in series. The impedance of the capacitor is $Z_C = \frac{1}{i\omega C}$ and $Z_R = R$ for the resistor, so the total impedance of th RC-circuit will be given as:

$$Z = \left(\frac{1}{Z_R} + \frac{1}{Z_C}\right)^{-1} = \left(\frac{1}{R} + i\omega C\right)^{-1} = \frac{R}{1 + i\omega\tau}, \tag{2.15}$$

where $\tau = RC$, the relaxation time of the RC-circuit. It is important to notice, that the equation (2.15) is similar to (2.10), but the underlying physics is different.

2.1.3 Basic principles of percolation theory

The percolation theory is the simplest not exactly solved model for multifacial material description [31]. The classic motivating problem behind percolation theory examines the flow of water over a porous stone. The pores in the stone can connect to each other forming the "cluster". In a case when the cluster size is comparable to the dimensions of the stone, the continuous path may be traced from the one border of the stone to opposite. The simple two-dimensional case is presented on figure 2.2.

In case of the composite materials is consisted of the insulating matrices and conductive particles as fillers the electric percolation is considered. Initially, the matrix is non-conductive, being enriched with some small amount of the conductive particles the dielectric properties are mainly governed by the properties of the matrix. If we increase the concentration, near the particular value of the filler fraction (p_c) the conductive path will be formed and the studied composite will undergo the phase transition from insulator to conductor. Close to percolation threshold the dielectric permittivity, as well as the conductivity, governs the following law [32]:

$$\begin{cases} \sigma = \sigma_0(\frac{p_c - p_f}{p_c})^{-s}, & p_f < p_c \\ \sigma = \sigma_i(\frac{p_f - p_c}{p_c})^{t}, & p_f > p_c \end{cases} \tag{2.16}$$

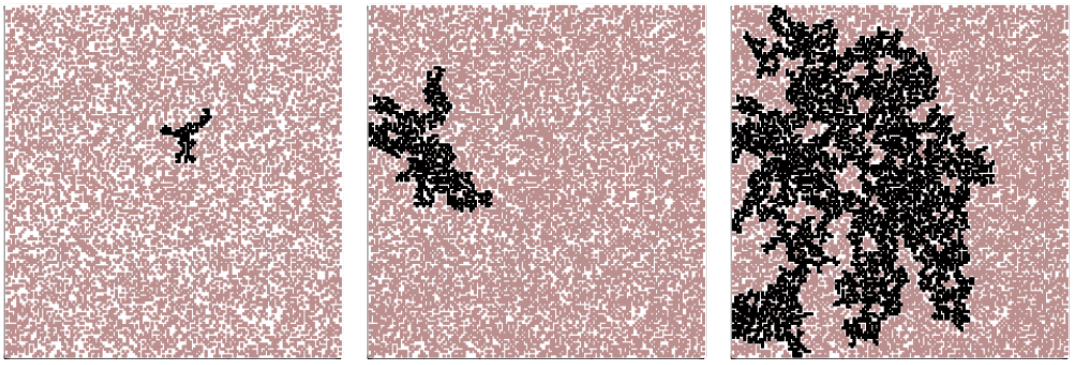

Figure 2.2: Percolation in 2D square lattices with system size $L \times L = 150 \times 150$. Occupation probability p = 0.45; 0.55; 0.59, respectively. Notice, that the largest cluster percolates through the lattice from top to bottom in this example when $p \geq 0.59$ [31].

Here σ_0 is the matrix conductivity, σ_i is the inclusions conductivity, s and t is the critical exponents, p_c is the percolation concentration, and p_f is the concentration of the conductive filler. Generaly, the physical properties behaviour near the percolation threshold can be illustrated as in figure 2.3.

From the experimental point of view, it is important to find out if the concentration in the sample under consideration is above the threshold or not. For the percolated composites the low-frequency dispersion of the real and the imaginary part of the permittivity can be described by Jonsher law [34, 35, 36]:

$$\begin{cases} \varepsilon^* \sim (-i\omega\tau)^{n_1-1}, & \omega > \omega_c \\ \varepsilon^* \sim (-i\omega\tau)^{n_{lfd}-1}, & \omega < \omega_c \end{cases} \tag{2.17}$$

where $\omega = 2\pi\nu$ is the angular frequency ω_c is the critical frequency, $n_{lfd} < n_1 < 1$. Since $\sigma = \varepsilon''\varepsilon_0\omega$, the imaginary part in equations (2.17) can be presented as [37]:

$$\sigma = \sigma_{dc} + \varepsilon_0\omega\varepsilon''(\omega) \tag{2.18}$$

where σ_{dc} is the dc conductivity and $\varepsilon_0\omega\varepsilon''(\omega)$ is the ac conductivity. In the case of non percolated sample the dc conductivity plateau has not been observed.

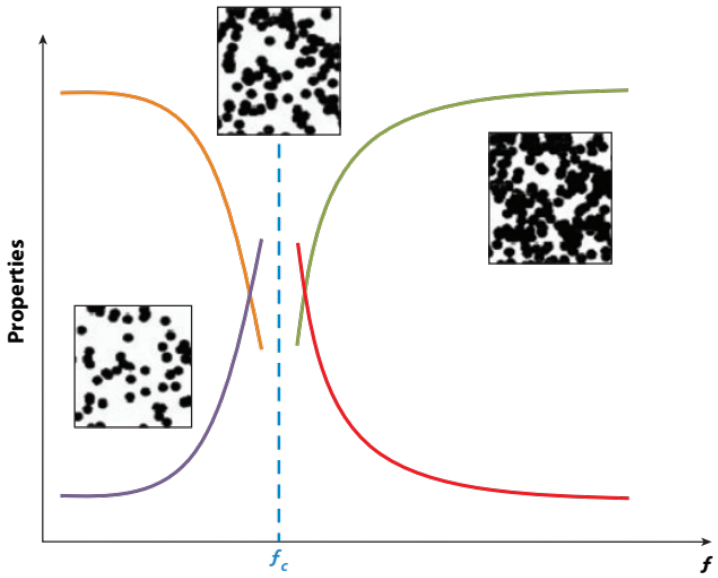

Figure 2.3: Schematic of nonlinear changes in the properties (the four curves denote different property parameters) of composites near the percolation threshold fc (dashed blue line). The insets show the geometric phase transition of fillers (denoted by dark spots) in the composites' microstructure near percolation. [33].

2.2 Basics of the ferroelectric materials

Ferroelectric materials are the materials wich demonstrate the spontaneous polarization in particular temperature range. The polarisation vector can change it's direction by means of an external field. A ferroelectric crystal consists of regions of homogeneous polarization that differ only in the direction of polarization. These regions are called domains. The simple possible domain configuration is presented on figure 2.4.

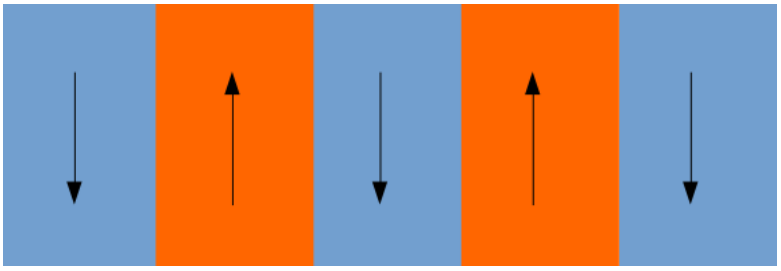

Figure 2.4: Schematic of domain structure of the crystal

The phenomenon of ferroelectricity is related to the crystallographic structure of the material. This can be illustrated for the case of barium titanate ($BaTiO_3$), a ferroelectric oxide that undergoes a transition from a ferroelectric tetragonal phase to a paraelectric cubic phase upon heating above 130 $^{\circ}C$. The physical principles of the phenomenon can be easily illustrated for the case of perovskite lattice. In particular, in cubic perovskite $BaTiO_3$, the structure of which is displayed in figure 2.5 (a), titanium atoms are octahedrally coordinated by six oxygen atoms. Ferroelectricity in tetragonal $BaTiO_3$ is due to an average relative displacement along the c-axis of titanium from its centrosymmetric position in the unit cell and consequently the creation of a permanent electric dipole.The tetragonal unit cell is shown in figure 2.5 (b). The elongation of the unit cell along the c-axis and consequently the deviation of the c/a ratio from unity are used as an indication of the presence of the ferroelectric phase [38].

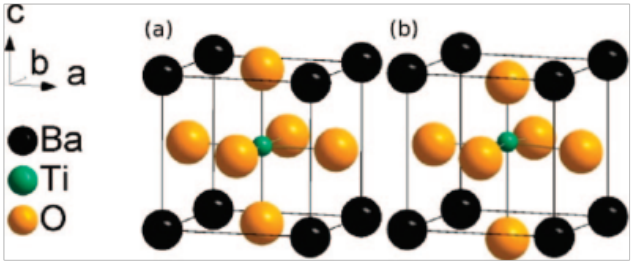

Figure 2.5: Unit cell of $BaTiO_3$ in both the (a) cubic $Pm-3m$ structure and (b) tetragonal $P4mm$ structure. In the tetragonal unit cell, atoms are displaced in the z-direction, and the cell is elongated along the c-axis. Atom positions: Ba at (0, 0, 0); Ti at (1/2, 1/2, z); O_1 at (1/2, 1/2, z); and O_2 at (1/2, 0, z). Displacements have been exaggerated for clarity. [38]

The temperature dependence of the permittivity of the ferroelectric materials in paraelectric phase is described with the Curie-Weiss law:

$$\varepsilon = \frac{C}{T - T_C} \tag{2.19}$$

here, C is the Curie-Weiss constant, T_C is the phase transition temperature. According to the equation (2.19), close to T_C the reciprocal permittivity $1/\varepsilon$ should demonstrate the linear dependence near the T_C point.

The important property of the ferroelectrics is the piezoelectricity phe-

nomenon: the ability of the material to accumulate the electric charge in response to the mechanical stress. The piezoelectricity is observed in single crystals and ceramics [39]. The piezoelectrics are widely used as sensors, sound generators and even as nanogenerators [40].

For the preparation of the composites, the size effect of the particles is important [41]. It was demonstrated, that with the size decrease the dielectric permittivity, the spontaneous polarization, piezoelectric properties and the phase transition temperature decreases. The surface energy for the smaller particles becomes comparable to the volume energy, so the spontaneous polarisation becomes unpreferable. The size effect is widely studied in nanosized ferroelectrics [42, 43], relaxors [44].

Chapter 3

Experimental methods

3.1 Methods of dielectric permittivity measurements

The main experimental techniques of the present work are the broadband dielectric and acoustic spectroscopy.

3.1.1 Quasistatic frequency range (20 Hz – 1 MHz)

Low frequency (20 Hz – 1 MHz) measurements were performed using LCR HP4284A meter. The capacitance (C) and loss tangent ($tg\delta = \varepsilon''/\varepsilon'$) of the sample were measured. The dielectric permittivity was recalculated using plane capacitor formulas:

$$\begin{cases} \varepsilon' = \dfrac{(C'_s - C_0)d_s}{\varepsilon_0 S_s} + 1, \\ tg\delta = \dfrac{C'_s tg(\delta_s) - C_0 tg(\delta_0)}{C'_s - C_0}, \end{cases} \tag{3.1}$$

where C'_s and $tg(\delta_s)$ are capacitance and tangent of losses of the systems with the sample, C'_0 and $tg(\delta_0)$ are capacitance and tangent of losses of the systems without the sample, d_s is height of the sample, S_s is the area of the sample.

For low-temperature measurements (25 – 300 K), the samples were placed in the closed-cycle cryostat. Measurements at high-temperature (300 – 500 K) were performed in a home-made furnace. All measurements were performed in ambient conditions with approximate heating / cooling rate 1 K/min. The temperature was controlled using Keithley Integra 2700 multimeter. The samples had the parallelepipedal shape with a typical area of 30 mm^2 and thickness of

1 mm. Silver paste was applied to improve the contacts between electrodes and sample.

3.1.2 Frequency range from 1 MHz up to 3 GHz

In the frequency range of 1 MHz – 3 GHz, the coaxial dielectric spectrometer with vector network analyzer Agilent 8714ET was used. The sample was placed at the end of the coaxial line between the inner conductor and the short piston and forms a capacitor, as shown on figure 3.1. The phase ϕ and the modulus R of the reflected signal were measured.

The reflected signal depends on the impedance connected to the transmission line in following way:

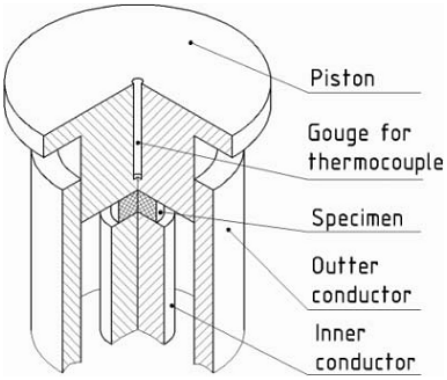

Figure 3.1: Schematic illustration of the sample installed at the end of coaxial line

$$R = \frac{Z_s - Z_0}{Z_s + Z_0}. \tag{3.2}$$

Here Z_s is the impedance of the sample and Z_0 is the impedance of the transmission line (50 Ω). Considering sample as a plane capacitor with $C_s^* = \varepsilon^* \varepsilon_0 S/d$, we can derive the impedance as follows:

$$Z_s = \frac{1}{\omega C^*} = \frac{d}{\varepsilon^* \varepsilon_0 S \omega}. \tag{3.3}$$

Using equations 3.2 and 3.3 the dielectric permittivity of the sample can be calculated. However, the described method can be applied only for the

quasistatic case, if the field is uniformly distributed inside the sample.

More precise method for the calculations of the permittivity can be proposed. The details are presented in book [45]. In general case, the field distribution is described with the Bessel functions:

$$E = A_k J_0 \left(\frac{2\pi r}{\lambda(\varepsilon_0 \varepsilon' \mu)^{1/2}} \right), \tag{3.4}$$

where A_k is the constant related with the dimensionality of the sample, r is the radial coordinate. the function nodes are given as:

$$r_1 = \frac{2.405\lambda}{2\pi(\varepsilon_0 \varepsilon' \mu)^{1/2}}. \tag{3.5}$$

If the radius of the sample is les then $0.1r_1$ then the field inside the sample can be considered as uniform. The external field excites the T-wave along the coaxial line. The components of the T-wave are [45]:

$$\begin{cases} E_z = -i \left(\frac{2\pi}{\lambda} \right)^2 \mu_0 (\varepsilon' \mu_0)^{1/2} A J_0 \left(\frac{2\pi r}{\lambda(\varepsilon_0 \varepsilon' \mu)^{1/2}} \right), \\ H_\phi = \left(\frac{2\pi}{\lambda} \right)^2 \varepsilon' \mu_0 A J_0' \left(\frac{2\pi r}{\lambda(\varepsilon_0 \varepsilon' \mu)^{1/2}} \right). \end{cases} \tag{3.6}$$

It can be demonstrated, that the capacitance of the dynamic capacitor reads:

$$C = \frac{\varepsilon'^{1/2} r J_1(\frac{2\pi}{\lambda} \varepsilon'^{1/2} r)}{\frac{2\pi}{\lambda} d J_0(\frac{2\pi}{\lambda} \varepsilon'^{1/2} r)} \tag{3.7}$$

Here, sample with typical area of S = 2 mm^2 and thickness of d = 0.3 mm were studied.

3.1.3 Microwave frequencies (25 – 36 GHz)

The microwave measurements were carried out with the waveguide system connected to scalar network analyzer R2-408R. The relation between the input and output signals can be described using scattering matrix S formalism:

$$\mathbf{b} = \mathbf{S}\mathbf{a}, \tag{3.8}$$

where $\mathbf{a} = (a_1, a_2)^T$ and $\mathbf{b} = (b_1, b_2)^T$ are the amplitudes of the input and output signal and the scatering matrix can be introduced as $S_{ij} = b_j/a_i$, i, j=1,2. Depending on the values of the permittivity, two different experimental technics are available.

3.1.3.1 Filled waveguide method

According to the first method, plane parallelepiped sample was cut to fit exactly the waveguide cross section as presented on the figure 3.2.

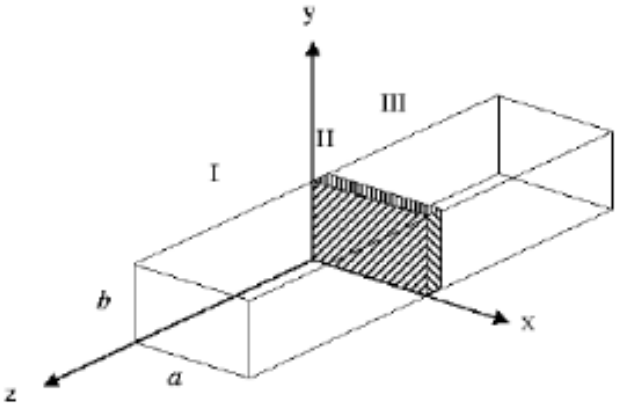

Figure 3.2: Schematic illustration of the waveguide with installed sample [46]

Three different areas can be introduced for this system: I – the area where the insident ratiation falls, II – the area occupied by the sample, and III – the area where transmitted signal propagates. The Hertz vector for these areas reads[46, 47]:

$$\begin{cases} \psi_I = \cos(\frac{\pi x}{a}) \left[C_1 e^{jk_z z} + C_2 e^{-jk_z z}\right], z \leq 0, \\ \psi_{II} = \cos(\frac{\pi x}{a}) \left[C_3 e^{jk_{2z} z} + C_4 e^{-jk_{2z} z}\right], 0 \leq z \leq \tau, \\ \psi_{III} = \cos(\frac{\pi x}{a}) C_5 e^{jk_z z}, z \geq \tau, \end{cases} \tag{3.9}$$

where τ - is the sample thickness, a - is the waveguide width, k_z and k_{2z} are the wavenumbers, which determines as:

$$k_z = \frac{\pi}{\lambda a}\sqrt{4a^2 - \lambda^2}, \tag{3.10}$$

$$k_{2z} = \frac{\pi}{\lambda a}\sqrt{4a^2\varepsilon - \lambda^2}. \tag{3.11}$$

Using the boundary contitions for I-III one can obtain [48],

$$\begin{cases} \psi_I|_0 = \psi_{II}|_0, \\ \psi_{II}|_\tau = \psi_{III}|_\tau, \\ \dfrac{\partial\psi_I}{\partial z}|_0 = \dfrac{\partial\psi_{II}}{\partial z}|_0, \\ \dfrac{\partial\psi_{II}}{\partial z}|_\tau = \dfrac{\partial\psi_{III}}{\partial z}|_\tau. \end{cases} \tag{3.12}$$

The electromagnetic response of the sample were measured as frequency dependent transmitted/input (S_{21}) and reflected/input (S_{11}) signals. The dielectric permittivity was recalculated from the S-parameters via following formulas [46]:

$$\begin{cases} S_{11} = \dfrac{C_2}{C_1} = \dfrac{-j[(k_z/k_{2z})^2 - 1]\sin(k_{2z}\tau)}{2j(k_z/k_{2z})\cos(k_{2z}\tau) + [(k_z/k_{2z}z)^2 + 1]\sin(k_{2z}\tau)} \\ S_{21} = \dfrac{C_5}{C_1} = \dfrac{2(k_{2z}/k_z)}{-2(k_{2z}/k_z)\cos(k_{2z}\tau) + j[(k_{2z}/k_z)^2 + 1]\sin(k_{2z}\tau)} \end{cases} \tag{3.13}$$

Solving the equations 3.13 numerically we can obtain the values of the complex dielectric permittivity ε^*. This method is suitable for samples with low permittivity constant and loss. Otherwise, if the sample's conductivity is high, the values of S_{21} will be close to zero.

3.1.3.2 Cylindrical rod method

The second approach is the measurements of the cylindrical rod placed in the waveguide perpendicularly to the broad waveguide wall as shown in the figure 3.3. Similarly to the previous method, the electromagnetic response (S_{21} and S_{11}) was measured.

$$\begin{cases} S_{11} = S_{11}(\varepsilon', \varepsilon''), \\ S_{21} = S_{21}(\varepsilon', \varepsilon''). \end{cases} \tag{3.14}$$

For the dielectric permittivity recalculation the similar approach of the three regions can be used (see figure 3.4). The intrinsic TE_{10} wave propagates from region I to region III. The resulting amplitudes of the wave in region I are given

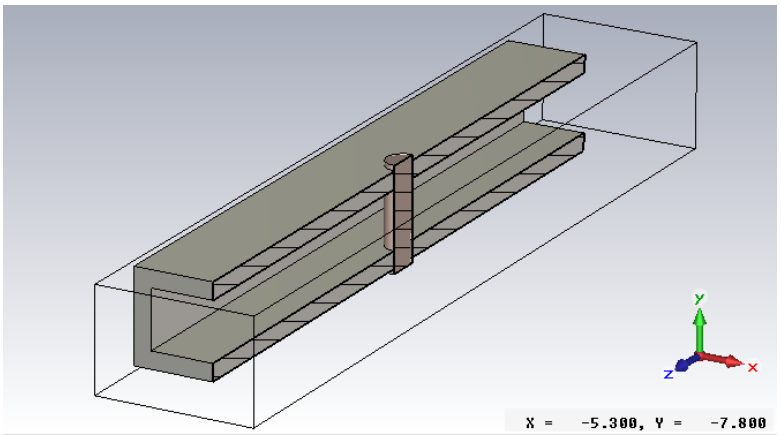

Figure 3.3: Schematic illustration of the waveguide with installed cylindrical sample

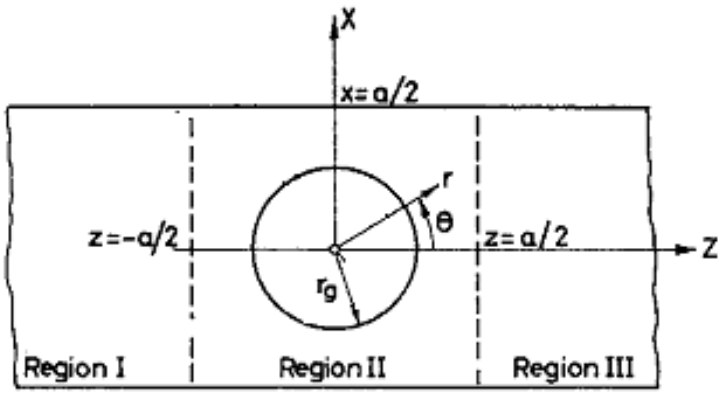

Figure 3.4: Schematic illustration of the waveguide with installed cylindrical sample, topview [49]

with equation:

$$\begin{cases} E_y^I(x,z) = \sum_{m=1}^{\infty} A_m cos(\gamma_m x) e^{ik_m z}, \\ H_y^I(x,z) = \frac{1}{\omega\mu} \sum_{m=1}^{\infty} A_m k_m cos(\gamma_m x) e^{ik_m z}, \\ H_z^I(x,z) = i\frac{1}{\omega\mu} \sum_{m=1}^{\infty} A_m \gamma cos(\gamma_m x) e^{ik_m l z}, \end{cases} \tag{3.15}$$

where m=1,3,5,7..., that is related with the fact, that only modes with odd

components are in scattered field, $\gamma_m = \frac{m\pi}{a}$, $k_m = \sqrt{k_0^2 - \gamma_m^2}$. Analogicaly to region I, the field in region III will read:

$$\begin{cases} E_y^{III}(x,z) = \sum_{m=1}^{\infty} B_m cos(\gamma_m x) e^{ik_m z}, \\ H_y^{III}(x,z) = -\frac{1}{\omega\mu} \sum_{m=1}^{\infty} B_m k_m cos(\gamma_m x) e^{ik_m z}, \\ H_z^{III}(x,z) = i\frac{1}{\omega\mu} \sum_{m=1}^{\infty} B_m \gamma cos(\gamma_m x) e^{ik_m l z}, \end{cases} \tag{3.16}$$

To describe the field distribution in region II we introduce the cylindrical coordinates (r, θ, y). The field distribution is given by the analytic solution of the homogeneous equation:

$$(\nabla^2 - k^2) E_y(r,\theta) = 0 \tag{3.17}$$

Taking into account the symmetry of the system we obtain:

$$E_y(r,\theta) = \sum_{n=0}^{\infty} (a_n J_n(kr) + b_n Y_n(kr)) cos(n\theta), \tag{3.18}$$

here a_n and b_n are complex coefficients, J_n and Y_n are Bessel and Neyman functions. The field in region II outside the cylinder is given by the equations:

$$\begin{cases} E_y^{II}(r,\theta) = \sum_{n=0}^{\infty} (C_n J_n(k_0 r) + D_n Y_n(k_0 r)) cos(n\theta), \\ H_y^{II}(r,\theta) = i\frac{1}{\omega\mu} \sum_{n=0}^{\infty} \frac{n}{r} (C_n J_n(k_0 r) + D_n Y_n(k_0 r)) cos(n\theta), \\ H_z^{II}(r,\theta) = i\frac{1}{\omega\mu} \sum_{n=0}^{\infty} k_0 (C_n J_n'(k_0 r) + D_n Y_n(k_0 r)) cos(n\theta), \end{cases} \tag{3.19}$$

while inside the cylinder:

$$\begin{cases} E_y^d(r,\theta) = \sum_{n=0}^{\infty} E_n J_n(k_d r) cos(n\theta), \\ H_r^d(r,\theta) = i\frac{1}{\omega\mu}\sum_{n=0}^{\infty} \frac{n}{r} E_n J_n(k_d r) cos(n\theta), \\ H_\theta^d(r,\theta) = i\frac{1}{\omega\mu}\sum_{n=0}^{\infty} k_d E_n J_n'(k_d r) cos(n\theta), \end{cases} \tag{3.20}$$

where $k_d = \omega\sqrt{\mu\varepsilon_d}$.

Now all the field components are presented. Taking into account the symmenty if the system, the following boundary conditions may be applied [50]:

$$\begin{cases} E_y^d(r_d,\theta) = E_y^{II}(r_d,\theta), \\ H_\theta^d(r_d,\theta) = H_\theta^{II}(r_d,\theta), \end{cases} \tag{3.21}$$

where $\theta \in [0, 2\pi]$,

$$E_y^{II}(r_a,\theta_a) = 0 \tag{3.22}$$

where $r_a = \frac{a}{2sin(\theta_a)}$, $\theta_a \in \left[\frac{\pi}{4}, \frac{3\pi}{4}\right]$,

$$\begin{aligned} &E_y^{II}(r_b,\theta_b) = E_y^i(x_b, -\frac{a}{b}) + E_y^I(x_b, -\frac{a}{b}), \\ &H_y^{II}(r_b,\theta_b)cos(\theta_b) + H_r^{II}(r_b,\theta_b)sin(\theta_b) = H_x^i(x_b, -\frac{a}{b}) + H_x^I(x_b, -\frac{a}{b}) \end{aligned} \tag{3.23}$$

where $r_b = -\frac{a}{2cos(\theta_b)}$, $x_b = -\frac{a}{2}tg(\theta_b)$ and $\theta_b \in \left[\frac{3\pi}{4}, \pi\right]$,

$$\begin{aligned} &E_y^{II}(r_c,\theta_c) = E_y^{III}(x_c, \frac{a}{2}), \\ &H_\theta^{II}(r_c,\theta_c)cos(\theta_c) + H_r^{II}(r_c,\theta_c)sin(\theta_c) = H_x^{III}(x_c, \frac{a}{2}), \end{aligned} \tag{3.24}$$

where $r_c = \frac{a}{2cos(\theta_c)}$, $x_c = \frac{a}{2}tg(\theta_c)$ and $\theta_c \in \left[0, \frac{\pi}{4}\right]$.

Using the boundary conditions (3.21-3.24) the system (3.15-3.20) can be numericaly solved. The series were replaced with summations with the number of summands up to 10 for the calculations.

The advantage of this method is that it is not limited to the absolute values of the permittivity. However, in the case of smaller permittivity, the first method is preferable due to higher accuracy.

3.1.4 Teraherz frequency range

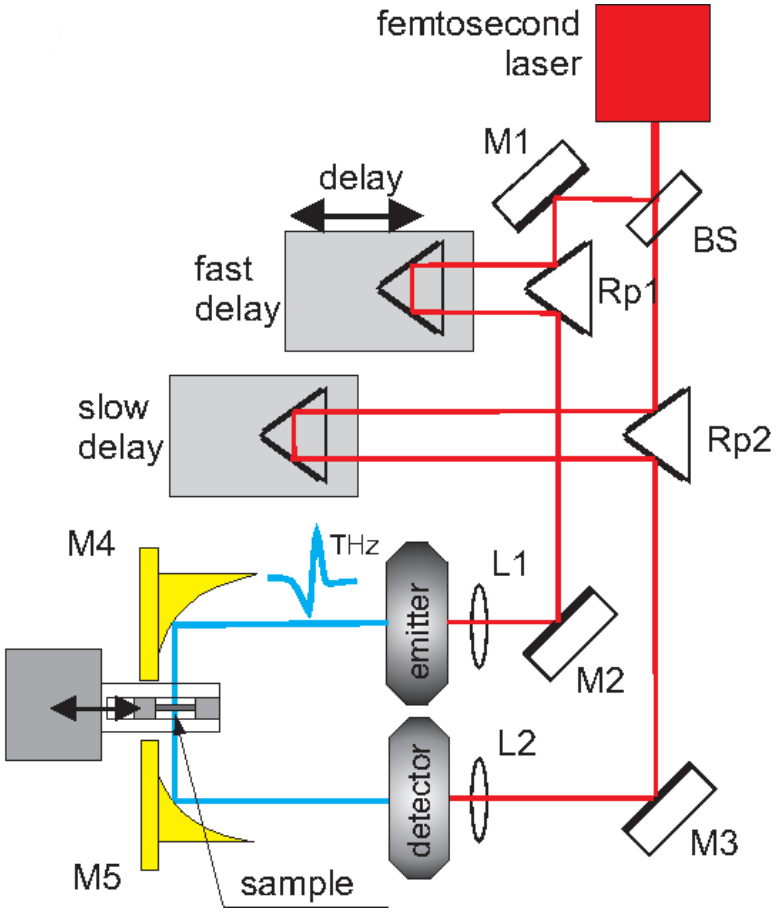

Figure 3.5: Schematic illustration of the waveguide with installed sample

Measurements at frequencies ranging from 100 GHz to 2 THz were performed in transmission mode using a time-domain THz spectrometer TERAVIL T-SPEC based on an femtosecond laser system. The spectroscopic method [51] consists in the measurement of a reference waveform $E_0(t)$ of reference signal (i.e. signal through the diaphragm without sample) and $E_s(t)$ a signal through the diaphragm with the sample. After fast Fourier transform, the spectral functions of $E_s(\omega)$ and $E_0(\omega)$ are obtained. The complex transmission function $T(\omega)$ can be defined as the ratio of reflected and reference spectra:

$$T(\omega) = \frac{E_s(\omega)}{E_0(\omega)} \tag{3.25}$$

Let E_0 is the amplitude of the incident polarised wave, then the complex

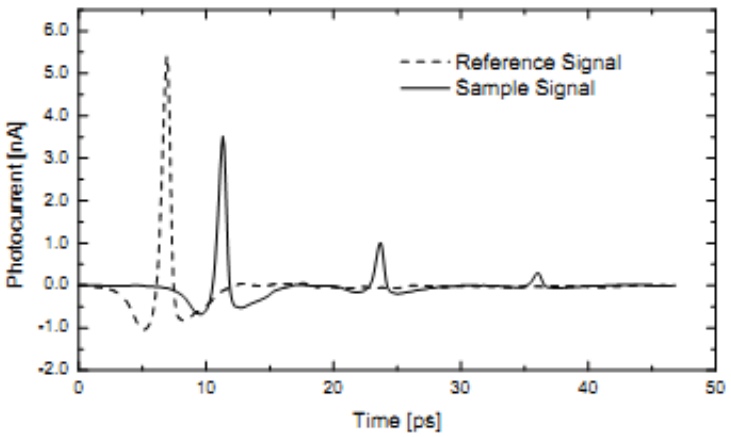

Figure 3.6: Reference and transmitted signals

amplitudes of the transmitted waves will read [52]:

$$E_p = \frac{4n(n-1)^{2p}}{(n+1)^{2p+2}} E_0 e^{\frac{-in\omega h(2p+1)}{c}} e^{i\omega h/c}, \tag{3.26}$$

where $n = \sqrt{\varepsilon\mu}$, h is the thickness of the sample, and p=0,1,2... Then, the transmitted spectrum will be:

$$T(\omega) = \frac{E_P(\omega)}{E_0} = \frac{4n(n-1)^{2p}}{(n+1)^{2p+2}} e^{\frac{-in\omega h(2p+1)}{c}} e^{i\omega h/c} \tag{3.27}$$

If the optical density of the sample is high, we consider $p = 0$ for the equation (3.27). It means that the first transmitted impuls brings the mean power of the transmitted radiation, while impulses with $p > 0$ can be neglected (see figure 3.6). The equation (3.27) can be easily solved to recalculate the dielectric permittivity ε.

3.2 Method of piezoelectric response measurements

The piezoelectric measurements were carried out using pulse-echo ultrasonic set-up according to the procedure described in papers [53, 54]. Z-cut $LiNbO_3$ piezoelectric transducer was used for sending 10 MHz ultrasonic wave in quartz buffer. The ultrasonic wave excited thin sample plate (0.25 mm in thickness)

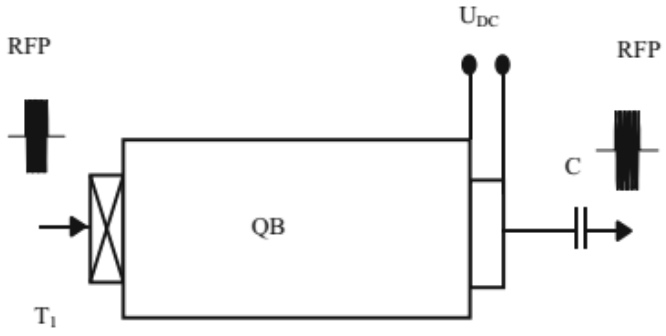

Figure 3.7: Experimental set up for piezoelectric test using pulse-echo ultrasonic system. RFP Radio frequency pulse, $T1$ lithium niobate ultrasonic transducer, QB quartz buffer [53, 54].

working as a receiving ultrasonic transducer attached to another end of a quartz buffer. The thickness of the sample was close to the approximately half of the ultrasonic wavelength in epoxy at 10 MHz frequency. Piezoelectric voltage in form of 10 MHz radio-pulse was measured by Agilent DSO3202A digital scope incorporated into the electronic pulse-echo set up for automatic temperature measurements.

Chapter 4

Redistribution effect of two-dimensional graphitic structures in polymer matrices

Composite materials consisting of insulating polymer matrices and conductive carbonaceous fillers attracted a lot of researcher's attention in the recent decades. Polymer composite mixing bulk specific properties of the matrix – flexibility, resistance to corrosion, good processability, strong adhesion to different substrates, curing ability etc — and conducting properties from the fillers (ferrites, noble metals, carbon and graphite nano- and microstructures) have received a lot of attention during the last two decades [55]. These advanced materials find more and more applications in aerospace, automotive, energy, electronics, defence and healthcare sectors [56]. Among others, one of the most promising fillers used to produce conductive polymer composites is carbon in various forms: carbon black [57], graphene [58], microsized quartz coated by graphene [59] vapor-grown carbon fibers [60], multi-walled and single-walled carbon nanotubes [61, 62], onion-like carbon [63]. A reason for that is the lightweight, the chemical resistance and the high dc and ac conductivity of those structures.

To explore the electromagnetic (EM) applications of composites, it is important to measure and analyze their electrical conductivity and effective permittivity. Several theoretical models can be used for the analysis, such as the percolation theory [64], Maxwell-Garnett [65, 66] and McLachlan [67] effective medium theories, and the generalized McLachlan-Jonsher theory [68]. The latter makes it possible to describe the frequency and concentration dependence of

the complex effective permittivity. In parallel, computer simulations methods become more and more efficient nowadays to predict the EM properties of composites. Novel methods of calculation allow taking into account the geometry of filler [69] and its influence on AC conductivity of composite [70], make possible performing simulations for a wide range of volume fractions, permittivity ratios and packing conditions [71]. Many researchers have examined this subject by performing *ab-initio* calculations, for example with density functional theory (DFT) [72], or finite-element method (FEM) [73, 73] and a combination of FEM and Monte-Carlo simulations [74, 75].

Carbon nanotubes (CNT) based composites are extremely interesting for conductive applications. CNTs lead to very low percolation threshold (0.03–0.5 $wt.$ % depending on the CNT origin, the wall surface quality, the functionalization, the dispersion state) and yield huge effective permittivity and electrical conductivity values at all frequencies [76] including microwave and terahertz ranges. However, a drawback of carbon nanotubes is their higher cost in comparison with other carbon nanostructures such as different derivatives of graphite. Another serious disadvantage is the possible toxicity of CNTs, which has been debated for long [77]. This problem seems less critical with bigger and/or less slender carbon particles such as graphene nanoplatelets (GNP) [78].

GNPs are carbon nanostructures consisting of small stacks of graphene sheets with the overall thickness from one nanometer to a few tens of nanometers, and lateral linear dimensions from a few micrometers up to hundreds of micrometers [79]. Graphene nanoplatelets are produced by thermal exfoliation of graphite intercalated compounds [80, 81]. By contrast with CNTs, the GNP production process is easy and cheap. Without a proper surface treatment, GNPs might have poor interfacial adhesion with polymers because of lack of chemical bonding [78, 82].

GNP functionalisation can lead to better interfacial adhesion to the polymer that improves mechanical [83] and thermal [84] properties of the resultant composite, but at the same time may deteriorate its electrical conductivity. Chemical treatments have been demonstrated improving the strength of interfacial interactions [85, 86] without changing significantly the EM properties of their composites [78].

Exploring the EM properties of nanocarbon-based composites at low temperatures (below 300K) is very important, for it gives information on the main

electrical transport mechanism [61, 87, 88, 89]. Also, the variation of EM properties of polymer / carbon composites with temperature is worth studying due to irreversible processes occurring near and above the glass transition temperature of the polymer matrices [90, 91, 92]. In this respect, the hysteresis of electromagnetic properties on heating and cooling cycles has already been reported for composites with carbon black [93], onion-like carbon [63] and CNTs [94]. Moreover, above the room temperature, the electrical conductivity and the effective permittivity of composites above the percolation threshold can increase or decrease with temperature [95, 96]. This effect can be related to particles redistribution or polymer matrix conductivity [97].

This chapter delivers the experimental investigation results of two different composite systems. The first one is the GNP / epoxy resin composite at different concentration of GNP. The second system is composite material based on a carbonaceous filler in the form of ultra-thin (100 nm) monocrystalline graphite flakes, called Flat Micronic Graphite (FMG) [98, 99, 100]. FMG particles have an average diameter of 10 μm, and as the polymer matrix used here was a thermoset polyurethane.

4.1 Sample preparation procedure

4.1.1 Graphene nanoplatelets / epoxy resin composites

Graphene nanoplatelets were produced by micro-cleavage exfoliation of expanded graphite. Expandable graphite was provided by Asbury® `https://asbury.com/`. Expandable graphite is manufactured by treating the flake graphite with various intercalation reagents that migrate between the graphene layers in a graphite crystal and remain as stable species. When exposed to a rapid increase of temperature, these intercalation compounds decompose into gaseous products as the result of high interlayer pressure. The internal stress is strong enough to push apart graphite basal planes along the c axis. Asbury expandable graphite exhibits a micronic and submicronic lamellar structure, an example of which revealed by SEM is shown in figure 4.1 (a). After micro-cleavage exfoliation, induced by microwave irradiation [101, 102, 103, 104, 105], a porous structure is visible in the SEM micrograph reproduced in figure 4.1 (b). A gentle treatment with ultrasound bath destroys the superstructure, releasing

GNP. Series of composite samples were produced using Epikote 828, a curing

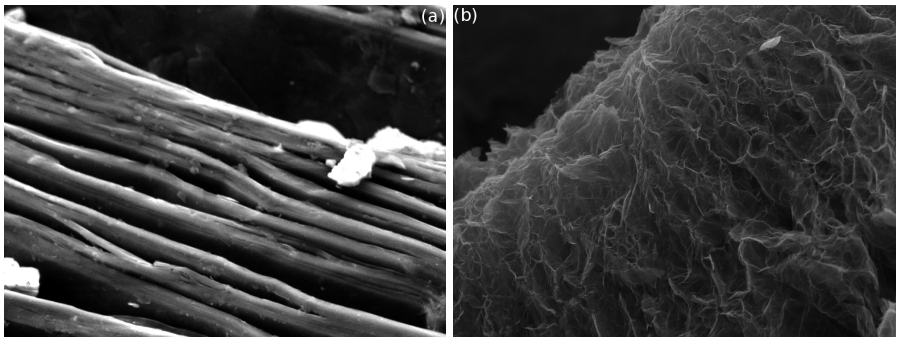

Figure 4.1: Lamellar structure of expandable graphite (a) and (b)worm-like GNP structure after exfoliation process.

agent A1 (i.e., a modified tetraethyl pentamine) and 0.25, 1, 2, 3 and 4 $wt.$ % of GNP filler. The resin was degassed under vacuum (1 – 3 $mbar$) for 12 – 14 h, then was put into an oven at 340 K. In the meantime, the GNPs were dispersed in propanol, and the suspension was submitted to an ultrasonic bath for 1.5 h. Afterwards, the alcoholic suspension of GNPs was mixed with the resin. The obtained mixture was placed inside an oven at 400 – 420 K for evaporating the alcohol. When alcohol was evaporated, the dispersion of GNP in uncured epoxy was additionally sonicated for 30 minutes. The curing agent A1 was added to the mixture of resin and filler through slow manual mixing for about 7 min. The blend was then poured into moulds of dimensions $1 \times 1 \times 7$ cm^3 and left as such for 20 h for the curing process at room temperature, and finally 4 h in an oven at 350 K. When the process was completed, the samples were removed from the moulds. After curing at room temperature, the samples were treated for 4 h in an oven at 350 K.

4.1.2 Flat micronic graphite / polyurethane composites

The FMG production scheme was described in papers [98, 99, 100]. This process consists first of preparing a sulphuric acid-graphite intercalation compound (GIC), using millimeter-size Madagascar natural graphite platelets. The GIC was then exfoliated at high temperature. The resultant expanded graphite was next suspended in cyclohexane and submitted to a series of grinding and ultrasonic dispersion steps. After freeze-drying of the suspension, a fluffy material was

obtained whose particle size distribution changed depending on the duration of the aforementioned steps. The present FMG flakes had an average diameter and thickness of about 10 μm and 0.1 μm, respectively, i.e., an aspect ratio of about 100, as proved by scanning electron microscopy observations [98]. Another important characteristic of FMG is that the preparation process allowed retaining the single crystal quality of the pristine graphite flakes.

For composite fabrication, polyurethane (PU) resin was freshly prepared by mixing in strictly controlled proportions, the corresponding base and hardener in the liquid state, and diluting the blend with an appropriate solvent. Various amounts of FMG particles were then weighed in calculated amounts for getting the desired volume fractions of graphite filler in the final dry composite after hardening. The amount of solvent was adjusted for each amount of FMG until the same low viscosity of the liquid blend was reached. A Brookfield viscometer was used for that purpose.

The liquid PU resin filled with FMG was then transferred into the tank of a paint gun. The gun was mounted on a carriage rolling on rails parallel to the projection surface so that the resin was strictly sprayed perpendicular to it at a constant distance of 20 cm. The projection surface was a copper plate covered by a Mylar film. A return trip of the paint gun at a fixed rate of a few centimeters per second was enough to get a composite film of thickness 100 μm after hardening.

Immediately after spraying, the filled resin deposited on its substrate was horizontally placed in a ventilated oven, in which a complex temperature ramp was applied. Such a process allowed a slow evaporation of the solvent and a concomitant crosslinking of the PU resin so that no bubble appeared in the thermoset composite films, whatever the FMG content. After cooling at room temperature, the composite film was carefully taken off the Mylar sheet. The obtained FMG / PU films had a typical area of 50 cm^2, and FMG contents ranging from 0 to 9 $vol.$ %. Samples were cut off such films for dielectric and conductivity measurements.

4.2 Experimental results

4.2.1 Graphene nanoplatelets / epoxy resin composites

4.2.1.1 Room temperature

The frequency dependence of the real part of the effective permittivity and the conductivity measured at room temperature is presented in figure 4.2.

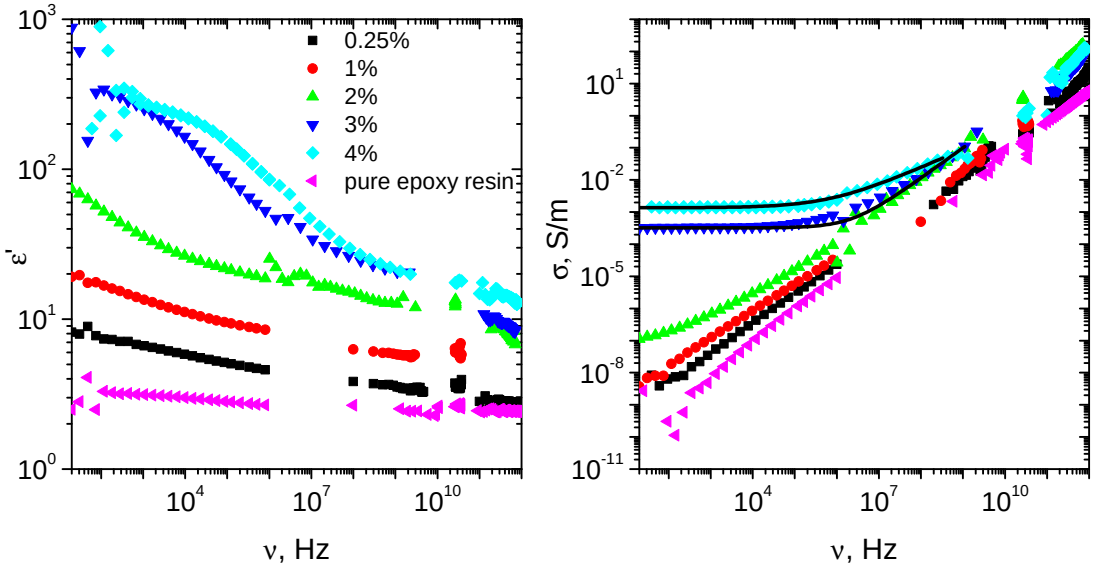

Figure 4.2: Real part of the effective permittivity (left) and conductivity (right) of epoxy resin and GNP/epoxy composites against frequency for different concentrations.

Both the static effective permittivity and dc conductivity increase with increasing concentration of GNPs and reach 300 and 1 mS/m respectively for composite with 4 $wt.$ % of GNP inclusions. For these composites the low-frequency dispersion of the real and the imaginary part of the permittivity can be described by Jonsher law [34, 35] (2.18).

The data indicate that the critical concentration between two conduction regimes lies between 2 and 3 $wt.$ % GNPs. Its value can be evaluated using the usual formula describing the conductivity σ *versus* the filler concentration p_{GNP} near the percolation threshold p_c [32] (2.16). Fitting the conductivity of the epoxy composites below the percolation threshold i.e. 0, 0.25, 1 and 2 $wt.$ % with first equation of (2.16) at a fixed frequency, here 117 Hz, yields p_c

= 2.3 $wt.$ % and s=1.8. The critical exponent exhibits slightly higher value than universal one [32, 106]. Such values can be also found in variety of composite materials [107, 108] and can be explained by inverse Swiss cheese model [106].

4.2.1.2 High temperature

The epoxy resin becomes conductive at high temperature. As a result, a dc plateau was observed in the conductivity frequency spectra of all composites, above and below the percolation threshold. The temperature variation of the permittivity and the dc conductivity of samples is presented on figure 4.3.

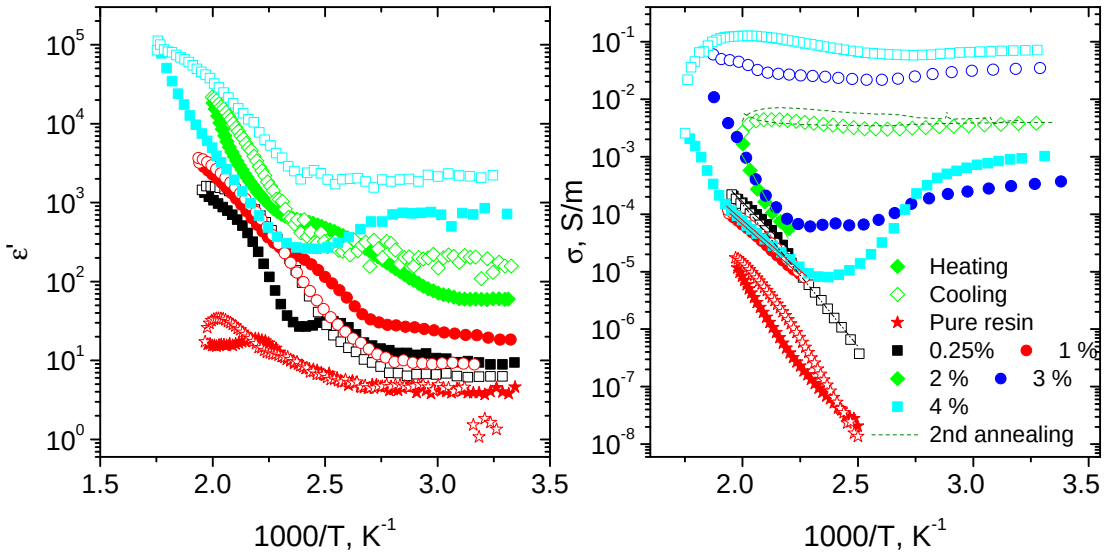

Figure 4.3: Temperature dependence of (left) the effective permittivity at 129 Hz and (right) the dc electrical conductivity measured on heating (solid symbols) and on cooling (open symbols) composite samples with different GNP concentrations.

The dc conductivity of composites with a low concentration of GNP (0.25 and 1 $wt.$ %) demonstrates small hysteresis on heating and cooling and can be fitted with Arrhenius law. For composites above the percolation threshold (3 and 4 $wt.$ %), three different dc conductivity regimes can be identified on heating: 1) at low temperatures (below 360 K), the dc conductivity is almost temperature independent; 2) in the intermediate temperature region – about 360 K – 390 K for the composite with 4 $wt.$ % GNP – the dc conductivity decreases with increasing temperature due to thermal expansion of the epoxy

matrix, which slightly increases the distance between conductive clusters; 3) at higher temperatures (above the glass transition in pure epoxy resin), the dc conductivity of the composites increases due to the finite conductivity of the epoxy matrix. A huge hysteresis between the first cooling and the first heating cycle is observed for composites filled with 2, 3 and 4 $wt.$ % of GNP. The hysteresis is followed by a drastic increase of the composite conductivity (up to six orders of magnitude). In addition, after annealing, the variation of the dc conductivity with T becomes flatter. Moreover, the sample with 2 $wt.$ % GNP has acquired a dc conductivity plateau at room temperature after annealing. The percolation concentration recalculated with second equation of (2.16) for percolated samples (2,3,4 $wt.$ %) gives p_c = 1.4 $wt.$ %. In other words, the percolation threshold has decreased substantially after annealing the samples. It is worth mentioning that the dc conductivity only slightly increases after a subsequent heating-cooling treatment (dashed-line curves in figure 4.3) and saturates after a few cycles.

Table 4.1: Shielding efficiency of 2 mm-thick composite layer at 30 GHz frequency

Sample	Reflectance, %	Transmittance, %	Absorbance, %
2%	45	22	33
2%, annealed	57	15	28
4%	70	14	16
4%, annealed	71	8	21

It was observed that GNP / epoxy composites lead to substantial EM attenuation in the microwave domain and are therefore interesting materials for shielding applications. A 2-mm thick sample with 4 $wt.$ % transmits only 14 % of initial radiation. Table 4.1 shows that annealing the samples improves their shielding ability significantly: the transmittance of the sample with 2 $wt.$ % shifts from 22% to 15% and from 14% to 8% for the 4 $wt.$ % sample. However, the variation of shielding behaviour is not the same for both compositions: for 2 $wt.$ %, sample annealing increases the reflection and slightly decreases the absorption whereas for 4 $wt.$ %, the reflection remains unchanged and the absorption increases.

The sample impedance (2.14) was employed to understand the observations. The frequency dependence of the measured impedance displayed in figure 4.4 cannot be described by that a single RC circuit $Z^* = R/(1+i\omega RC) = R/(1+i\omega\tau)$

(which form is very similar to the Debye equation for the dielectric dispersion). Instead, the Maxwell-Wagner relaxation of the impedance spectra was modelled by considering an infinite chain of RC circuits connected in series. The distribution $f(\tau)$ of relaxation times was calculated by solving the integral equation (4.1) with the Tikhonov regularization technique [109]:

$$Z^* = Z_\infty + \Delta Z \int_{-\infty}^{\infty} \frac{f(\tau)}{1 + i\omega\tau} d(\ln \tau). \tag{4.1}$$

As we can see from figure 4.4, equation (4.1) well fits impedance spectra at higher frequencies and lower temperatures (for example above 1 kHz at T = 425 K). At higher temperatures and lower frequencies, an additional dispersion is observed, which is caused obviously by non-ohmic contacts. The dispersion at lower frequencies can be taken into account using the equation (2.12) for two Cole-Cole processes. In this case, the maximum of the imaginary part of the lower frequency process occurs below 20 Hz, so the fixed relaxation time $\tau = 10\ S$ was taken for the fit.

The results are displayed in figure 4.5 for a composite sample containing 2 $wt.$ % of GNP. The maximum of $f(\tau)$ shifts to shorter relaxation times upon heating the samples and the distribution becomes narrower. Upon cooling (figure 4.5 (b)), the distribution of relaxation times stays almost temperature independent and peaks at 2.5 10^{-6} s. The results for samples with 3 and 4 wt.% GNP (not shown) has a similar behaviour as for 2 $wt.$ %, but the maximum of the imaginary part of their impedance shifted at higher frequencies. For all the compositions studied, the distributions of relaxation time are almost temperature-independent after the second and third annealing.

The relaxation time $\tau = RC \sim C/\sigma$ involves the capacitance C of a GNP cluster and the tunneling conductivity σ between neighborhood GNP clusters. The capacitance depends only on the geometry of the GNP clusters. Assuming a spherical shape, which for GNP is a rough approximation aimed at capturing the underlying physics, $C = 4\pi\varepsilon_0 r$ where r is an effective radius. The tunnelling conductivity between GNP clusters is dependent on their distribution inside the polymer matrix and on the GNP shape distribution. Schematically, short relaxation times come from small GNP clusters and short distances that charge carriers have to tunnel through. Long relaxation times is dominated by large GNP clusters and long distance between them. From the distribution of relaxa-

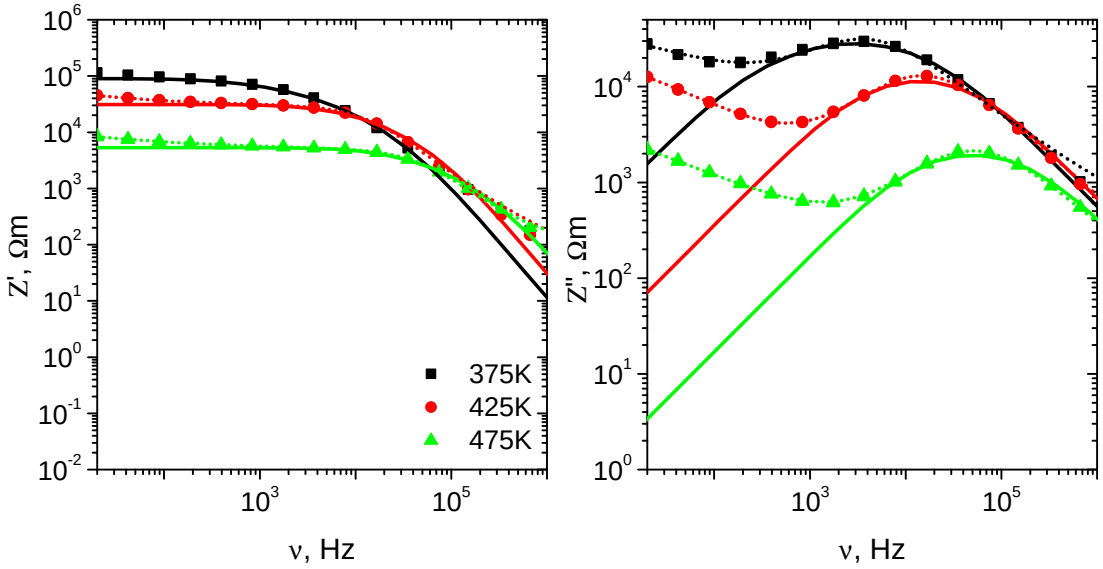

Figure 4.4: Real and imaginary parts of the impedance of a GNP / epoxy sample containing 2 $wt.$ % filler for three temperatures: experimental data (symbols), calculated with equation (4.1) (solid curves) and calculated with equation (2.12) (dotted curves).

tion of times shown in figure 4.5, it is difficult to extract the exact GNP cluster shape distribution. One can nevertheless deduce that, during heating, large GNP clusters separate into smaller ones and their distribution becomes more homogeneous (see figure 4.6). A better dispersion of small clusters decreases the tunnel barrier because the distribution of the distance between them becomes narrower. Decreasing the probability of long path across the epoxy matrix increases the tunnel conductivity in annealed samples. Moreover, the conductivity activation energy deduced by Arrhenius fit decreases with increasing GNP concentration, except at the concentration 2 $wt.$ % (Table 4.2).

What is an impact of composite annealing on the electromagnetic properties at different frequencies? It is possible to separate two cases:

1) The low frequency approximation, $\omega\tau_{max} << 1$ (where τ_{max} is the most probable relaxation time). In this case according to equation (4.1), $Z' = Z_\infty + \Delta Z$ and Z'' is very small. Under such conditions and according to equation (2.14) $\varepsilon'' >> \varepsilon'$ and $\varepsilon'' = \frac{\sigma_{dc}}{\omega\varepsilon_0}$.

2) The high frequency approximation, $\omega\ \tau_{max} >> 1$. According to equation (4.1), $Z' = Z_\infty$ and Z'' is again very small. In this case, ε'=ε_∞ (where ε_∞

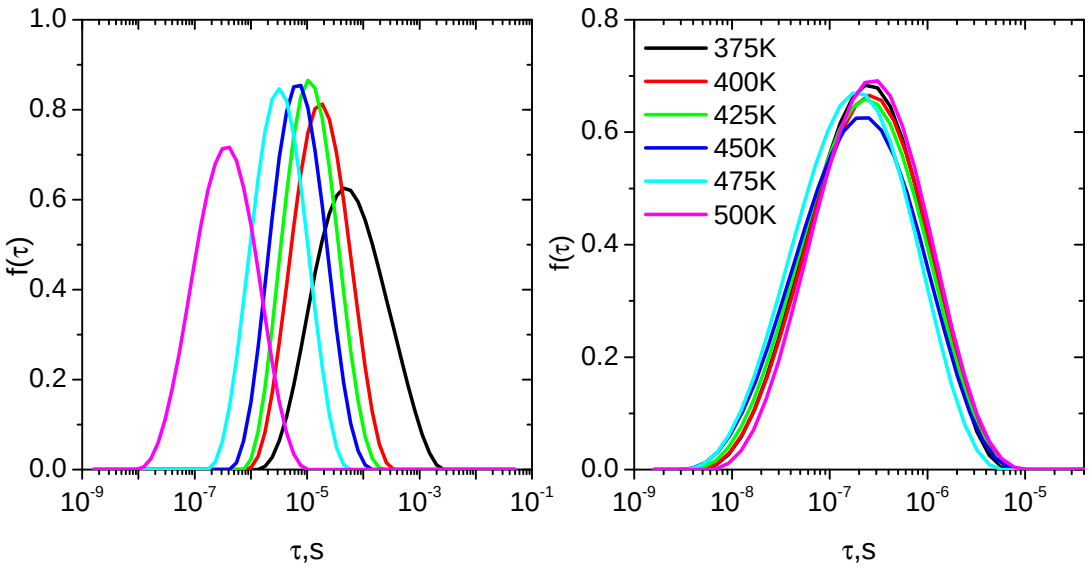

Figure 4.5: Distribution of relaxation times upon heating (a) and upon cooling (b) of composites with 2 $wt.$ % of GNP

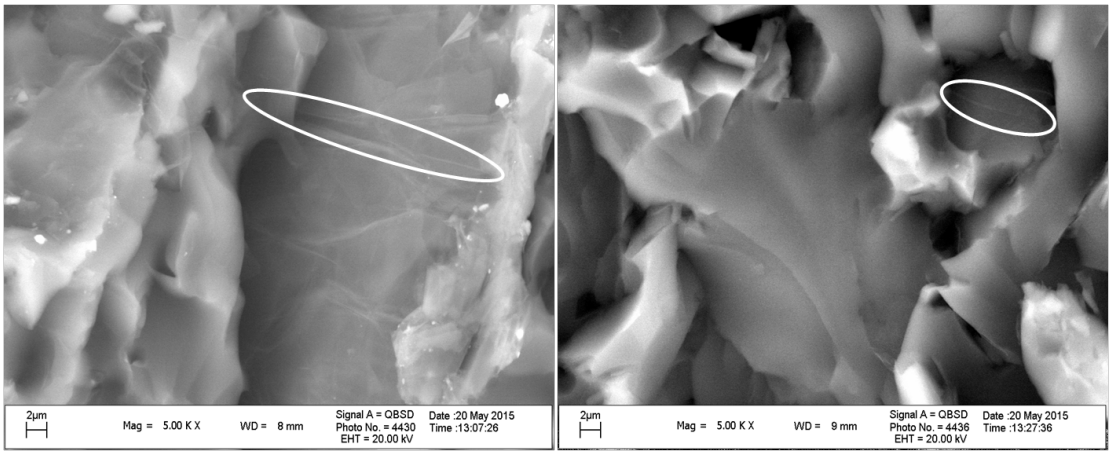

Figure 4.6: SEM image of epoxy / GNP composites containing 2 $wt.$ % of GNP before (see large GNP clusters marked with white oval) and after annealing (see small GNP cluster).

is caused by phonons and the electronic polarization) and ε''=1/($Z_\infty\omega\varepsilon_0$) are both very small and almost temperature independent. The highest impact of annealing is observed in low-frequency region 1) due to the increase in dc conductivity, while in the high-frequency region 2) the impact is negligibly small. In intermediate frequency range, when $\omega\tau_{max} \approx 1$, the impact of the annealing

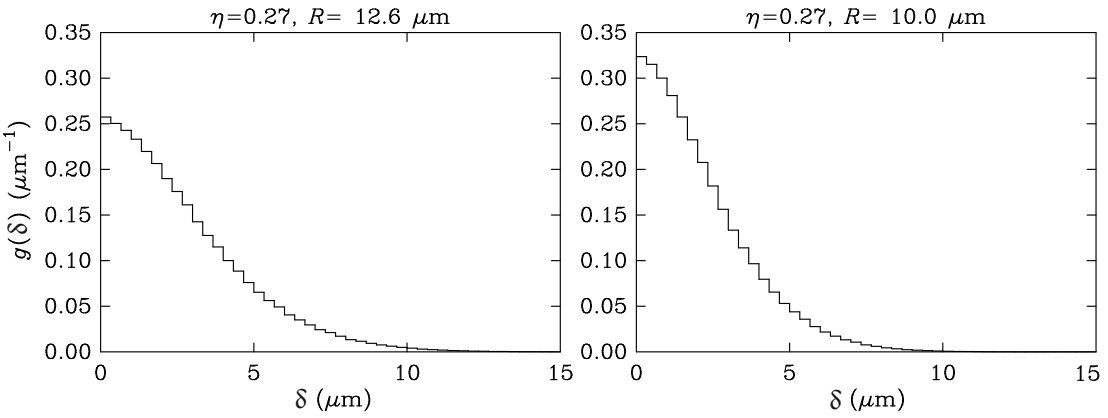

Figure 4.7: Distribution of separation distances between spherical clusters of 12.6 μm and 10 μm randomly and evenly distributed in epoxy. The results of this model calculation with volume filling fraction η = 0.27 mimic the composite with 2 $wt.$ % GNP before and after annealing, respectively (see text).

is also observed (Table 4.1), however lower than for dc regime.

The hypothesis that breaking the clusters into smaller ones by annealing could increase the conductivity of the composite samples can be substantiated with the results of the following model computation. Spherical clusters, with uniform radius, were randomly distributed in a cubic cell with periodic boundary conditions. The volume filling fraction was chosen at η = 0.27, which corresponds to 2 $wt.$ % concentration of GNPs in the epoxy resin at room temperature. The distribution $g(\delta)$ of closest approach distances δ between spheres was computed and averaged over many independent configurations. The precise definition of this distribution function can be found in equation (2) of ref. [110]. The calculations were performed for two radii R differing by a factor of $\sqrt[3]{2}$, 12.6 and 10 μm, as if each cluster were broken into two halves upon annealing. Figure 4.7 clearly shows that the distribution $g(\delta)$ becomes narrower upon reducing radius and its maximum shifts towards smaller separation distances δ. It is not a surprise since the theoretical function $g(\delta)$ for an equilibrium distribution of monodisperse hard spheres at a given filling fraction is a universal function of the ratio δ/R [110]. As a result, the width of the tunnel barrier between two clusters decreases with decreasing cluster size. The conductivity should therefore increase.

Table 4.2: Parameters of Arrhenius law fit

Sample,Process	$ln\sigma_0, S/m$	$E_a/k_B, K$	T.Region
0%, Heating [93]	12.51	12253	T $\geq$ 400
0%, Cooling [93]	17.1	14000	T $\geq$ 400
0.25%, Heating	10.1	9411.8	T $\geq$ 456
0.25%, Cooling	13.9	11379	T $\geq$ 450
1%, Heating	6.6	8112.9	T $\geq$ 446
1%, Cooling	6.7	8073.9	T $\geq$ 440
2%, Heating	26.5	16678	T $\geq$ 454
3%, Heating	26,1	1638	T $\geq$ 445
4%, Heating	11,49	1032,74	T $\geq$ 440

4.2.1.3 Low temperature region

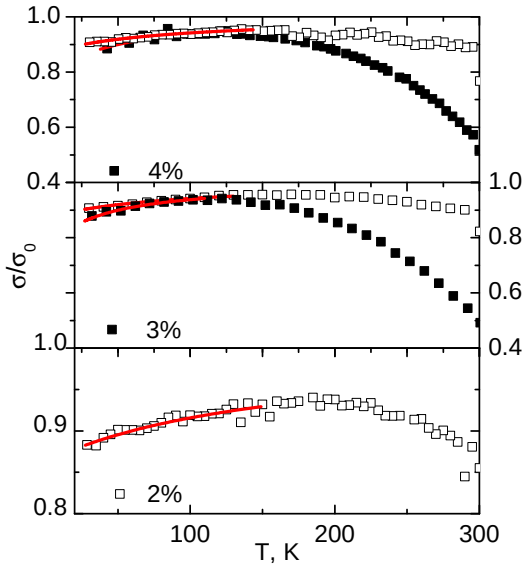

Figure 4.8: Temperature dependence of dc conductivity at low temperatures of GNP / epoxy composites with 2, 3 and 4 $wt.$ % GNP. Thee open symbols represent data for annealed samples, the black symbols correspond to as-produced composites. Non-annealed composite with 2 $wt.$ % is not represented because it is below the percolation threshold.

Composites above the percolation threshold were studied at low temperatures. The temperature dependence of their dc conductivity on temperature is plotted in figure 4.8. The dc conductivity of non-annealed samples with 3 and

4 $wt.$ % GNP has a maximum at 115 K. The increase of conductivity on cooling from 300 K down to 115 K can be explained by the thermal contraction of the epoxy matrix, which reduces the distance between clusters. After annealing, the maximum of conductivity shifts to 170 K and the temperature curve of σ becomes flattered at the higher temperature than for as-produced composites. As indicated by solid-line curves in figure 4.8, the observed conductivity behaviour below 170 K is well described by the tunnelling law [111] .

$$\sigma_{dc} = \sigma_0 \exp\left(-\frac{T_1}{T + T_0}\right) \tag{4.2}$$

where $k_B T_1$ represents the energy required for an electron to cross the insulating gap between GNP clusters and T_0 is the temperature above which thermally activated conduction over the barriers begins to occur. The parameters of the fits are listed in Table 4.3. Both T_0 and T_1 decrease with increasing concentration. Thus the electrical conductivity of GNP / epoxy composites is caused by the electron tunnelling through the insulating epoxy matrix. The potential barrier for such a process can be calculated by [111]:

$$k_B T_1 = U\epsilon_0^2 \tag{4.3}$$

and

$$k_B T_0 = \frac{2U\epsilon_0^2}{\pi\chi\delta} = \frac{2k_B T_1}{\pi\chi\delta}. \tag{4.4}$$

In these expressions, $U = \delta A/8\pi$ is a measure of the tunnel junction volume, $\epsilon_0 = 4V_0/e\delta$ is a pre-exponential factor and $\chi = \sqrt{2m_e V_0/\hbar}$ is the tunneling constant for electrons, where V_0 is the potential barrier, A and ω are the junction area and thickness of the insulating gap between conductive clusters. According to equations (4.3) and (4.4), $T_1/T_0 = \pi\chi\delta/2 = (\pi/2)\sqrt{2m_e/\hbar}\ V_0^{1/2}\delta$. It can be concluded from this relation that the observed decrease of the ratio T_1/T_0 by more than a factor of two after annealing (last column of Table 4.3) is equivalent to decreasing the potential barrier V_0 and the separation distance δ between conductive clusters. This can be understood in terms of the separation of large clusters into smaller ones and shorter average inter-distance.

Table 4.3: Parameters of tunneling law fit

p, %	$\sigma_0 \cdot 10^3$, S/m	T_1, K	T_0, K	T_1/T_0
3%	1.26	8.25	27.79	0.30
4%	5.25	8.06	22.64	0.36
2% annealed	10.76	22.02	148.04	0.14
3% annealed	37.34	11.49	81.75	0.14
4% annealed	94.29	10.30	71.59	0.14

4.2.2 Flat micronic graphite / polyurethane composites

4.2.2.1 Room temperature properties

The frequency dependence at room temperature of dielectric permittivity (ε') and electrical conductivity (σ') of PU-based composites with different FMG loadings is shown in figure 4.9. The corresponding values for composites with $p \leq 1\ vol.\ \%$ (where p is FMG volume fraction) are very low, similar to those of pure PU. However, the effective permittivity increased for composites with 2 $vol.$ % of inclusions. At low frequencies (below 1 kHz), a dc electrical conductivity plateau was clearly seen in conductivity spectra of composites with 2 $vol.$ % of filler, indicating that the percolation threshold in FMG / PU composites is close to 2 $vol.$ %.

The effective permittivity and electrical conductivity were very high for composites with 9 $vol.$ % of FMG at low frequency, of the order of 10^6 and 1 S/m, respectively. Such value of complex dielectric permittivity is very similar to those reported for composites based on functionalized carbon nanotubes near the percolation threshold [112].

Two different trends were observed in the frequency spectra of the dielectric permittivity: in the range 129 Hz – 3 kHz on the one hand, and in the range 3 kHz – 1 MHz on the other hand. In these frequency ranges, the dielectric permittivity decreased according to the Jonscher universal power law with different exponents [34]. The different dispersions are related to the Maxwell – Wagner contribution to the dielectric permittivity [113]. The loss tangent $tg\delta = \varepsilon''/\varepsilon'$ was also very high, indicating a high absorption ability of electromagnetic waves by composites filled with 2 – 9 $vol.$ % of FMG.

In order to explain the influence of the FMG concentration, the dielectric permittivity and the electrical conductivity at the frequency of 129 Hz and at room temperature were plotted as a function of concentration. It is worth noting

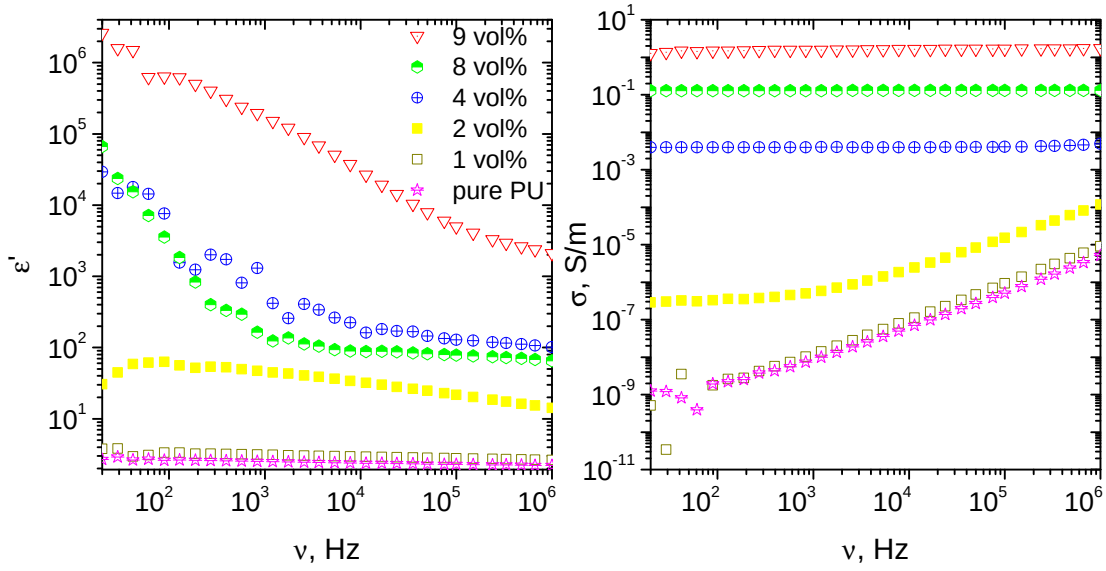

Figure 4.9: Frequency dependence of dielectric permittivity and electrical conductivity at room temperature.

that the frequency-independent dc plateau was observed at low frequency for composites with FMG concentration higher than, or equal to, 2 $vol.$ %, so that the conductivity at 129 Hz of these materials corresponds to their dc conductivity. Above the percolation threshold, the dielectric permittivity ε at 129 Hz and the dc electrical conductivity were fitted according to the classical law (2.16). Obtained percolation concentration is p_c = 1.9 $vol.$ %.

4.2.2.2 Electrical conductivity above room temperature

Above the percolation threshold, the electrical conductivity governs the dielectric properties of composites. The frequency dependence of the electrical conductivity for composites with 2 $vol.$ % FMG filler is presented in figure 4.10. One can observe a frequency-independent contribution to the conductivity at low frequency (which corresponds to the dc conductivity), and a contribution which increased with frequency, at higher frequencies. It can be assumed that dc conductivity increased with temperature, whereas the critical frequency at which the conductivity deviates from its constant dc value, decreased. Moreover, dc conductivity at room temperature after annealing became higher whereas the critical frequency decreased (see figure 4.10). The frequency dependence

of the electrical conductivity can be fitted according to the universal power law (2.18) [36]. The dc conductivity values for all investigated composites are presented in figure 4.11.

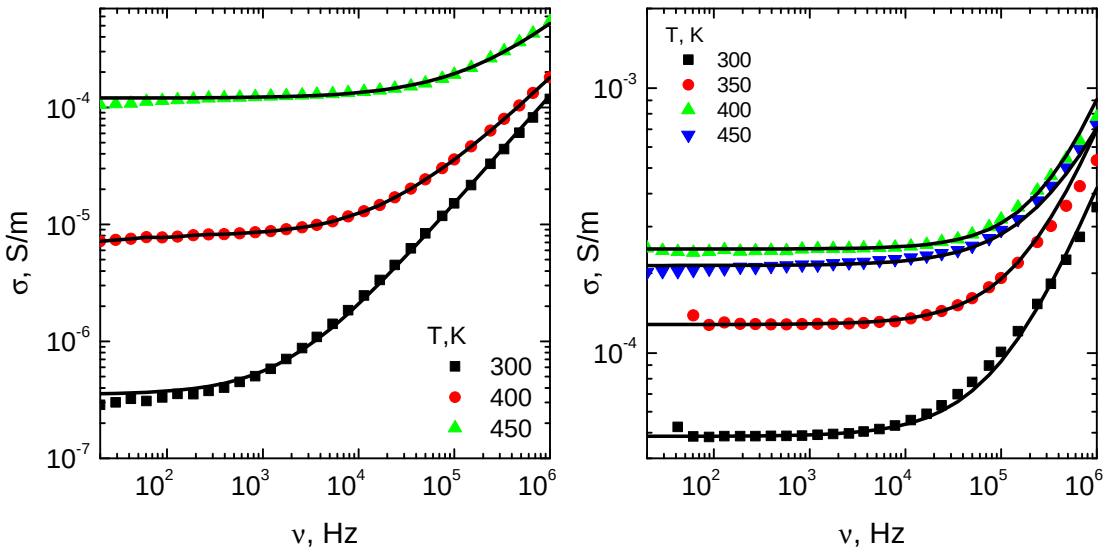

Figure 4.10: Frequency dependence of the electrical conductivity on heating (right) and cooling (left), measured values (symbols) and fitted with universal power law (solid curves)

For composites below the percolation threshold and for pure PU, dc conductivity values were obtained at higher temperatures only, above 350 K, i.e. above the glass transition temperature of pure PU, which is known to be about 330 K in the present case. The electrical conductivity for these samples is related to some mechanisms of conductivity throughout the polymer matrix occurring at sufficiently high temperatures and can be fitted by Arrhenius law.

For composites above the percolation threshold, the value of dc conductivity also increased upon heating, however the most pronounced rise of σ_{dc} occurred after annealing at 450 K. Then, on cooling, the temperature dependence of the conductivity was very limited.

In order to understand the impact of thermal treatment (heating / cooling) on composites' dielectric properties at different frequencies, the impedance formalism can be used (2.14). As-obtained frequency spectra of the complex impedance Z^* are presented in figure 4.12. The frequency dependence of Z^* is very broad and cannot be described by a single RC circuit. Instead, the similar

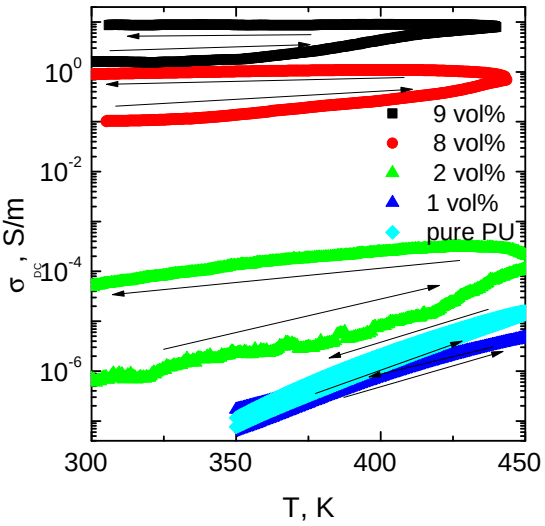

Figure 4.11: Temperature dependence of dc conductivity above room temperature. The arrows indicate heating and cooling.

technic as in section 4.2.1.2 (equation (4.1)) was used. It is important to note that the frequency spectrum of Z'' is almost symmetric at room temperature (see figure 4.12). On heating and cooling, the values of complex impedance $Z*$ decreased unevenly at different frequencies and the frequency spectra of Z^* became more asymmetric (figure 4.13).

The calculated distributions of relaxation times are presented in figure 4.14. The distributions of relaxation times exhibited pronounced temperature dependence (see figure 4.14). The maximum of the distributions was shifted from milliseconds to several microseconds with the decrease of annealing temperature, and the distributions became narrower. The most pronounced effect occurred after half an hour of isothermal annealing at 450 K. After annealing, the position of the maximum of the distribution of relaxation times indeed changed by two orders of magnitude. In contrast, on cooling, the distributions of relaxation times remained almost temperature-independent.

The similar tendency of the relaxation times behaviour was demonstrated in the case of GNP / epoxy resin composites 4.2.1.2. We can conclude that the similar effect of the dividing of big agglomerates into smaller one is observed here.

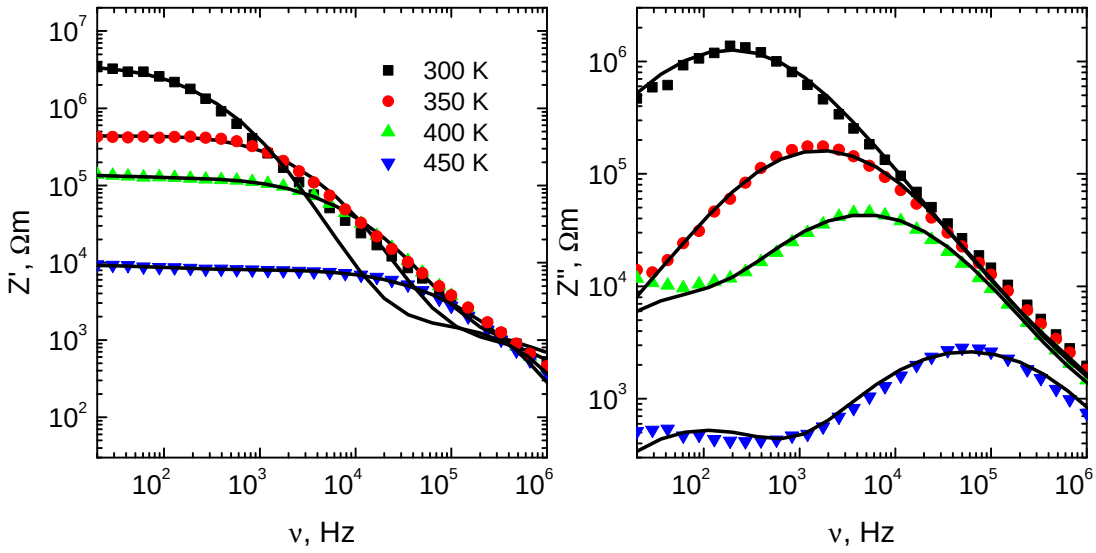

Figure 4.12: Frequency dependence of the complex impedance at different temperatures for composites with 2 $vol.$ % of FMG filler: experimental data (symbols) and calculated with equation (4.1) (curves)

4.2.2.3 Electrical conductivity below room temperature

The temperature dependence of dc conductivity on cooling below room temperature is presented in figure 4.15. Both dielectric permittivity and electrical conductivity demonstrated very low-temperature dependence, mainly caused by different thermal properties of FMG and pure polyurethane matrix.

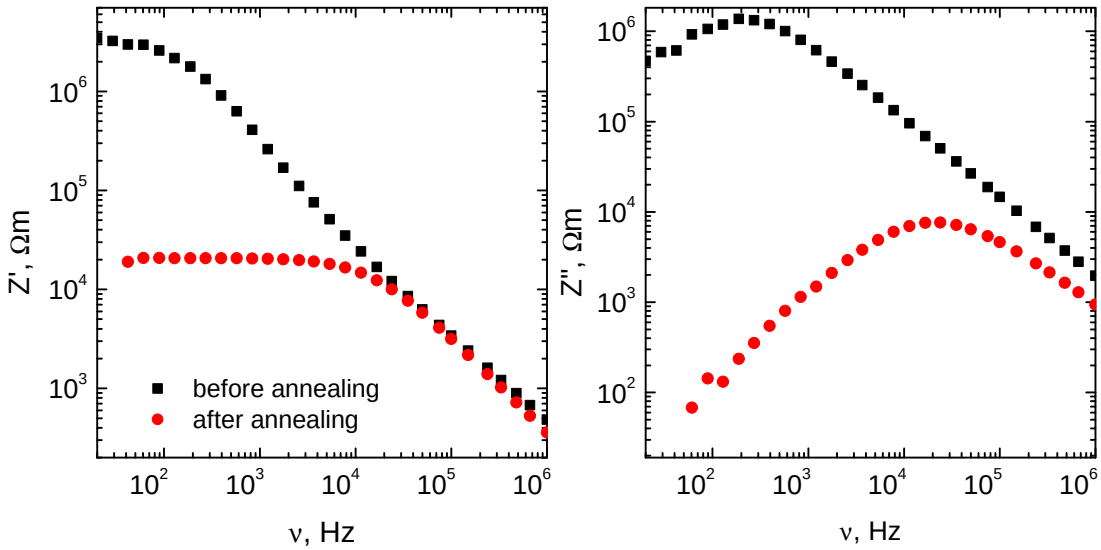

Figure 4.13: Frequency dependence of the complex impedance at room temperature before and after annealing for composites with 2 $vol.$ % of FMG filler

4.3 Summary

Two different types of composite materials with the similar effects have been studied.

Electromagnetic properties of epoxy composites containing the small addition of GNP have been studied over eight decades of frequency, from 20 Hz to 2 THz. It was demonstrated that the percolation threshold in such systems is 2.87 $wt.$ %. According to low-temperature analysis, the electrical conductivity occurs by a tunnelling mechanism.

The dielectric properties of FMG / polyurethane resin composites were presented in a wide temperature (25 – 450 K) and frequency (20 Hz – 1 MHz)range. It was established that the electrical percolation threshold lies between 1 and 2 $vol.$ % of filler. Above the percolation threshold, the composites exhibited huge values of dielectric permittivity and electrical conductivity. The materials above the percolation threshold also presented a huge hysteresis of properties on heating from room temperature up to above 450 K and subsequent cooling.

During the first annealing of samples close to and above the percolation threshold, a dramatic increase of both permittivity and conductivity was observed. In case of GNP / epoxy resin composites by a factor of 3 and by 4

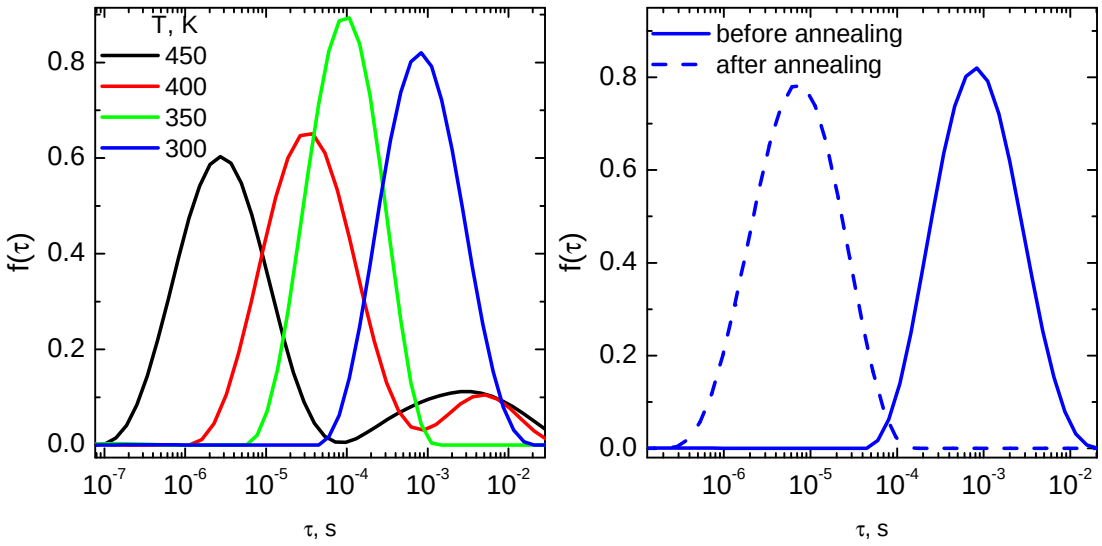

Figure 4.14: Distributions of relaxations times for composites with 2 $vol.$ % of FMG filler on heating (left) and at room temperature before and after annealing at 450 K (right)

orders of magnitude, respectively (for the 2 $wt.$ % GNP sample). For FMG / polyurethane composites the conductivity increased by more than 2 orders of magnitude.

Annealing was also demonstrated to be a simple way to improve significantly the shielding ability of GNP-based composites. Indeed, as-produced composite with 4 $wt.$ % GNP provided 86% of EM attenuation across a 2 mm-thick sample, while the same sample reached 92% after annealing. The same EMI shielding efficiency of 85% can be achieved with 2 $wt.$ % GNP after annealing.

This phenomenon was studied with the impedance formalism. It was found that Maxwell – Wagner relaxation occurs. Upon heating, the relaxation time τ decreases by several orders of magnitude and remains unchanged on cooling. The analysis points to a redistribution of GNP or FMG clusters during which the average size and, consequently, the separation between the conductive clusters decreases. This leads to a huge rise of conductivity and even pulls the percolation threshold down (for the GNP / epoxy resin composites). After a second or third annealing, no significant changes of the relaxation time and the conductivity was observed, indicating that the redistribution processes is achieved after the first thermal cycle.

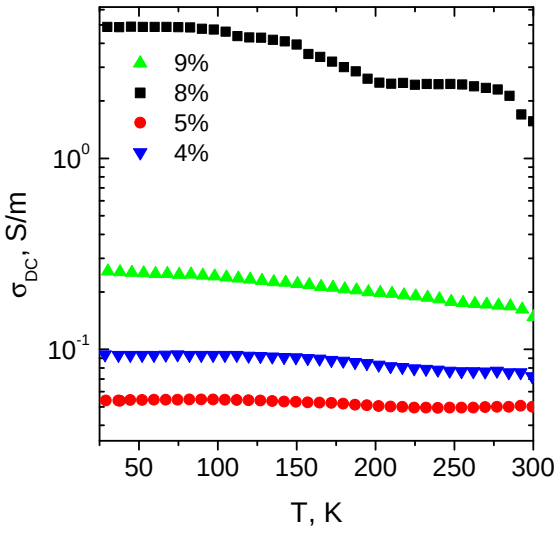

Figure 4.15: Temperature dependence of dc conductivity on cooling below room temperature.

The fact that the same effect was observed for two different systems moves us towards the proposal about the universality of this phenomenon. However, it is not so. For instance, the redistribution was not observed for the system of nanosized spherical Ni particles covered with few layers of carbon introduced into the polydimethylsiloxane (PDMS) matrix. PDMS in normal condition is already above the glass transition temperature (which is near 120 K), so we expected pronounced improvement on heating / cooling cycle. But such improvement was not observed (see figure. 4.16). One of the reason is that the composites were significantly lower the percolation threshold.

Such annealing proved to be a very simple but powerful way of improving significantly the electrical and dielectric properties of composites based on carbon fillers. Such noteworthy annealing effect was unambiguously observed, despite the rather big size of the graphite particles and the thermoset nature of the polymer matrix. We assume that annealing is a cheap and simple procedure for producing materials with well-dispersed carbonaceous inclusions for high-frequency applications.

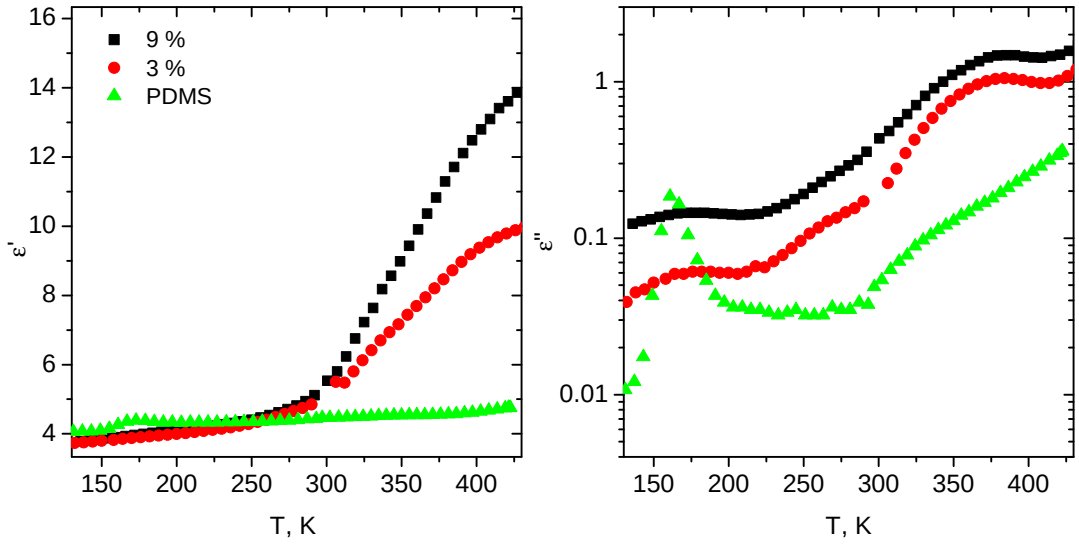

Figure 4.16: Temperature dependence of the dielectric permittivity of the Ni@C / PDMS composites.

Chapter 5

Synergetic effect of triglycine sulfate and graphite nanoplatelets on dielectric and piezoelectric properties of epoxy resin composites

Composite materials filled with the ferroelectric inclusions are widely studied for decades [108, 114, 115, 116]. The broad range of possible applications of these materials in microelectronics includes, for example, microwave substrates [117], 3D antennas, embedded capacitors [118] and inductors [119, 120], and electromagnetic shields [121].

The second point is that the ternary composites with GNP and an additional filler are promising due to the possibility of simple surface modification[122]. Also, the addition of the third phase in nanocarbon / polymer composites may drastically change the distribution of carbon particles and, as a result, their dielectric properties [123, 124, 125]. Even the optimal amount of the third phase may be figured out [126].

Designing ternary composites with carbon and ferroelectric inclusions embedded into polymer matrices is a way to combine the advantages of both fillers [127, 128, 129, 108]. Several authors indeed demonstrated significant improvement of electromagnetic wave absorption properties of such systems, energy storage properties [19] and electronic device applications [20].

Triglycine sulfate (TGS) is one of the most well-studied ferroelectric crystal with a second-order ferroelectric phase transition close to 322 K [130]. The

ferroelectric phase transition is of order-disorder type with strong dielectric dispersion in the microwave frequency range and a typical critical slowing-down effect [131]. TGS crystals also present huge values of dielectric permittivity, piezoelectric and pyroelectric coefficients, enabling a wide range of applications, including highly sensitive infrared sensors.

It is also known that polycrystallinity [132], moisture [133, 134], and doping with either organic or inorganic impurities [135] may significantly affect TGS properties. It is therefore worth investigating the possibility of designing composite materials based on epoxy resin filled with both TGS particles and conductive inclusions. As for the latter, graphite nanoplatelets (GNP) were used. The main ideas are the following: (i) being embedded in epoxy resin, TGS can be protected from ambient moisture; (ii) by introducing various amounts of conductive filler, the dielectric and ultrasonic properties of the composites can be controlled so that polymer composites with improved dielectric and electromagnetic properties can be produced through an easy and cost-effective method.

5.1 Sample preparation procedure

A single TGS crystal was first dissolved in distilled water. Next, the solution of TGS was evaporated overnight in an oven heated at 360 K. After complete evaporation of water, the solid residue was collected and ground in an agate mortar for 2 – 3 minutes. As a result, a powder of TGS crystallites was obtained. According to scanning electron microscopy (figure 5.1 (a)), the average size of TGS crystallites was around 50 μm. GNP particles were obtained by a succession

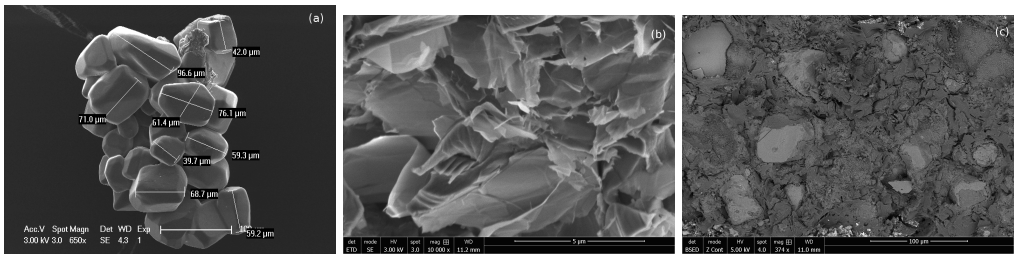

Figure 5.1: Scanning electron microscopy images of: (a) TGS crystallites; (b) GNP particles; and (c) composite material loaded at 30 and 0.5 $wt.$ % of TGS and GNP, respectively.

of grinding and sonication steps applied to a suspension of exfoliated graphite in cyclohexane. GNP particles had an average diameter of 10 μm, and a typical thickness of 0.1 μm. In other words, their aspect ratio was as high as 100 [136]. The composites were prepared as follows. GNP and TGS particles were sonicated in isopropyl alcohol for 3 hours. Next, degassed epoxy resin (Buehler EpoThin 2) was introduced into the solution, and the blend was sonicated for 1 additional hour. The homogeneous solution was then placed into an oven at 330-340 K until complete evaporation of the alcohol. After evaporation, the system was sonicated again for one more hour. When homogenisation was finished, the curing agent was introduced and the obtained system was carefully stirred manually for 5 minutes and poured into the moulds for curing. Composites were cured overnight at room temperature first, then for 5 hours at 350 K. Based on the aforementioned protocol, samples with either 0 or 30 $wt.$ % of TGS and 0, 0.5, or 1 $wt.$ % of GNP were prepared. Scanning electron microscopy (figure 5.1 (b,c)) demonstrated that both GNP and TGS inclusions were well-dispersed. No percolation paths between TGS crystallites were observed, so the connectivity of the composite may be assumed to be 0-3, since the polymer matrix is interconnected along the 3 directions, while TGS crystallites are not, along with any direction. In the following, samples were referred to as wt_{GNP}GNP-wt_{TGS}TGS, where wt means weight concentration.

5.2 Experimental results

5.2.1 Dielectric properties at room temperature

The frequency dependence of the complex dielectric permittivity for all studied composites at room temperature is presented in figure 5.2. As it can be seen from the figure, the addition of either TGS or GNP led to an increase of both real and imaginary parts of the complex dielectric permittivity. In order to understand the influence of the addition of each component on the dielectric properties of composites, the following approach was used. The behaviour of the TGS / epoxy binary system may be predicted by Jayasundere and Smith model of the 0-3 composite with dielectric matrix and piezoelectric inclusions [137]. On the other hand, the concentration behaviour of the dielectric properties of GNP / epoxy composites may be described with a simple universal power law, or

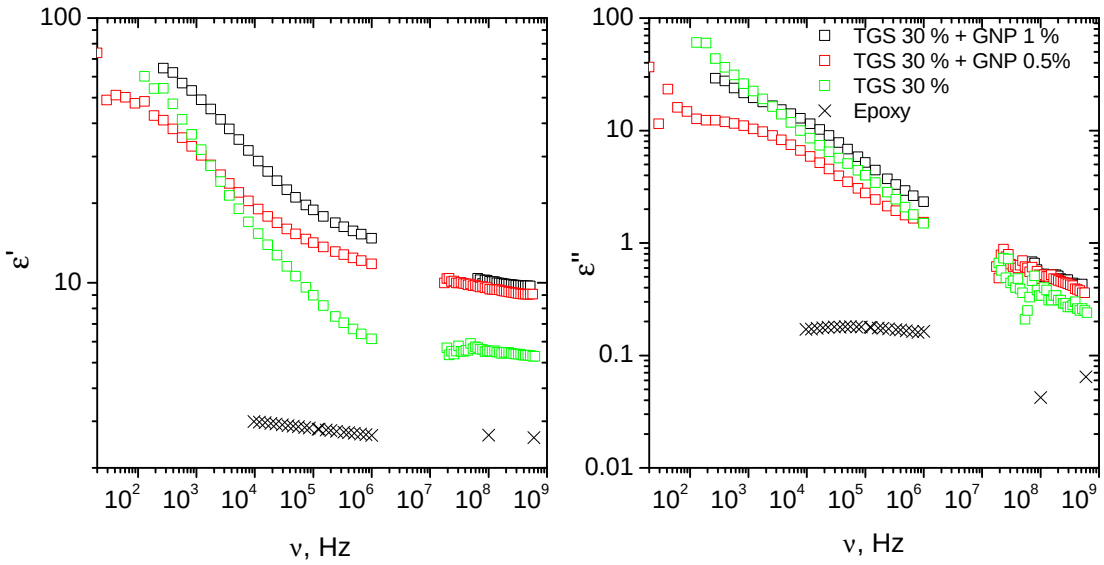

Figure 5.2: Frequency spectra of dielectric permittivity of pure epoxy and of composite materials filled with 30 $wt.$ % of TGS and different amounts of GNP at room temperature.

with the Maxwell-Garnett equation [65, 66]. But in the case of ternary TGS + GNP / epoxy system, the combination of those models might fail at high filler concentrations due to the following reasons. Considering a composite whose total volume is equal to V_0, then the volumes occupied by TGS and GNP particles are V_{TGS} and $V' = V_0 - V_{TGS}$, respectively. Therefore, the local volume concentration of GNP in the region between TGS particles should be higher than in a binary GNP / epoxy system having the same overall concentration of GNP. The percolation network should thus appear at a comparatively lower weight concentration. On the other hand, TGS crystals may introduce additional barriers preventing contacts between conductive GNP clusters. These two effects are antagonistic so that the final properties of ternary composites should be more sensitive to the microstructure than binary ones.

In the present case, a slight enhancement of dielectric properties was observed for xGNP-30TGS composites with respect to xGNP-0TGS at lower frequencies (see figure 5.3, mainly because: (i) the studied concentration range (0 – 1 $wt.$ %) of GNP was lower than the percolation threshold [138], (ii) the amount of TGS was quite high, so it is most likely that TGS particles acted as additional barriers in the conductive GNP network. The dielectric permittiv-

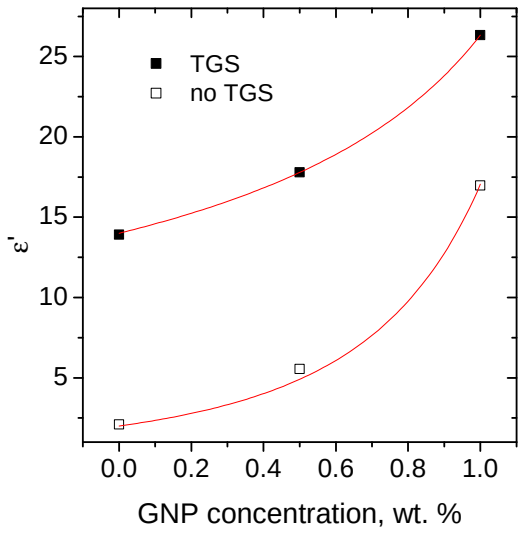

Figure 5.3: Comparison of dielectric permittivity of xGNP-30TGS and xGNP-0TGS at a frequency of 16667 Hz. Solid lines are fit with equation (2.16)

ity and dielectric losses strongly decreased with frequency for all composites. Two different dielectric dispersion trends could be distinguished: one at lower frequencies (20 Hz – 1 MHz), where the dielectric permittivity was strongly frequency-dependent, and another one at higher frequencies (above 1 MHz), where dielectric losses were quite low (lower than 1) and the dielectric permittivity was almost frequency-independent.

The dielectric dispersion at lower frequencies can be caused by the dynamics of ferroelectric domains, similarly as in pure TGS crystals, or by the Maxwell-Wagner relaxation due to the high electrical conductivity of GNP, the random orientation of TGS crystallites, and their finite value of electrical conductivity. However, the contribution of ferroelectric domains dynamics should be neglected because the dielectric dispersion remains far above the phase transition temperature. Therefore, the main contribution at low frequencies comes from the Maxwell-Wagner relaxation. It means that the differences in dielectric properties of composites at lower frequencies are mainly related to the structure of conductive clusters.

On the other hand, at higher frequencies at which the impact of GNP on the dielectric permittivity is more significant, the contribution of ferroelectric soft mode, typical of TGS crystals, might also be substantial. In other words,

the ferroelectric polarization of TGS clusters may be affected by the presence of GNP because: 1) the distribution of TGS crystallites is more homogeneous due to the presence of GNP, 2) GNP particles (due to their high electrical conductivity) create electric fields inside the composite, which affect the polarization inside TGS crystallites. Both contributions should be important in the present composites.

5.2.2 Dielectric properties above room temperature

The maximum of dielectric permittivity close to T=322 K for all studied composites is typical of the ferroelectric transition in pure TGS crystals, except the substantially lower dielectric permittivity peak value due to the random orientation of TGS crystallites (see figure 5.4). The variation of dielectric permittivity near the Curie temperature is governed with Curie-Weiss law 2.19 both in paraelectric and ferroelectric phase (figure 5.4), although with a different value of the constant C. The corresponding parameters of the fits of equation (2.19) are collected in Table 5.1.

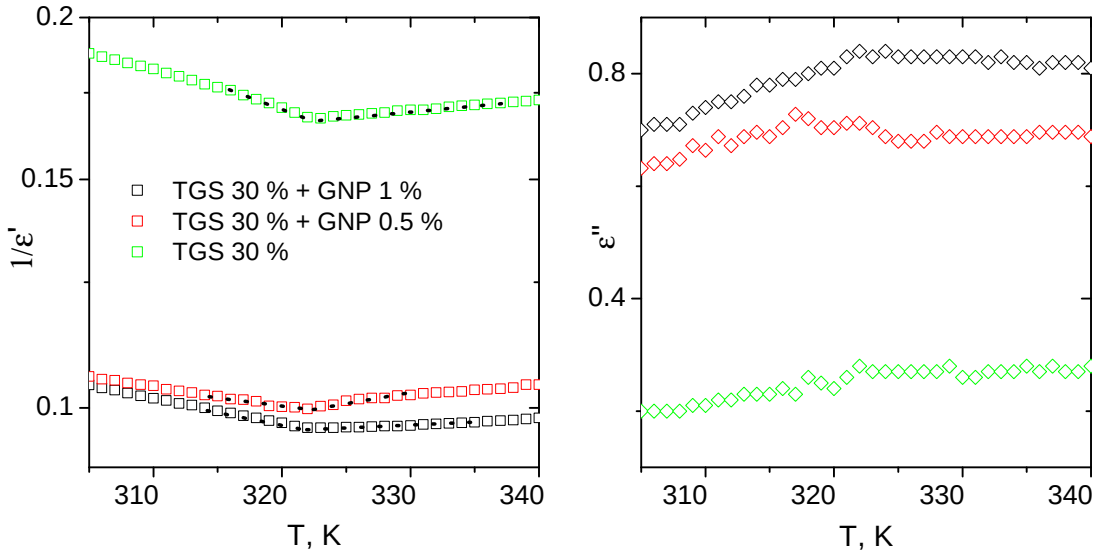

Figure 5.4: Temperature dependence of the dielectric permittivity of composite materials filled with 30 $wt.$ % of TGS and different amounts of GNP above room temperature, and at frequency 0.8 GHz. Lines are fits with equation (2.19)

The Curie constants C and C' increased with the GNP concentration, due to the rise of dielectric permittivity. The Curie-Weiss behaviour is usually related

Table 5.1: Parameters of the fits of equation 2.19 to the data of figure 5.4; C and C' are the constants of equation 2.19 for para- and ferroelectric phases, respectively.

Sample	C', K; ferroelectric phase	C, K; paraelectric phase
0GNP-30TGS	854.24	3235.42
0.5GNP-30TGS	3023.05	4509.23
1GNP-30TGS	2217.91	10428.83

to ferroelectric soft mode: either resonant or relaxational [139]. For TGS crystals, the relaxational soft mode is usual [139].

It can also be seen that the addition of GNP did not affect the temperature of the phase transition. However, it increased the absolute value of the complex permittivity in a broad temperature range, especially the real part, while the shape of the curves roughly remained the same. This should be due to the strong synergy effect between TGS particles and GNP. Indeed, the contribution of the Maxwell-Wagner relaxation (which appears at the dielectric / GNP interface) to the dielectric permittivity should not present an anomaly close to the ferroelectric phase transition temperature. Such a contribution should strongly increase with temperature. This was not the case for the composites investigated here.

The temperature dependence of dielectric permittivity of 0.5GNP-30TGS at different frequencies is shown in figure 5.5 . The same typical behaviour was also observed for all investigated composites.

It is clearly seen that at higher frequencies (above 1 MHz), a more pronounced maximum of permittivity appears at a certain intermediate temperature close to 322 K. In contrast, at lower frequencies (below 1 MHz), the dielectric properties are mostly governed by the Maxwell-Wagner relaxation, i.e., are thermally activated and almost not affected by the ferroelectric phase transition.

The frequency dispersion in the high-frequency range (above 1 MHz) can be well described by the universal Jonscher law [34, 35] (see figure 5.6):

$$\chi(\omega) = \varepsilon(\omega) - \varepsilon_\infty = A(T)(i\omega)^{n(T)-1} \tag{5.1}$$

where $A(T)$ is a temperature-dependent parameter and is a suitable "high-frequency" value of the permittivity at which the low-frequency losses become negligible. The exponent $n(T)$ is weakly temperature-dependent and is smaller than unity. This law states that real and imaginary parts of $\chi(\omega)$ have the same

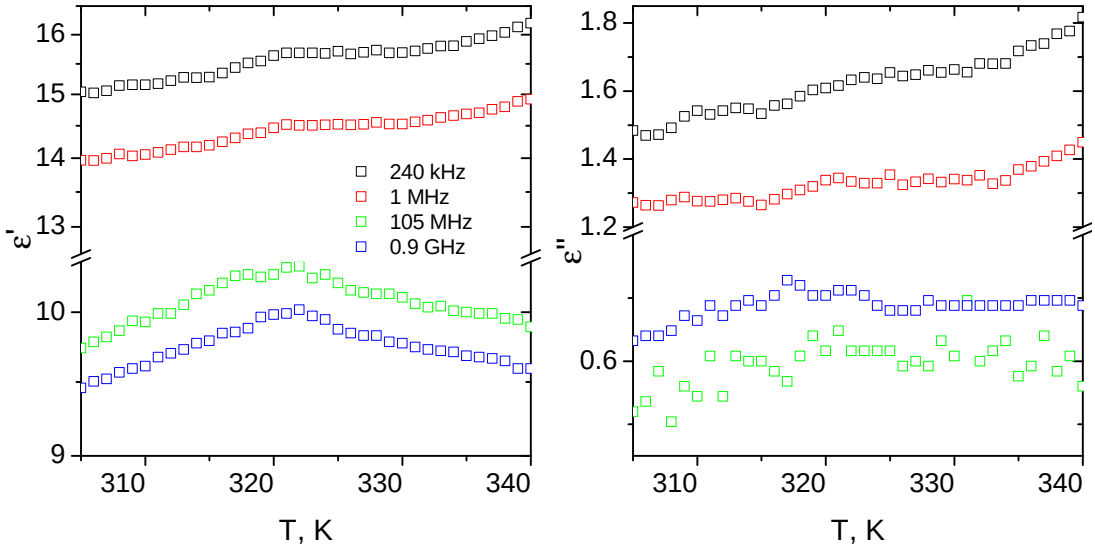

Figure 5.5: Temperature dependence of the dielectric permittivity of composite materials filled with 30 $wt.$ % of TGS and 0.5 $wt.$ % of GNP at different frequencies.

frequency dependence:

$$\frac{\chi''(\omega)}{\chi'(\omega)} = cot(\frac{\pi n}{2}) \tag{5.2}$$

The universal law is associated with many-body interactions between dipoles or charges responsible for polarisation in dielectrics. The parameters of equation 5.2 describing the frequency dependence are collected in Table 5.2.

Table 5.2: Parameters of the fits of equation (5.1) to the data of figure 5.6

Temperature, K	0GNP-30TGS		0.5GNP-30TGS		1GNP-30TGS	
	n	ε'_∞	n	ε'_∞	n	ε'_∞
315	0.92791	3.3	0.81849	8.1	0.74336	9.1
320	0.92083	3.4	0.80642	8.1	0.75913	9
322	0.9177	3.5	0.81328	8.3	0.79987	9
325	0.92083	3.4	0.81328	8.2	0.82416	8.8
330	0.92711	3.1	0.80304	8.1	0.81218	8.7
335	0.9177	3.2	0.8091	8.1	0.81648	8.6
340	0.90521	3.4	0.80059	8.0	0.81788	8.6

It can be seen that the values slightly depended on temperature, especially ε_∞ demonstrated maxima close to the phase transition temperature for all studied

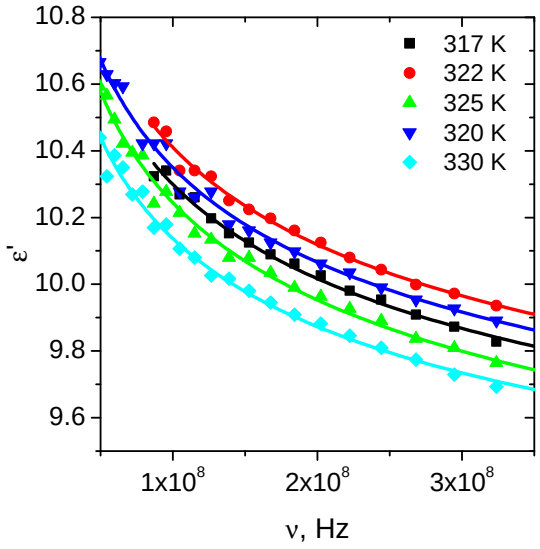

Figure 5.6: Frequency dependence of the dielectric permittivity of composite materials filled with 30 $wt.$ % of TGS and 0.5 or 1 $wt.$ % of GNP at different temperatures. Solid lines are fits with equation (5.1).

samples. However, those values strongly depended on the GNP concentration. Firstly, ε_∞ obviously increased with the concentration, but at the same time, the value of n decreased. This may be explained as follows: below the percolation threshold, the GNP loading made the real part of the permittivity increase faster than the imaginary part.

At lower frequencies the Maxwell-Wagner relaxation of composites takes place. For Maxwell-Wagner relaxations analysis, it is more convenient to use the diectric modulus formalism (2.13) (see figure 5.7). The imaginary part of the dielectric modulus demonstrate a maximum at certain frequency. The relaxation times can be calculated as the inverse of the frequency at which the imaginary part of the electrical modulus is the highest, i.e., $\tau = 1/f_{max}$. The variation of the relaxation times at different temperatures was tracked out and the results are presented in figure 5.8.

Such behaviour of the frequency dependence of the electrical modulus was observed only in ternary composites. The interfacial polarisation likely occurred at the conductive GNP clusters and TGS interfaces. The relaxation time τ obtained from the electrical modulus is proportional to the resistivity R and to the capacitance of conductive clusters C, i.e., $\tau = RC$. Now, the capacitance only depends on the geometry of the GNP clusters. Assuming a spherical shape,

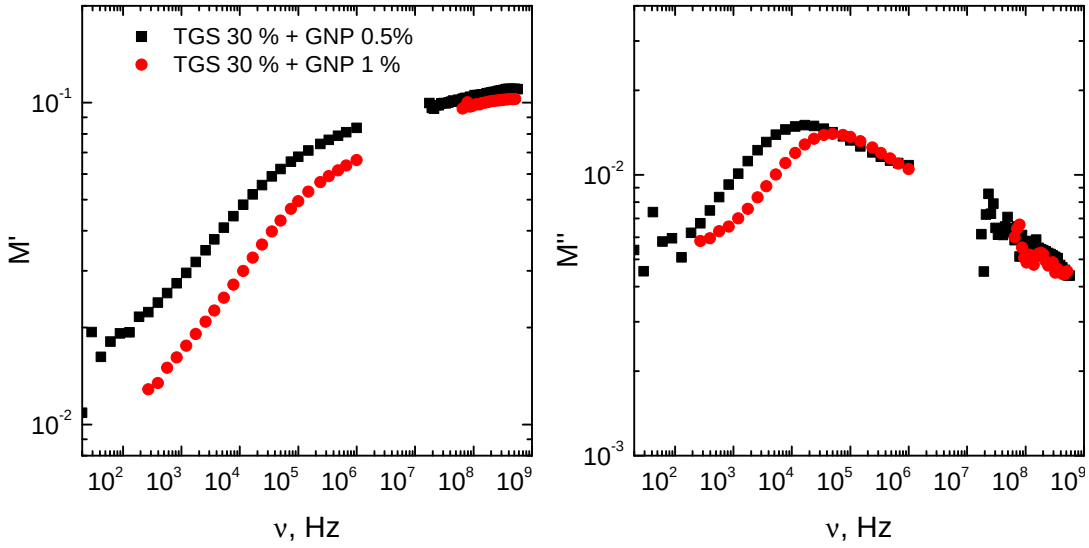

Figure 5.7: Frequency dependence of the electric modulus of composite materials filled with 30 $wt.$ % of TGS and 0.5 or 1 $wt.$ % of GNP at 345 K.

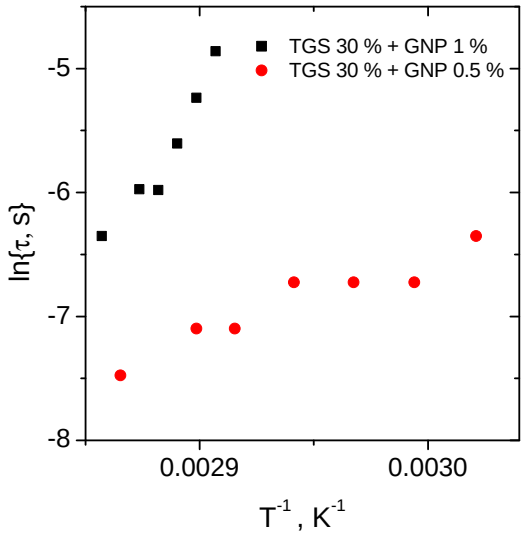

Figure 5.8: Temperature dependence of the relaxation time for the same ternary composites as in figure 5.7

which for GNP is a rough approximation, aimed at capturing the underlying physics, $C = 4\pi\varepsilon_0 r$, where r is an effective radius. Bigger conductive clusters thus lead to lower electrical conductivity and to higher capacitance, and hence to longer relaxation times [140]. Therefore, the biggest clusters are present in composites only containing TGS inclusions, and the smallest ones are in 0.5GNP-30TGS. The Maxwell-Wagner relaxation is related to the onset of conductivity at higher temperatures or higher GNP concentration.

5.2.3 Piezoelectric properties

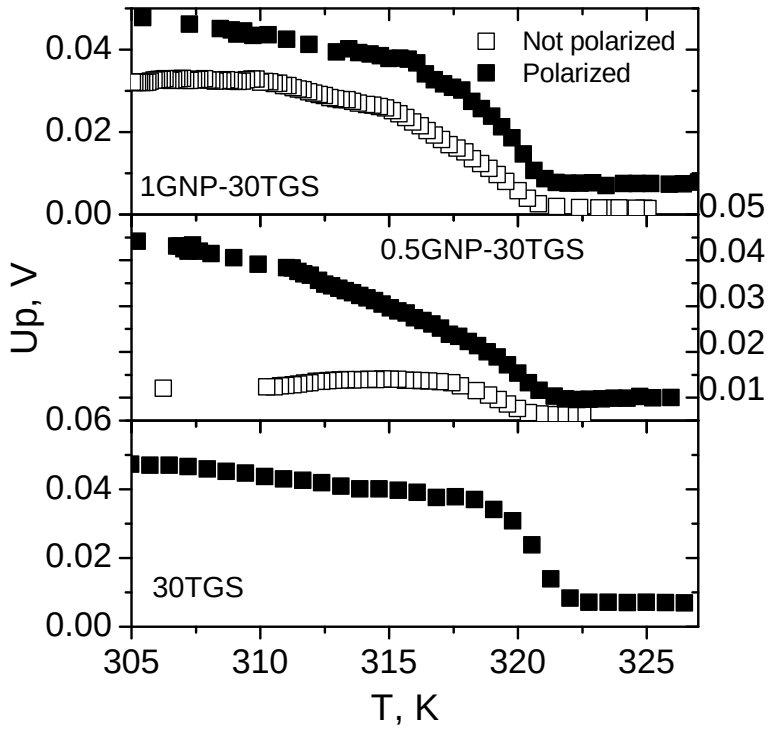

Figure 5.9: Piezoelectric response of composite materials either polarised with an external field of 400 V/mm (solid symbols) or not polarised (open symbols).

Figure 5.9 presents measurement results of piezoelectric properties of composite materials. The temperature dependence of the piezoelectric voltage at 10 MHz frequency exhibited the ferroelectric phase transition at 322 K. Above the transition temperature, the piezoelectric signal of non-polarized samples vanished, but it kept a finite value in the paraelectric phase for the polarised

samples. The signal in the paraelectric phase is caused by the electrostriction effect [141]. It can be demonstrated that the detected piezoelectric signal varies with temperature in the same manner as the order parameter [54, 142]. It was clearly seen that adding GNP provides a strong synergy effect. Composites with only TGS particles indeed did not show piezoelectric response without external polarisation field. Addition of 0.5 $wt.$ % of GNP significantly changed the situation: a weak piezoelectric response appeared even without an external electric field. Finally, adding 1 $wt.$ % of GNP provided a strong piezoelectric response without external polarisation. Even more, the difference between responses with and without polarisation decreased when increasing the GNP amount. Similarly, as in the case of dielectric properties, two possible reasons for this behaviour can be indicated. On the one hand, the loading of GNP obviously impacts the distribution of TGS crystals. Being more homogeneous, composites with TGS and GNP provide the highest piezoelectric response. On the other hand, the addition of GNP might improve the mechanical and electrical properties of epoxy. Two possible mechanisms of influence of the epoxy properties may be figured out. Firstly, by excitation with ultrasonic waves, the TGS crystals generate charges on their surfaces. The nearby regions thus accumulate the charges. Since the concentration of GNP is quite low (below the percolation threshold), the GNP loading provides a capacitive impact, while the conductivity of the samples remains low and appearance of the loss currents is impossible. Due to higher capacitance, the GNP / epoxy composite media which surrounds the TGS crystallites may accumulate electric charges better. The field created by those charges provides additional polarisation of TGS. Thus, the increase of GNP concentration should provide the higher piezoelectric response of samples without external polarisation. Secondly, it is known that the addition of carbon inclusions improves the mechanical properties of the polymers. Due to that, the ultrasonic waves might propagate throughout with fewer losses than in pure polymers. So, through hardening by GNP addition, composites should present higher piezoelectric properties.

5.3 Summary

Epoxy resin composites with 30 $wt.$ % inclusions of TGS and up to 1 $wt.$ % inclusions of GNP demonstrate ferroelectric properties. The ferroelectric phase transition in these composites was confirmed by the dielectric anomaly and the appearance of piezoelectric properties in the low-temperature phase (below the Curie point). The dielectric properties are mainly governed by the Maxwell-Wagner relaxation (below 1 MHz) and the ferroelectric soft mode (above 1 MHz). Although the ferroelectric phase transition temperature in ternary composites is the same as in pure TGS crystals, GNP and TGS particles demonstrate an evident synergy effect in dielectric and piezoelectric properties. Below their percolation concentration, more GNP nanoparticles lead to an increase of both dielectric permittivity and piezoelectric signals in a broad temperature range. The effect can be explained by a better distribution of particles, an improvement of the mechanical properties, and the creation of internal electric fields by GNP. Therefore, GNP addition should be considered as a relevant and easy way of improving the ferroelectric properties of ternary polymeric composites with ferroelectric and GNP inclusions.

Chapter 6

Numerical modelling of the percolation process in composites with randomly distributed nanoinclusions

As it was previously demonstrated, one of the main parameters of composite systems is the percolation threshold. Generally, the percolation threshold for multi phase irregular media is a problem that was studied for a long time (see [143, 144] and Refs. therein). In modern material science, the main focus is the percolation phenomena in composite with randomly distributed carbon nanoinclusions like graphite nanoplatelets, carbon nanotubes, carbon black, onion-like carbon, etc. [138]. There are many approaches to simulate the nanocarbon composite system. For the case of nanotubes or fibers, the most obvious is to simulate it as a caped [145, 146] or non-caped [69, 147] cylinder.

However, this approach is not universal because it does not allow to simulate all possible geometries of nanoinclusions (2D, 1D, and 0D). All mentioned objects may be roughly modelled as ellipsoids of revolution with a different axial ratio. Many papers contribute to the modelling of the percolation threshold of overlapping ellipsoids [148, 149, 150]. The method of overlapping inclusions is faster; it describes the transport properties in porous media well [151], as well as the social phenomena [152], *etc*. However, it is not accurate in the case of nanocarbon composites, because these particles are robust and cannot overlap. Very few papers contribute to the modelling of the percolation threshold for the

suspension of the non-overlapping ellipsoids [153, 154].

It was shown, that the percolation concentration is related with fillers' aspect ratio as $p_c \sim 1/AR$. Knowledge of the percolation threshold concentration for the particular filler allows predicting the samples' properties. The situation is easy and predictable for the case of one type of filler, but only a few papers contribute to the numerical study of the systems with two or more types of fillers introduced into the matrix [18].

In this chapter, we present the Monte Carlo model for the calculation of the percolation of the non-overlapping ellipsoids distributed inside a cubic unit cell. The dependence of the percolation threshold on the ellipsoids' distribution, unit cell size and the aspect ratio for the case of oblate and prolate ellipsoids was studied. The model was successfully used for calculations of the hybrid composites (2D + 1D fillers mixture).

6.1 Modelling details

The model generates the system of non-overlapping ellipsoids of revolution located inside the cubic unit cell. The dimensions of the unit cell are $UC = nd$, where d is the maximal diameter of the ellipsoid and $n > 1$.

6.1.1 Positioning the ellipsoid in 3D space

The ellipsoid with semiaxes b_i, $i = 1, 3$ is a set of points $\mathbf{X}$, that satisfy the condition:

$$(\mathbf{X} - \mathbf{X}_0)^T \mathbf{Q} (\mathbf{X} - \mathbf{X}_0) \leq 1, \tag{6.1}$$

where $\mathbf{X}_0$ is vector of ellipsoid center, $\mathbf{Q} \succ 0$ is positively defined matrix.

Any $\mathbf{Q}$ can be converted to diagonal matrix $\mathbf{A}$ as follows:

$$\mathbf{Q} = \mathbf{R}^T(\phi, \theta, \Phi) \mathbf{A} \mathbf{R}(\phi, \theta, \Phi). \tag{6.2}$$

Here $\mathbf{A}$ is the diagonal matrix with elements a_{ii} and $\mathbf{R}(\phi, \theta, \Phi)$ is the Euler's rotation matrix. The rotation matrix can be generally evaluated as a series of

rotations:

$$\mathbf{R}(\phi,\theta,\Phi) = \mathbf{R}_z(\phi)\mathbf{R}_x(\theta)\mathbf{R}_{z'}(\Phi) = \\ = \begin{bmatrix} cos\phi & sin\phi & 0 \\ -sin\phi & cos\phi & 0 \\ 0 & 0 & 1 \end{bmatrix} \cdot \begin{bmatrix} 1 & 0 & 0 \\ 0 & cos\theta & sin\theta \\ 0 & -sin\theta & cos\theta \end{bmatrix} \cdot \begin{bmatrix} cos\Phi & sin\Phi & 0 \\ -sin\Phi & cos\Phi & 0 \\ 0 & 0 & 1 \end{bmatrix}. \tag{6.3}$$

Let b_i be the semiaxes of the ellipsoid then, elements of A may be computed as $a_{ii} = 1/b_i^2$. If $b_1 = b_2$ (for the ellipsoid of revolution), the rotation $\mathbf{R}_{z'}(\Phi)$ turns to unitary. So, the total number of the coordinates is 5: $\mathbf{K} = (\mathbf{X}_0, \phi, \theta)$. Using the described method, we can easily construct the ellipsoid of revolution with known orientation and position as a combination of the diagonal matrix **A** and 5-component vector **K**.

6.1.2 Distance between ellipsoids

Minimal distance ΔD_{min} between two ellipsoids $(\mathbf{A}, \mathbf{K})$ and $(\mathbf{A}', \mathbf{K}')$, is a solution of the minimisation problem:

$$\Delta D_{min} = min|\mathbf{X} - \mathbf{Y}|, \mathbf{X} \in S, \mathbf{Y} \in S', \tag{6.4}$$

where S and S' are the surfaces of ellipsoids. The equation (6.4) cannot be solved analyticaly, but there is a variety of numerical methods. All methods may be divided into geometrical [155, 156] and algebraical [157, 158].

Here we will use the geometrical approach developed by Lin and Han [156]. The idea of the method is to construct two balls completely inside each ellipsoid (see figure 6.1).

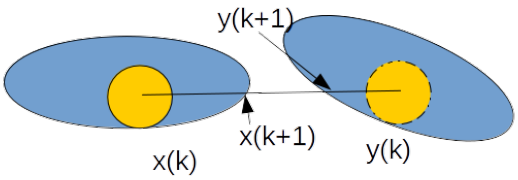

Figure 6.1: Illustration of the approach by Linn.

Then we check whether the line segment [c_1, c_2] between the two centers is entirely contained in $(\mathbf{A}, \mathbf{K}) \cup (\mathbf{A}', \mathbf{K}')$. If it is, then the two ellipsoids have a

nonempty intersection and the distance $\Delta D_{min} = 0$; otherwise, we continue and compute new point $\mathbf{X}(k+1)$ as the intersection of the line segment [$\mathbf{c}_1$, $\mathbf{c}_2$] with the boundary S, and also $\mathbf{Y}(k+1)$ as the intersection of [$\mathbf{c}_1$, $\mathbf{c}_2$] with the boundary S'. As the accuracy criteria the angles between segments $\angle([\mathbf{c}_1, \mathbf{c}_2], [c_1, \mathbf{X}(k)])$ and $\angle([\mathbf{c}_1, \mathbf{c}_2], [\mathbf{c}_2, \mathbf{Y}(k)])$ can be used.

6.1.3 Composite generation procedure

The procedure of the composite creation is follows. On *i*-th step, we generate random **K** as:

$$\begin{cases} \mathbf{X} : x_i \in (0, UC), \\ \phi \in (0, 2\pi), \\ \theta \in (0, \pi). \end{cases} \tag{6.5}$$

Next, two conditions should be satisfied:

i *i*-th the ellipsoid should not intersect the walls of the unit cell.

ii *i*-th ellipsoid should not penetrate into any ellipsoid of the already existing system of $i-1$.

For the real nanocarbon composite, the condition (ii) is more strict. Taking into account the Van der Waals separation, the minimal separation between two ellipsoids here is set as 0.34 nm. If both conditions are satisfied then we store *i*-th ellipsoid, if not—we abandon it and make a new attempt for *i*-th. The example of the distributed ellipsoids with different aspect ratios is presented in figure 6.2.

6.1.4 Percolation computation

Once the distribution of ellipsoids is computed, well-known Dijkstra's algorithm [159] was applied for the calculation of the percolation path. The tunnelling distance of 2 nm was used as a connection criterion.

Next, for the Dijkstra protocol, we have to select an initial and final point (edge) of the graph. Obviously, these points are the ellipsoids located near the *i*-th border of the unit cell and the border opposite to *i*-th correspondingly. Periodic boundary conditions are utilised. So the distance between the ellipsoid

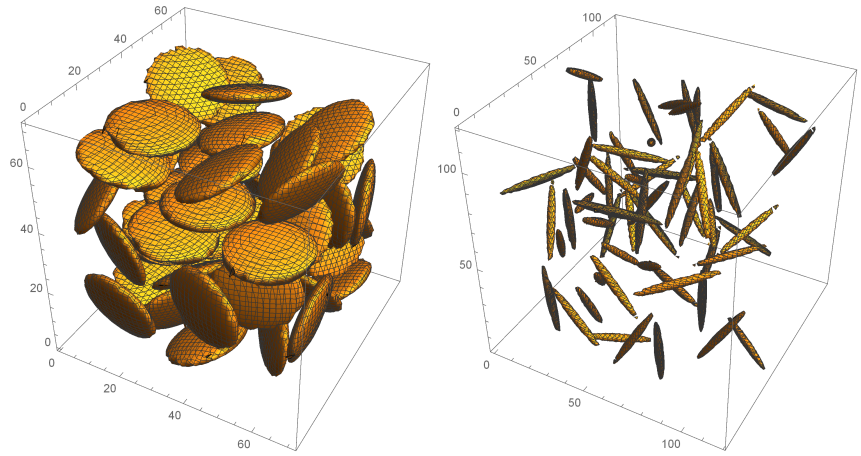

Figure 6.2: Visualisation of the unit cell filled with different aspect ratio ellipsoids (2D inclusions vs 1D).

near the *i*-th border, and the opposite one shifted along the chosen direction on UC, should be less than the predefined separation of 2 nm. If this condition is satisfied, the ellipsoids are considered as the initial and final edges of the graph.

Finally, the boolean vector of the percolation is computed. We consider the system as percolated one if it is percolated in at least one direction.

6.1.5 Total algorithm

The total algorithm organized as Tabu search method [160, 161, 162] and performs as follows:

1. We generate of the composite of $N(p)$ ellipsoids, where p is the volume fraction. A result of this step is an array of the dimensions $5 \times N(p)$ of ellipsoid coordinates **K**.

2. Next, we check if the system is percolated.

If it is, we then terminate, if not, we go back to (1) with $p := p + \delta p$ and construct new composite. The implementation of the algorithm is written with Fortran (see figure 6.3).

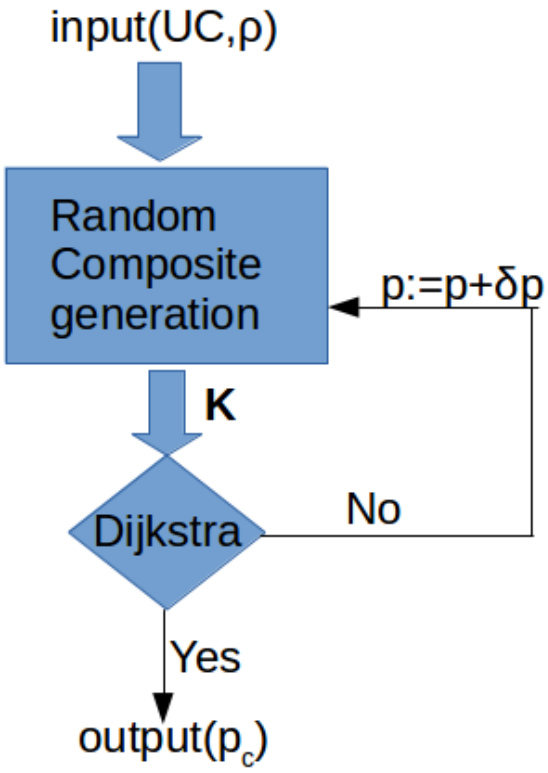

Figure 6.3: Block scheme for the algorithm.

6.2 Percolation modelling results

6.2.1 Two phase system

For the ellipsoid of revolution $b_1 = b_2$, then the aspect ratio can be introduced as $\rho = b_1/b_3$, $\rho \geq 1$. We consider $b_3 = 2.38\ nm$, so the total thickness corresponds to 14 graphite interlayer distances. The formation of the percolation paths depends on the concentration of the filler, and also the distribution of the inclusions. The distribution effect was studied for the system filled with ellipsoids of $\rho = 5$. We made 10,000 observations for n = 3, 7000 for n = 4 and 3000 for n = 5. The percolation probability function is presented in figure 6.4.

The empiric probability functions are governed by the Weibull probability function, $W(\lambda, k) = 1 - e^{-(x/\lambda)^k}$ [163]. The parameters of equation are follows: λ = 0.115, k = 8.797 for n = 3; λ = 0.113, k = 12.092 for n = 4, and λ = 0.113, k = 14.90 for n = 5. The Weibull function describes "time-to-failure" and it is typical for percolation processes [164, 165, 166]. All the probability functions for different

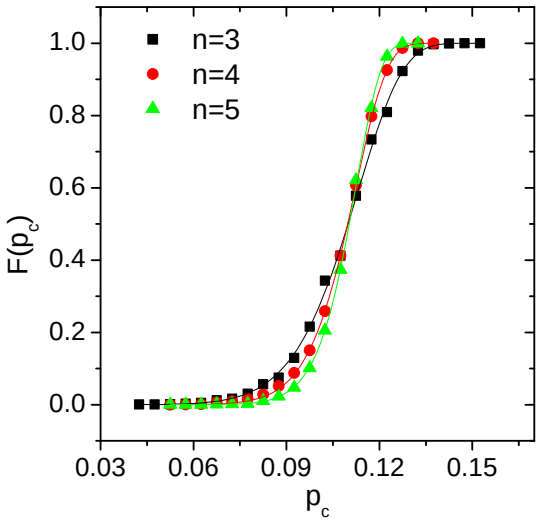

Figure 6.4: The empiric percolation probability function for $\rho = 5$ ellipsoids inside cells of different sizes (symbols); Weibull probability distribution functions (solid curves).

cell size are closely collapsed, but the diffusion is slightly decreased from n = 3 to n = 5, that corresponds to the rise of the Weibull modulus k. This means that the percolation threshold is independent of the UC. The diffusion difference may be explained by the finite volume fraction of the single ellipsoid inside the unit cell. On the other hand, the calculation time increases drastically with UC rise, so the UC size of n = 3 is optimal for the calculation of the composites with ellipsoids of higher aspect ratio.

Figure 6.5 shows the dependence of the percolation threshold on the ellipsoids aspect ratio. As expected, the percolation threshold decreases with the aspect ratio rise. The resulting dependence is in good agreement with experimental data [167, 168, 169] and theoretical modeling [170, 148].

6.2.2 Three phase system (hybrid)

The calculation of the percolation of hybrid composite requires the modification of composite generation procedure section 6.1.3. The generation is organised "one in time". We introduce the parameter $prob$ – the probability of the GNP appearance, then 1-$prob$ is the probability of the CNT appearance. So, upon the generation procedure, each i-th particle has the probability to be "born" as GNP

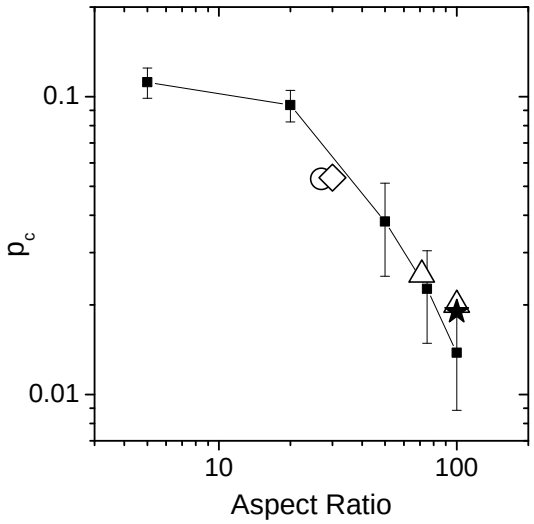

Figure 6.5: Dependence of the percolation concentration on the aspect ratio of the ellipsoid (b_3 = 2.38 and n = 3). Experimentally observed percolation concentrations: △—[167]; ◯—[168] ; ◊—[169], ★ — FMG / PU composites, described in the chapter 4

or CNT. After, the percolation was computed using the standard protocol. For the hybrid composite, we consider p_c as a total volume fraction of the inclusions required for the percolation. Obviously, for the hybrids total concentration may be presented as a sum of partial concentrations as $p_c^{tot} = p_c^{GNP} + p_c^{CNT}$. The dependence of the $p_c^{tot}(prob)$ is presented on figure 6.6. For the case of prob = 1 and 0, the data was verified with the model for 1 type of inclusions. For the calculations two types of ellipsoids were used: $b_1^1 = b_2^1 = 20\ nm$, $b_3^1 = 2\ nm$, and $b_1^2 = b_2^2 = 2\ nm$, $b_3^2 = 20\ nm$.

The excluded volume theory states that the percolation for the hybrid composites [18] occurs if the following condition is satisfied:

$$EVT = \frac{p_c^{GNP}}{p_c^{tot}(1)} + \frac{p_c^{CNT}}{p_c^{tot}(0)} = 1, \tag{6.6}$$

where p_c^{GNP} and p_c^{CNT} are partial concentrations of the GNP and CNT in hybrid composite, and $p_c^{tot}(1)$ and $p_c^{tot}(1)$ are the critical concentrations for composites with GNP ($prob = 1$) and CNT ($prob$ = 0). However, a lot of experimental works evident the percolation even if the condition equation (6.6) is not satisfied [171, 172, 173, 17]. In our case, the exact number of GNP and CNT is known for

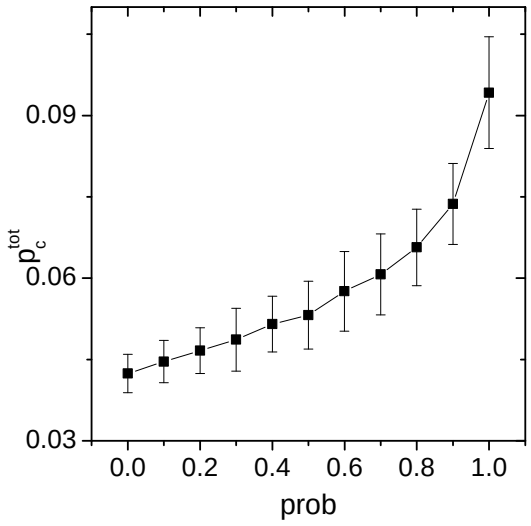

Figure 6.6: Dependence of the percolation concentration for hybrid composites of different composition.

each configuration, so we can easily calculate the EVT-parameter. The result is presented in figure 6.7. As it is seen from figure 6.7, the mean value of EVT is below 1 for all studied configurations. The dependence demonstrates minimum at $prob$ = 0.7–0.8. We can preliminarily conclude that there is some optimum combination of CNT and GNP in hybrid composites.

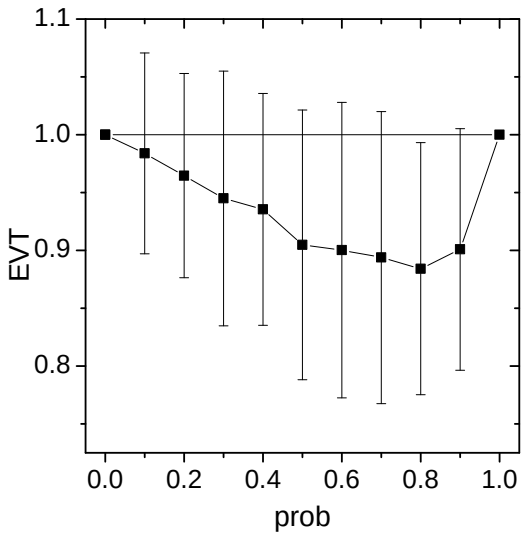

Figure 6.7: Dependence of the left part of equation (6.6) for percolated hybrid composites of different composition.

6.3 Summary

We present a Monte Carlo model for the calculation of the percolation threshold in the irregular system filled with ellipsoids of revolution of different aspect ratios, as well as the hybrid systems. We demonstrate, that the percolation concentration is independent of the unit cell size. The dependence of the percolation concentration on the aspect ratio of nanoinclusions is in the good agreement with previously reported [148, 153, 154, 170].

The reported model can be applied for nanocarbon containing composites as it supports the real experimental situation when percolated additives do not penetrate to each other. The important advantage of the present model is that it can be easily applied for the modelling of multi-component composites, e.g. containing graphene nanoplatelets, carbon black and carbon nanotubes, by means of utilising the ellipsoids of different aspect ratio with the filling fraction corresponding to concentrations of each type of inclusion.

This tested in simple case of one-component composite MC model could be used in a pre-experimental step for producing effective close-to percolation and percolated nanocomposites for various mechanical, thermal and electromagnetic applications to avoid time- and resources consuming "sort-out" experimental

phase, that should lead to design of optimal composition of many functional components providing e.g. the lowest overall percolative concentration at lowest content of most expensive functional additive, keeping at the same time high performance and functionality. The case of hybrid CNT+GNP composite proves the strong synergetic effect.

Summary and conclusions

This thesis is focused on the experimental and numerical investigations of the composite materials filled with 2D nanostructured carbonaceous materials (GNP and FMG) in different matrices with or without additional inclusions (TGS and CNT). The results are obtained by means of the dielecrtric and acoustic spectroscopy and the numerical study using the Tabu search method. The main results are organised into three chapters.

The first chapter delivers the results of the experimental investigations of two different composite systems filled with 2D carbon. Huge rise of the conductivity was observed after first annealing for both of studied composite types. Also the annealing pulls the percolation concentration down. The mechanism of the particle redistribution was proposed to explain the phenomena. The fact of the observation of the phenomena in two systems proves the universality of the process for 2D nanostructured carbon inclusions introduced into the thermo setting polymers.

The second chapter is devoted to studying electromagnetic properties of the GNP + TGS / epoxy resin ternary system. Strong synergetic effect of the two fillers using was found. The addition of GNP particles leads to increase of the dielectric constant, appearance of the Maxwell-Wagner relaxation, and improvement of the piezoelectric response of the composites. Several mechanisms of the synergetic effect were proposed: the first is the co- influence of the different fillers on the final distribution upon the composites preparation, and the second is creating the internal microfields by means of charge accumulation on the GNP.

Third chapter reports on the numerical model development. The model is aimed to calculate the percolation concentration of the composites filled with different types of carbonaceous materials: GNP, CNT, onion-like carbon as well as the hybrid composites. The models' algorithm is organised as the Tabu search

method based on the Monte Carlo protocol for the particle distribution generation and Dijkstra's protocol for percolation check. The programm was tested for the case of 2D inclusions. Obtained results are in good aggreement with previous theoretical and experimental investigations of such type of materials. One of the main advandage of the presented model is the possibility to apply it for hybrid composites calculation. The case of 1D + 2D hybrid system was studied.

The results of the thesis are published as 5 articles in peer-revieved journals and discussed at 7 international conferences.

The main conclusions of the thesis are following:

1. Electromagnetic properties of epoxy composites containing the small addition of GNP have been studied over eight decades of frequency, from 20 Hz to 2 THz. It was demonstrated that the percolation threshold in such systems is 2.87 $wt.$ %. According to low temperature analysis, the electrical conductivity occurs by a tunneling mechanism.

2. The dielectric properties of FMG/polyurethane resin composites, were presented in a wide temperature (25 – 450 K) and frequency (20 Hz – 1 MHz) range. It was established that the electrical percolation threshold lies between 1 and 2 $vol.$ % of filler.

3. During the first annealing of composite samples with GNP or FMG inclusions close to and above the percolation threshold, a dramatic increase of both permittivity and conductivity was observed. In particular case of GNP / epoxy resin composites the increase is by a factor of 3 and by 4 orders of magnitude, respectively (for the 2 $wt.$ % GNP sample). For FMG / polyurethane composites the conductivity rised by more than 2 orders of magnitude.

4. The conductivity increase upon annealing was studied with the impedance formalism. It was found that Maxwell – Wagner relaxation occurs. Upon heating, the relaxation time RC decreases by several orders of magnitude and remains unchanged on cooling. The analysis points to a redistribution of GNP or FMG clusters during which the average size and, consequently, the separation between the conductive clusters decreases. This leads to a huge rise of conductivity and even pulls the percolation threshold down

(for the GNP / epoxy resin composites). After a second or third annealing, no significant changes of the relaxation time and the conductivity was observed, indicating that the redistribution processes is achieved after the first thermal cycle.

5. Annealing was also demonstrated to be a simple way to improve significantly the shielding ability of GNP-based composites. Indeed, as-produced composite with 4 $wt.$ % GNP provided 86% of EM attenuation across a 2 mm thick sample, while the same sample reached 92% after annealing. The same EMI shielding efficiency of 85% can be achieved with 2 $wt.$ % GNP after annealing.

6. Epoxy resin composites with 30 $wt.$ % inclusions of TGS and up to 1 $wt.$ % inclusions of GNP demonstrate ferroelectric properties. The ferroelectric phase transition in these composites was confirmed by the dielectric anomaly and the appearance of piezoelectric properties in the low temperature phase (below the Curie point).

7. The dielectric properties of thernary GNP + TGS / epoxy resin composites are mainly governed by the Maxwell-Wagner relaxation (below 1 MHz) and the ferroelectric soft mode (above 1 MHz). Although the ferroelectric phase transition temperature in ternary composites is the same as in pure TGS crystals, GNP and TGS particles demonstrate an evident synergy effect in dielectric and piezoelectric properties.

8. The reported Monte Carlo model can be applied for nanocarbon containing composites as it supports the real experimental situation when percolated additives do not penetrate to each other. The important advantage of the present model is that it can be easily applied for the modelling of multi-components composites, e.g. containing graphene nanoplatelets, carbon black and carbon nanotubes, by means of utilising the ellipsoids of different aspect ratio with the filling fraction corresponding to concentrations of each type of inclusion.

Bibliography

[1] M. Narkis, M. Zilberman, and A. Siegmann, "On the" curiousity" of electrically conductive melt processed doped-polyaniline/polymer blends versus carbon-black/polymer compounds," *Polymers for Advanced Technologies*, vol. 8, no. 8, p. 525, 1997.

[2] R. Scarisbrick, "Electrically conducting mixtures," *Journal of Physics D: Applied Physics*, vol. 6, no. 17, p. 2098, 1973.

[3] A. Y. Xiao, Q. K. Tong, A. C. Savoca, and H. Van Oosten, "Conductive ink for through hole application," *IEEE Transactions on Components and Packaging Technologies*, vol. 24, no. 3, pp. 445–449, 2001.

[4] S. De and J. White, *Short fibre-polymer composites*. Elsevier, 1996.

[5] R. Norman, *Conductive Rubbers and Plastics: Their Production, Apllication and Test Methods*. Elsevier, 1970.

[6] L. Flandin, Y. Brechet, and J.-Y. Cavaille, "Electrically conductive polymer nanocomposites as deformation sensors," *Composites Science and Technology*, vol. 61, no. 6, pp. 895–901, 2001.

[7] X. Wang and D. Chung, "Short carbon fiber reinforced epoxy coating as a piezoresistive strain sensor for cement mortar," *Sensors and Actuators A: Physical*, vol. 71, no. 3, pp. 208–212, 1998.

[8] W. Zhang, A. A. Dehghani-Sanij, and R. S. Blackburn, "Carbon based conductive polymer composites," *Journal of materials science*, vol. 42, no. 10, pp. 3408–3418, 2007.

[9] S. Iijima, "Helical microtubules of graphitic carbon," *nature*, vol. 354, no. 6348, p. 56, 1991.

[10] R. F. Gibson, *Principles of composite material mechanics*. CRC press, 2016.

[11] Z. Spitalsky, D. Tasis, K. Papagelis, and C. Galiotis, "Carbon nanotube–polymer composites: chemistry, processing, mechanical and electrical properties," *Progress in polymer science*, vol. 35, no. 3, pp. 357–401, 2010.

[12] S.-Y. Yang, W.-N. Lin, Y.-L. Huang, H.-W. Tien, J.-Y. Wang, C.-C. M. Ma, S.-M. Li, and Y.-S. Wang, "Synergetic effects of graphene platelets and carbon nanotubes on the mechanical and thermal properties of epoxy composites," *Carbon*, vol. 49, no. 3, pp. 793–803, 2011.

[13] S. Chatterjee, F. Nafezarefi, N. Tai, L. Schlagenhauf, F. Nüesch, and B. Chu, "Size and synergy effects of nanofiller hybrids including graphene nanoplatelets and carbon nanotubes in mechanical properties of epoxy composites," *Carbon*, vol. 50, no. 15, pp. 5380–5386, 2012.

[14] H. Im and J. Kim, "Thermal conductivity of a graphene oxide–carbon nanotube hybrid/epoxy composite," *Carbon*, vol. 50, no. 15, pp. 5429–5440, 2012.

[15] J. Sumfleth, X. C. Adroher, and K. Schulte, "Synergistic effects in network formation and electrical properties of hybrid epoxy nanocomposites containing multi-wall carbon nanotubes and carbon black," *Journal of materials science*, vol. 44, no. 12, p. 3241, 2009.

[16] C. Li, E. T. Thostenson, and T.-W. Chou, "Dominant role of tunneling resistance in the electrical conductivity of carbon nanotube–based composites," *Applied Physics Letters*, vol. 91, no. 22, p. 223114, 2007.

[17] U. Szeluga, B. Kumanek, and B. Trzebicka, "Synergy in hybrid polymer/nanocarbon composites. a review," *Composites Part A: Applied Science and Manufacturing*, vol. 73, pp. 204–231, 2015.

[18] Y. Sun, H.-D. Bao, Z.-X. Guo, and J. Yu, "Modeling of the electrical percolation of mixed carbon fillers in polymer-based composites," *Macromolecules*, vol. 42, no. 1, pp. 459–463, 2008.

[19] A. Patsidis, K. Kalaitzidou, D. Anastassopoulos, A. Vradis, and G. Psarras, "Graphite nanoplatelets and/or barium titanate/polymer nanocomposites: fabrication, thermomechanical properties, dielectric response and energy storage," *Journal of the Chinese Advanced Materials Society*, vol. 2, no. 3, pp. 207–221, 2014.

[20] S. Moharana, M. K. Mishra, M. Chopkar, and R. Mahaling, "Dielectric properties of three-phase ps-bifeo3-gnp nanocomposites," *Polymer Bulletin*, vol. 74, no. 9, pp. 3707–3719, 2017.

[21] L. D. Landau, J. Bell, M. Kearsley, L. Pitaevskii, E. Lifshitz, and J. Sykes, *Electrodynamics of continuous media*, vol. 8. elsevier, 2013.

[22] C. Kittel, P. McEuen, and P. McEuen, *Introduction to solid state physics*, vol. 8.

Wiley New York, 1996.

[23] M.-S. Cao, W.-L. Song, Z.-L. Hou, B. Wen, and J. Yuan, "The effects of temperature and frequency on the dielectric properties, electromagnetic interference shielding and microwave-absorption of short carbon fiber/silica composites," *Carbon*, vol. 48, no. 3, pp. 788–796, 2010.

[24] G. Psarras, E. Manolakaki, and G. Tsangaris, "Electrical relaxations in polymeric particulate composites of epoxy resin and metal particles," *Composites Part A: Applied Science and Manufacturing*, vol. 33, no. 3, pp. 375–384, 2002.

[25] S. Havriliak and S. Negami, "A complex plane analysis of α-dispersions in some polymer systems," in *Journal of Polymer Science: Polymer Symposia*, vol. 14, pp. 99–117, Wiley Online Library, 1966.

[26] S. Havriliak and S. Negami, "A complex plane representation of dielectric and mechanical relaxation processes in some polymers," *Polymer*, vol. 8, pp. 161–210, 1967.

[27] K. W. Wagner, "Erklärung der dielektrischen nachwirkungsvorgänge auf grund maxwellscher vorstellungen," *Archiv für Elektrotechnik*, vol. 2, no. 9, pp. 371–387, 1914.

[28] R. Sillars, "The properties of a dielectric containing semiconducting particles of various shapes," *Institution of Electrical Engineers-Proceedings of the Wireless Section of the Institution*, vol. 12, no. 35, pp. 139–155, 1937.

[29] N. G. McCrum, B. E. Read, and G. Williams, "Anelastic and dielectric effects in polymeric solids," 1967.

[30] P. Macedo, C. Moynihan, and R. Bose, "Dielectric modulus: experiment, application, and interpretation," *J Phy Chem Glasses*, vol. 13, p. 171, 1972.

[31] K. Christensen, "Percolation theory," *Imperial College London*, vol. 1, 2002.

[32] K. Ahmad, W. Pan, and S.-L. Shi, "Electrical conductivity and dielectric properties of multiwalled carbon nanotube and alumina composites," *Applied physics letters*, vol. 89, no. 13, p. 133122, 2006.

[33] C.-W. Nan, Y. Shen, and J. Ma, "Physical properties of composites near percolation," *Annual Review of Materials Research*, vol. 40, pp. 131–151, 2010.

[34] A. K. Jonscher, *Universal relaxation law: a sequel to Dielectric relaxation in solids*. Chelsea Dielectrics Press, 1996.

[35] A. K. Jonscher, "The universal dielectric response," *nature*, vol. 267,

no. 5613, p. 673, 1977.

[36] D. Almond, G. Duncan, and A. West, "The determination of hopping rates and carrier concentrations in ionic conductors by a new analysis of ac conductivity," *Solid State Ionics*, vol. 8, no. 2, pp. 159–164, 1983.

[37] A. Jonscher and M. Frost, "Weakly frequency-dependent electrical conductivity in a chalcogenide glass," *Thin Solid Films*, vol. 37, no. 2, pp. 267–273, 1976.

[38] M. B. Smith, K. Page, T. Siegrist, P. L. Redmond, E. C. Walter, R. Seshadri, L. E. Brus, and M. L. Steigerwald, "Crystal structure and the paraelectric-to-ferroelectric phase transition of nanoscale batio3," *Journal of the American Chemical Society*, vol. 130, no. 22, pp. 6955–6963, 2008.

[39] B. Jaffe, *Piezoelectric ceramics*, vol. 3. Elsevier, 2012.

[40] Z. L. Wang and J. Song, "Piezoelectric nanogenerators based on zinc oxide nanowire arrays," *Science*, vol. 312, no. 5771, pp. 242–246, 2006.

[41] K. Ishikawa, K. Yoshikawa, and N. Okada, "Size effect on the ferroelectric phase transition in pbtio 3 ultrafine particles," *Physical Review B*, vol. 37, no. 10, p. 5852, 1988.

[42] R. Grigalaitis, J. Banys, S. Lapinskas, E. Erdem, R. Bottcher, H.-j. Glasel, and E. Hartmann, "Dielectric investigations and theoretical calculations of size effect in lead titanate nanocrystals," *IEEE transactions on ultrasonics, ferroelectrics, and frequency control*, vol. 53, no. 12, 2006.

[43] T. Ramoška, J. Banys, R. Grigalaitis, and A. Kareiva, "Dielectric investigations of nanoferroelectric batio3," *Ferroelectrics*, vol. 368, no. 1, pp. 170–176, 2008.

[44] R. Grigalaitis, M. Ivanov, J. Macutkevic, J. Banys, J. Carreaud, J. M. Kiat, V. V. Laguta, and B. Zalar, "Size effects in a relaxor: further insights into pmn," *Journal of Physics: Condensed Matter*, vol. 26, no. 27, p. 272201, 2014.

[45] J. Grigas, *Microwave dielectric spectroscopy of ferroelectrics and related materials*. Gordon and Breach publishers, 1996.

[46] B.-K. Chung, "Dielectric constant measurement for thin material at microwave frequencies," *Progress In Electromagnetics Research*, vol. 75, pp. 239–252, 2007.

[47] J. D. Jackson, *Classical electrodynamics*. Wiley, 1999.

[48] M. Born and E. Wolf, *Principles of optics: electromagnetic theory of propagation, interference and diffraction of light*. Elsevier, 2013.

[49] E. Nielsen, "Scattering by a cylindrical post of complex permittivity in a waveguide," *IEEE Transactions on Microwave Theory and Techniques*, vol. 17, no. 3, pp. 148–153, 1969.

[50] L.-F. Chen, C. Ong, C. Neo, V. Varadan, and V. K. Varadan, *Microwave electronics: measurement and materials characterization*. John Wiley & Sons, 2004.

[51] A. Pashkin, E. Buixaderas, P. Kužel, M.-H. Liang, C.-T. Hu, and I.-N. Lin, "Thz transmission spectroscopy applied to dielectrics and microwave ceramics," *Ferroelectrics*, vol. 254, no. 1, pp. 113–120, 2001.

[52] L. Duvillaret, F. Garet, and J.-L. Coutaz, "Highly precise determination of optical constants and sample thickness in terahertz time-domain spectroscopy," *Applied optics*, vol. 38, no. 2, pp. 409–415, 1999.

[53] V. Samulionis, J. Banys, and Y. Vysochanskii, "Piezoelectric and elastic properties of layered materials of cu (in, cr) p2 (s, se) 6 system," *Journal of electroceramics*, vol. 22, no. 1-3, pp. 192–197, 2009.

[54] V. Samulionis, J. Banys, and Y. Vysochanskii, "Piezoelectric and ultrasonic studies of mixed agxcu1-xinp2 (s, se) 6 layered crystals," in *Materials Science Forum*, vol. 636, pp. 398–403, Trans Tech Publ, 2010.

[55] F. Qin and C. Brosseau, "A review and analysis of microwave absorption in polymer composites filled with carbonaceous particles," *Journal of applied physics*, vol. 111, no. 6, p. 4, 2012.

[56] J. Liang, Y. Wang, Y. Huang, Y. Ma, Z. Liu, J. Cai, C. Zhang, H. Gao, and Y. Chen, "Electromagnetic interference shielding of graphene/epoxy composites," *Carbon*, vol. 47, no. 3, pp. 922–925, 2009.

[57] B.-P. Adohi, A. Mdarhri, C. Prunier, B. Haidar, and C. Brosseau, "A comparison between physical properties of carbon black-polymer and carbon nanotubes-polymer composites," *Journal of applied physics*, vol. 108, no. 7, p. 074108, 2010.

[58] B. Adohi, V. Laur, B. Haidar, and C. Brosseau, "Measurement of the microwave effective permittivity in tensile-strained polyvinylidene difluoride trifluoroethylene filled with graphene," *Applied Physics Letters*, vol. 104, no. 8, p. 082902, 2014.

[59] B. Adohi, D. Bychanok, B. Haidar, and C. Brosseau, "Microwave and mechanical properties of quartz/graphene-based polymer nanocomposites," *Applied Physics Letters*, vol. 102, no. 7, p. 072903, 2013.

[60] I. C. Finegan and G. G. Tibbetts, "Electrical conductivity of vapor-grown carbon fiber/thermoplastic composites," *Journal of Materials Research*, vol. 16, pp. 1668–1674, 2001.

[61] A. Mdarhri, F. Carmona, C. Brosseau, and P. Delhaes, "Direct current electrical and microwave properties of polymer-multiwalled carbon nanotubes composites," *Journal of Applied Physics*, vol. 103, no. 5, pp. –, 2008.

[62] P. Kuzhir, A. Paddubskaya, D. Bychanok, A. Nemilentsau, M. Shuba, A. Plusch, S. Maksimenko, S. Bellucci, L. Coderoni, F. Micciulla, *et al.*, "Microwave probing of nanocarbon based epoxy resin composite films: Toward electromagnetic shielding," *Thin Solid Films*, vol. 519, no. 12, pp. 4114–4118, 2011.

[63] J. Macutkevič, J. Banys, K. Glemža, V. Kuznetsov, V. Borjanovic, and O. Shenderova, "Dielectric properties of annealed onion-like carbon composites in microwave region," *Lithuanian Journal of Physics*, vol. 53, no. 4, 2013.

[64] A. Efros and B. Shklovskii, "Critical behaviour of conductivity and dielectric constant near the metal-non-metal transition threshold," *physica status solidi (b)*, vol. 76, no. 2, pp. 475–485, 1976.

[65] J. C. M. Garnett, "Colours in metal glasses and in metallic films," *Philosophical Transactions of the Royal Society of London A: Mathematical, Physical and Engineering Sciences*, vol. 203, no. 359-371, pp. 385–420, 1904.

[66] J. M. Garnett, "Colours in metal glasses, in metallic films and in metallic solutions.Ůii," *Proc. R. Soc. Lond. A*, vol. 76, no. 511, pp. 370–373, 1905.

[67] D. S. McLachlan, M. Blaszkiewicz, and R. E. Newnham, "Electrical resistivity of composites," *Journal of the American Ceramic Society*, vol. 73, no. 8, pp. 2187–2203, 1990.

[68] C. Brosseau, "Generalized effective medium theory and dielectric relaxation in particle-filled polymeric resins," *Journal of applied physics*, vol. 91, no. 5, pp. 3197–3204, 2002.

[69] B. De Vivo, P. Lamberti, G. Spinelli, and V. Tucci, "A morphological and structural approach to evaluate the electromagnetic performances of composites based on random networks of carbon nanotubes," *Journal of Applied Physics*, vol. 115, no. 15, p. 154311, 2014.

[70] X. Sun and M. Song, "Numerical simulations of the effect of microstructure on ac conductivity of mwcnt/polymer nanocomposites," *Macromolecular*

Theory and Simulations, vol. 19, no. 1, pp. 57–63, 2010.

[71] F. Nilsson, U. Gedde, and M. Hedenqvist, "Modelling the relative permittivity of anisotropic insulating composites," *Composites Science and Technology*, vol. 71, no. 2, pp. 216 – 221, 2011.

[72] J. W. Evans, "Random and cooperative sequential adsorption," *Reviews of modern physics*, vol. 65, no. 4, p. 1281, 1993.

[73] V. Myroshnychenko and C. Brosseau, "Finite-element method for calculation of the effective permittivity of random inhomogeneous media," *Physical Review E*, vol. 71, no. 1, p. 016701, 2005.

[74] V. Myroshnychenko and C. Brosseau, "Effective complex permittivity of two-phase random composite media: A test of the two exponent phenomenological percolation equation," *Journal of Applied Physics*, vol. 103, no. 8, pp. –, 2008.

[75] V. Myroshnychenko and C. Brosseau, "Possible manifestation of nonuniversality in some continuum percolation systems," *Journal of Physics D: Applied Physics*, vol. 41, no. 9, p. 095401, 2008.

[76] D. Bychanok, P. Kuzhir, S. Maksimenko, S. Bellucci, and C. Brosseau, "Characterizing epoxy composites filled with carbonaceous nanoparticles from dc to microwave," *Journal of Applied Physics*, vol. 113, no. 12, p. 124103, 2013.

[77] C. A. Poland, R. Duffin, I. Kinloch, A. Maynard, W. A. Wallace, A. Seaton, V. Stone, S. Brown, W. MacNee, and K. Donaldson, "Carbon nanotubes introduced into the abdominal cavity of mice show asbestos-like pathogenicity in a pilot study," *Nature nanotechnology*, vol. 3, no. 7, p. 423, 2008.

[78] S.-E. Lee, O. Choi, and H. T. Hahn, "Microwave properties of graphite nanoplatelet/epoxy composites," *Journal of Applied Physics*, vol. 104, no. 3, p. 033705, 2008.

[79] M. S. Sarto, A. G. D'Aloia, A. Tamburrano, and G. De Bellis, "Synthesis, modeling, and experimental characterization of graphite nanoplatelet-based composites for emc applications," *IEEE Transactions on Electromagnetic Compatibility*, vol. 54, no. 1, pp. 17–27, 2012.

[80] S. Stankovich, D. A. Dikin, G. H. Dommett, K. M. Kohlhaas, E. J. Zimney, E. A. Stach, R. D. Piner, S. T. Nguyen, and R. S. Ruoff, "Graphene-based composite materials," *nature*, vol. 442, no. 7100, p. 282, 2006.

[81] S. Stankovich, D. A. Dikin, R. D. Piner, K. A. Kohlhaas, A. Kleinhammes,

Y. Jia, Y. Wu, S. T. Nguyen, and R. S. Ruoff, "Synthesis of graphene-based nanosheets via chemical reduction of exfoliated graphite oxide," *carbon*, vol. 45, no. 7, pp. 1558–1565, 2007.

[82] J. Li, J.-K. Kim, and M. L. Sham, "Conductive graphite nanoplatelet/epoxy nanocomposites: effects of exfoliation and uv/ozone treatment of graphite," *Scripta Materialia*, vol. 53, no. 2, pp. 235–240, 2005.

[83] L. Guadagno, M. Raimondo, L. Vertuccio, M. Mauro, G. Guerra, K. Lafdi, B. De Vivo, P. Lamberti, G. Spinelli, and V. Tucci, "Optimization of graphene-based materials outperforming host epoxy matrices," *RSC Advances*, vol. 5, no. 46, pp. 36969–36978, 2015.

[84] A. Yu, P. Ramesh, M. E. Itkis, E. Bekyarova, and R. C. Haddon, "Graphite nanoplatelet-epoxy composite thermal interface materials," *The Journal of Physical Chemistry C*, vol. 111, no. 21, pp. 7565–7569, 2007.

[85] M.-T. Hung, O. Choi, Y. S. Ju, and H. Hahn, "Heat conduction in graphite-nanoplatelet-reinforced polymer nanocomposites," *Applied Physics Letters*, vol. 89, no. 2, p. 023117, 2006.

[86] J.-K. Kim, C. Hu, R. S. Woo, and M.-L. Sham, "Moisture barrier characteristics of organoclay–epoxy nanocomposites," *Composites Science and Technology*, vol. 65, no. 5, pp. 805–813, 2005.

[87] D. Van der Putten, J. Moonen, H. Brom, J. Brokken-Zijp, and M. Michels, "Evidence for superlocalization on a fractal network in conductive carbon-black–polymer composites," *Physical review letters*, vol. 69, no. 3, p. 494, 1992.

[88] C. Brosseau, P. Molinié, F. Boulic, and F. Carmona, "Mesostructure, electron paramagnetic resonance, and magnetic properties of polymer carbon black composites," *Journal of Applied Physics*, vol. 89, no. 12, pp. 8297–8310, 2001.

[89] A. Pyushch, J. Macutkevic, J. Banys, D. Bychanok, S. Maksimenko, A. Cataldo, F. Micciulla, and S. Bellucci, "Electromagnetic properties of graphene nano platelets / epoxy composites in whide temperature range," in *Proceedings of International Conference Nanomeeting-2015, 26-29 May 2015*, pp. 233–235, World Scientific, 2015.

[90] K.-M. Jäger, D. McQueen, and J. Vilcakova, "Ac conductance and capacitance of carbon black polymer composites during thermal cycling and isothermal annealing," *Journal of Physics D: Applied Physics*, vol. 35, no. 10,

p. 1068, 2002.

[91] P. Mather and K. Thomas, "Carbon black/high density polyethylene conducting composite materials: Part i structural modification of a carbon black by gasification in carbon dioxide and the effect on the electrical and mechanical properties of the composite," *Journal of materials science*, vol. 32, no. 2, pp. 401–407, 1997.

[92] S. Barrau, P. Demont, A. Peigney, C. Laurent, and C. Lacabanne, "Dc and ac conductivity of carbon nanotubes-polyepoxy composites," *Macromolecules*, vol. 36, no. 14, pp. 5187–5194, 2003.

[93] J. Macutkevic, P. Kuzhir, A. Paddubskaya, S. Maksimenko, J. Banys, A. Celzard, V. Fierro, S. Bistarelli, A. Cataldo, F. Micciulla, *et al.*, "Electrical transport in carbon black-epoxy resin composites at different temperatures," *Journal of Applied Physics*, vol. 114, no. 3, p. 033707, 2013.

[94] J. Macutkevic, P. P. Kuzhir, A. G. Paddubskaya, J. Banys, S. A. Maksimenko, E. Stefanutti, F. Micciulla, and S. Bellucci, "Broadband dielectric/electric properties of epoxy thin films filled with multiwalled carbon nanotubes," *Journal of Nanophotonics*, vol. 7, no. 1, p. 073593, 2013.

[95] X. He, J. Du, Z. Ying, and H. Cheng, "Positive temperature coefficient effect in multiwalled carbon nanotube/high-density polyethylene composites," *Applied Physics Letters*, vol. 86, no. 6, p. 062112, 2005.

[96] J.-F. Gao, D.-X. Yan, B. Yuan, H.-D. Huang, and Z.-M. Li, "Large-scale fabrication and electrical properties of an anisotropic conductive polymer composite utilizing preferable location of carbon nanotubes in a polymer blend," *Composites Science and Technology*, vol. 70, no. 13, pp. 1973–1979, 2010.

[97] N. Jović, D. Dudić, A. Montone, M. V. Antisari, M. Mitrić, and V. Djoković, "Temperature dependence of the electrical conductivity of epoxy/expanded graphite nanosheet composites," *Scripta Materialia*, vol. 58, no. 10, pp. 846–849, 2008.

[98] G. Furdin, J. Marêché, and A. Herold, "Graphite micronique plat, procede pour sa preparation et ses applications," 1993.

[99] A. Celzard, G. Furdin, J. Mareche, E. McRae, M. Dufort, and C. Deleuze, "Anisotropic percolation in an epoxy-graphite disc composite," *Solid state communications*, vol. 92, no. 5, pp. 377–383, 1994.

[100] A. Celzard, G. Furdin, J. Mareche, and E. McRae, "Non-linear current-

voltage characteristics in anisotropic epoxy resin-graphite flake composites," *Journal of materials science*, vol. 32, no. 7, pp. 1849–1853, 1997.

[101] A. Dabrowska, S. Bellucci, A. Cataldo, F. Micciulla, and A. Huczko, "Nanocomposites of epoxy resin with graphene nanoplates and exfoliated graphite: Synthesis and electrical properties," *physica status solidi (b)*, vol. 251, no. 12, pp. 2599–2602, 2014.

[102] S. Bellucci, M. Bozzi, A. Cataldo, R. Moro, D. Mencarelli, and L. Pierantoni, "Graphene as a tunable resistor," in *Semiconductor Conference (CAS), 2014 International*, pp. 17–20, IEEE, 2014.

[103] L. Pierantoni, M. Bozzi, R. Moro, D. Mencarelli, and S. Bellucci, "On the use of electrostatically doped graphene: Analysis of microwave attenuators," in *Numerical Electromagnetic Modeling and Optimization for RF, Microwave, and Terahertz Applications (NEMO), 2014 International Conference on*, pp. 1–4, IEEE, 2014.

[104] L. Pierantoni, D. Mencarelli, M. Bozzi, R. Moro, and S. Bellucci, "Graphene-based electronically tuneable microstrip attenuator," *Nanomaterials and Nanotechnology*, vol. 4, p. 18, 2014.

[105] L. Pierantoni, D. Mencarelli, M. Bozzi, R. Moro, S. Moscato, L. Perregrini, F. Micciulla, A. Cataldo, and S. Bellucci, "Broadband microwave attenuator based on few layer graphene flakes," *IEEE Transactions on Microwave Theory and Techniques*, vol. 63, no. 8, pp. 2491–2497, 2015.

[106] C.-W. Nan, "Physics of inhomogeneous inorganic materials," *Progress in materials science*, vol. 37, no. 1, pp. 1–116, 1993.

[107] M. Panda, V. Srinivas, and A. Thakur, "On the question of percolation threshold in polyvinylidene fluoride/nanocrystalline nickel composites," *Applied Physics Letters*, vol. 92, no. 13, p. 132905, 2008.

[108] Z.-M. Dang, Y.-H. Lin, and C.-W. Nan, "Novel ferroelectric polymer composites with high dielectric constants," *Advanced Materials*, vol. 15, no. 19, pp. 1625–1629, 2003.

[109] J. Macutkevic, J. Banys, and A. Matulis, "Determination of the distribution of the relaxation times from dielectric spectra," *Nonlinear Anal. Model. Control*, vol. 9, no. 1, pp. 75–88, 2004.

[110] S. Torquato, "Nearest-neighbor statistics for packings of hard spheres and disks," *Physical Review E*, vol. 51, no. 4, p. 3170, 1995.

[111] P. Sheng, E. Sichel, and J. I. Gittleman, "Fluctuation-induced tunneling con-

duction in carbon-polyvinylchloride composites," *Physical Review Letters*, vol. 40, no. 18, p. 1197, 1978.

[112] Z.-M. Dang, L. Wang, Y. Yin, Q. Zhang, and Q.-Q. Lei, "Giant dielectric permittivities in functionalized carbon-nanotube/electroactive-polymer nanocomposites," *Advanced Materials*, vol. 19, no. 6, pp. 852–857, 2007.

[113] J. Liu, C.-G. Duan, W.-G. Yin, W.-N. Mei, R. W. Smith, and J. R. Hardy, "Large dielectric constant and maxwell-wagner relaxation in bi 2/ 3 cu 3 ti 4 o 12," *Physical review B*, vol. 70, no. 14, p. 144106, 2004.

[114] H. Banno, "Theoretical equations for dielectric and piezoelectric properties of ferroelectric composites based on modified cubes model," *Japanese Journal of Applied Physics*, vol. 24, no. S2, p. 445, 1985.

[115] Y. Bai, Z.-Y. Cheng, V. Bharti, H. Xu, and Q. Zhang, "High-dielectric-constant ceramic-powder polymer composites," *Applied Physics Letters*, vol. 76, no. 25, pp. 3804–3806, 2000.

[116] M. T. Sebastian and H. Jantunen, "Polymer–ceramic composites of 0–3 connectivity for circuits in electronics: a review," *International Journal of Applied Ceramic Technology*, vol. 7, no. 4, pp. 415–434, 2010.

[117] C. Brosseau, P. Quéffélec, and P. Talbot, "Microwave characterization of filled polymers," *Journal of Applied Physics*, vol. 89, no. 8, pp. 4532–4540, 2001.

[118] R. Popielarz, C. Chiang, R. Nozaki, and J. Obrzut, "Dielectric properties of polymer/ferroelectric ceramic composites from 100 hz to 10 ghz," *Macromolecules*, vol. 34, no. 17, pp. 5910–5915, 2001.

[119] S. K. Bhattacharya and R. R. Tummala, "Next generation integral passives: materials, processes, and integration of resistors and capacitors on pwb substrates," *Journal of Materials Science: Materials in Electronics*, vol. 11, no. 3, pp. 253–268, 2000.

[120] Q. Wang and L. Zhu, "Polymer nanocomposites for electrical energy storage," *Journal of Polymer Science Part B: Polymer Physics*, vol. 49, no. 20, pp. 1421–1429, 2011.

[121] X. Chen, G. Wang, Y. Duan, and S. Liu, "Microwave absorption properties of barium titanate/epoxide resin composites," *Journal of Physics D: Applied Physics*, vol. 40, no. 6, p. 1827, 2007.

[122] E. Ruiz-Hitzky, M. M. C. Sobral, A. Gómez-Avilés, C. Nunes, C. Ruiz-García, P. Ferreira, and P. Aranda, "Clay-graphene nanoplatelets func-

tional conducting composites," *Advanced Functional Materials*, vol. 26, no. 41, pp. 7394–7405, 2016.

[123] H.-D. Bao, Z.-X. Guo, and J. Yu, "Effect of electrically inert particulate filler on electrical resistivity of polymer/multi-walled carbon nanotube composites," *Polymer*, vol. 49, no. 17, pp. 3826–3831, 2008.

[124] Y.-F. Lan and J.-J. Lin, "Observation of carbon nanotube and clay micelle-like microstructures with dual dispersion property," *The Journal of Physical Chemistry A*, vol. 113, no. 30, pp. 8654–8659, 2009.

[125] D. Pedrazzoli, A. Pegoretti, and K. Kalaitzidou, "Synergistic effect of exfoliated graphite nanoplatelets and short glass fiber on the mechanical and interfacial properties of epoxy composites," *Composites Science and Technology*, vol. 98, pp. 15–21, 2014.

[126] B. De Vivo, P. Lamberti, G. Spinelli, V. Tucci, L. Guadagno, M. Raimondo, L. Vertuccio, and V. Vittoria, "Improvement of the electrical conductivity in multiphase epoxy-based mwcnt nanocomposites by means of an optimized clay content," *Composites Science and Technology*, vol. 89, pp. 69–76, 2013.

[127] Z.-M. Dang, S.-H. Yao, J.-K. Yuan, and J. Bai, "Tailored dielectric properties based on microstructure change in batio3-carbon nanotube/polyvinylidene fluoride three-phase nanocomposites," *The Journal of Physical Chemistry C*, vol. 114, no. 31, pp. 13204–13209, 2010.

[128] K. Piasotski, D. Bychanok, G. Gorokhov, D. Meisak, A. Plyushch, P. Kuzhir, A. Sokol, K. Lapko, A. Sánchez-Sánchez, V. Fierro, *et al.*, "Microwave-absorbing properties of phosphate ceramics filled with carbon nanotubes, batio3 and fe3o4," in *Physics, Chemistry And Application Of Nanostructures: Reviews And Short Notes To Nanomeeting-2017*, pp. 202–205, World Scientific, 2017.

[129] B. Luo, X. Wang, E. Tian, H. Gong, Q. Zhao, Z. Shen, Y. Xu, X. Xiao, and L. Li, "Dielectric enhancement in graphene/barium titanate nanocomposites," *ACS applied materials & interfaces*, vol. 8, no. 5, pp. 3340–3348, 2016.

[130] R. Hill and S. Ichiki, "Polarization relaxation in triglycine sulfate above the curie temperature," *Physical Review*, vol. 128, no. 3, p. 1140, 1962.

[131] R. Blinc, S. Detoni, and M. Pintar, "Nature of the ferroelectric transition in triglycine sulfate," *Physical Review*, vol. 124, no. 4, p. 1036, 1961.

[132] M. Amin, K. Darwish, and S. Ibrahim, "Pyroelectricity and electrical conductivity in polycrystalline triglycine sulfate (tgs)," *Ferroelectrics*, vol. 76, no. 1, pp. 33–41, 1987.

[133] V. Khutorsky and S. B. Lang, "Very strong influence of moisture on pyroelectric and dielectric properties of triglycine sulfate-gelatin films," *Journal of applied physics*, vol. 82, no. 3, pp. 1288–1292, 1997.

[134] V. Khutorsky and S. Lang, "Pyroelectric and dielectric properties of dry and moist tgs-gelatin films," in *Applications of Ferroelectrics, 1994. ISAF'94., Proceedings of the Ninth IEEE International Symposium on*, pp. 817–820, IEEE, 1991.

[135] N. T. Shanthi, P. Selvarajan, and C. Mahadevan, "Growth, structural, mechanical, spectral and dielectric characterization of nacl-added triglycine sulfate single crystals," *Current Applied Physics*, vol. 9, no. 5, pp. 1155–1159, 2009.

[136] A. Celzard, E. McRae, J. Mareche, G. Furdin, M. Dufort, and C. Deleuze, "Composites based on micron-sized exfoliated graphite particles: electrical conduction, critical exponents and anisotropy," *Journal of Physics and Chemistry of Solids*, vol. 57, no. 6-8, pp. 715–718, 1996.

[137] N. Jayasundere and B. Smith, "Dielectric constant for binary piezoelectric 0-3 composites," *Journal of Applied Physics*, vol. 73, no. 5, pp. 2462–2466, 1993.

[138] A. Celzard, E. McRae, C. Deleuze, M. Dufort, G. Furdin, and J. Marêché, "Critical concentration in percolating systems containing a high-aspect-ratio filler," *Physical Review B*, vol. 53, no. 10, p. 6209, 1996.

[139] J. Scott, "Soft-mode spectroscopy: Experimental studies of structural phase transitions," *Reviews of Modern Physics*, vol. 46, no. 1, p. 83, 1974.

[140] A. Plyushch, J. Macutkevic, P. Kuzhir, J. Banys, D. Bychanok, P. Lambin, S. Bistarelli, A. Cataldo, F. Micciulla, and S. Bellucci, "Electromagnetic properties of graphene nanoplatelets/epoxy composites," *Composites Science and Technology*, vol. 128, pp. 75–83, 2016.

[141] V. Samulionis, J. Banys, and Y. Vysochanskii, "The characterization of two dimensional electrostrictive cuinp2s6 materials for transducers," in *Materials science forum*, vol. 514, pp. 230–234, Trans Tech Publ, 2006.

[142] V. Samulionis, J. Banys, and Y. Vysochanskii, "Ultrasonic and piezoelectric studies of phase transitions in two-dimensional cuinp2s6 type crystals,"

Ferroelectrics, vol. 379, no. 1, pp. 69–76, 2009.

[143] G. Grimmett, "What is percolation?," in *Percolation*, pp. 1–31, Springer, 1999.

[144] D. Stauffer and A. Aharony, *Introduction to percolation theory*. CRC press, 1994.

[145] I. Balberg, N. Binenbaum, and N. Wagner, "Percolation thresholds in the three-dimensional sticks system," *Physical Review Letters*, vol. 52, no. 17, p. 1465, 1984.

[146] A. Bug, S. Safran, and I. Webman, "Continuum percolation of rods," *Physical review letters*, vol. 54, no. 13, p. 1412, 1985.

[147] B. De Vivo, P. Lamberti, G. Spinelli, and V. Tucci, "Numerical investigation on the influence factors of the electrical properties of carbon nanotubes-filled composites," *Journal of Applied Physics*, vol. 113, no. 24, p. 244301, 2013.

[148] E. Garboczi, K. Snyder, J. Douglas, and M. Thorpe, "Geometrical percolation threshold of overlapping ellipsoids," *Physical review E*, vol. 52, no. 1, p. 819, 1995.

[149] Y.-B. Yi and A. Sastry, "Analytical approximation of the two-dimensional percolation threshold for fields of overlapping ellipses," *Physical Review E*, vol. 66, no. 6, p. 066130, 2002.

[150] Y.-B. Yi, C.-W. Wang, and A. Sastry, "Two-dimensional vs. three-dimensional clustering and percolation in fields of overlapping ellipsoids," *Journal of the Electrochemical Society*, vol. 151, no. 8, pp. A1292–A1300, 2004.

[151] S. Feng, B. Halperin, and P. Sen, "Transport properties of continuum systems near the percolation threshold," *Physical Review B*, vol. 35, no. 1, p. 197, 1987.

[152] R. Fujie and T. Odagaki, "Effects of superspreaders in spread of epidemic," *Physica A: Statistical Mechanics and its Applications*, vol. 374, no. 2, pp. 843–852, 2007.

[153] I. Y. Sagalianov, O. A. Lazarenko, L. L. Vovchenko, and L. Y. Matzui, "Monte-carlo study of the percolation in a binary composites: Hardcore and softcore models comparison," in *Nanomaterials: Application & Properties (NAP), 2017 IEEE 7th International Conference*, pp. 03NNSA30–1, IEEE, 2017.

[154] S. Akagawa and T. Odagaki, "Geometrical percolation of hard-core el-

lipsoids of revolution in the continuum," *Physical Review E*, vol. 76, no. 5, p. 051402, 2007.

[155] A. Kosolap, "Quadratic optimization problems of computer geometry," *Art. Int.*, no. 1, pp. 70–75, 2009.

[156] A. Lin and S.-P. Han, "On the distance between two ellipsoids," *SIAM Journal on Optimization*, vol. 13, no. 1, pp. 298–308, 2002.

[157] G. S. Tamasyan and A. A. Chumakov, "Finding the distance between ellipsoids," *Journal of Applied and Industrial Mathematics*, vol. 8, no. 3, pp. 400–410, 2014.

[158] A. Y. Uteshev and M. Yashina, "Computation of the distance from an ellipsoid to a linear surface and a quadric in rn," in *Doklady Mathematics*, vol. 77, pp. 269–272, Springer, 2008.

[159] E. W. Dijkstra, "A note on two problems in connexion with graphs," *Numerische mathematik*, vol. 1, no. 1, pp. 269–271, 1959.

[160] F. Glover, "Tabu searchŮpart i," *ORSA Journal on computing*, vol. 1, no. 3, pp. 190–206, 1989.

[161] F. Glover, "Tabu searchŮpart ii," *ORSA Journal on computing*, vol. 2, no. 1, pp. 4–32, 1990.

[162] F. Glover and M. Laguna, "Tabu search," in *Handbook of combinatorial optimization*, pp. 3261–3362, Springer, 2013.

[163] W. Weibull *et al.*, "A statistical distribution function of wide applicability," *Journal of applied mechanics*, vol. 18, no. 3, pp. 293–297, 1951.

[164] J. Stathis, "Percolation models for gate oxide breakdown," *Journal of applied physics*, vol. 86, no. 10, pp. 5757–5766, 1999.

[165] T. Kauerauf, R. Degraeve, E. Cartier, C. Soens, and G. Groeseneken, "Low weibull slope of breakdown distributions in high-k layers," *IEEE Electron Device Letters*, vol. 23, no. 4, pp. 215–217, 2002.

[166] S. Long, X. Lian, C. Cagli, L. Perniola, E. Miranda, M. Liu, and J. Suñé, "A model for the set statistics of rram inspired in the percolation model of oxide breakdown," *IEEE Electron Device Letters*, vol. 34, no. 8, pp. 999–1001, 2013.

[167] B. Li and W.-H. Zhong, "Review on polymer/graphite nanoplatelet nanocomposites," *Journal of materials science*, vol. 46, no. 17, pp. 5595–5614, 2011.

[168] S. Araby, Q. Meng, L. Zhang, H. Kang, P. Majewski, Y. Tang, and J. Ma,

"Electrically and thermally conductive elastomer/graphene nanocomposites by solution mixing," *Polymer*, vol. 55, no. 1, pp. 201–210, 2014.

[169] J.-W. Shen, W.-Y. Huang, S.-W. Zuo, and J. Hou, "Polyethylene/grafted polyethylene/graphite nanocomposites: Preparation, structure, and electrical properties," *Journal of applied polymer science*, vol. 97, no. 1, pp. 51–59, 2005.

[170] A. Celzard, J. Marêché, and F. Payot, "Simple method for characterizing synthetic graphite powders," *Journal of Physics D: Applied Physics*, vol. 33, no. 12, p. 1556, 2000.

[171] I. Kranauskaite, J. Macutkevic, J. Banys, E. Talik, V. Kuznetsov, N. Nunn, and O. Shenderova, "Synergy effects in the electrical conductivity behavior of onion-like carbon and multiwalled carbon nanotubes composites," *physica status solidi (b)*, vol. 252, no. 8, pp. 1799–1803, 2015.

[172] M. Drubetski, A. Siegmann, and M. Narkis, "Electrical properties of hybrid carbon black/carbon fiber polypropylene composites," *Journal of materials science*, vol. 42, no. 1, pp. 1–8, 2007.

[173] L. Yue, G. Pircheraghi, S. A. Monemian, and I. Manas-Zloczower, "Epoxy composites with carbon nanotubes and graphene nanoplatelets–dispersion and synergy effects," *Carbon*, vol. 78, pp. 268–278, 2014.